The Dissertation Committee for Meng Li
certifies that this is the approved version of the following dissertation:

Alfvén modes and wave-particle interaction in a tokamak

Committee:

Boris N. Breizman, Supervisor

Herbert L. Berk

Philip J. Morrison

Richard Fitzpatrick

Irene M. Gamba

Alfvén modes and wave-particle interaction in a tokamak

by

Meng Li, B.S.

DISSERTATION

Presented to the Faculty of the Graduate School of

The University of Texas at Austin

in Partial Fulfillment

of the Requirements

for the Degree of

DOCTOR OF PHILOSOPHY

THE UNIVERSITY OF TEXAS AT AUSTIN

December 2017

Acknowledgments

First of all, I indeed present my gratitude to my supervisor-Prof. Boris Breizman. His guidance and his patient instructions on the fundamental plasma physics theory during daily discussions is really helpful and I can not complete my current research work without it. In the meantime, I am also thankful for his interesting and inspiring courses on plasma physics, which is among the best courses I have taken in UT Austin.

I wish to express my appreciation to Dr. Linjin Zheng for the help throughout these years. He is always supportive and his numerical experience is a treasure for my simulation work. I also thank Prof. Herbert Berk who influences me on the understanding of the physical world. His keen interest in different areas of plasma physics is always an inspiration to me.

I also wish to thank Prof. Philip Morrison, Prof. Richard Fitzpatrick and Prof. Irene Gamba for being my committee members and spending time reviewing my dissertation. I am thankful to Prof. Morrison for all his interesting and challenging courses on mathematics and physics. I am grateful to Prof. Fitzpatrick for the very first class I have taken in UT Austin. I wish to thank Prof. Gamba for all the discussions on my research.

Scientists and students at IFS have helped me a lot. I am always grateful to Prof. Francois Waelbroeck for offering me the valuable chance to

start my study in IFS. I really appreciate the chance to work together with Dr. David Brower on the MST problem. I'd also like to present my thanks to Prof. Richard Hazeltine, Prof. Swedish Mahajan for their courses and seminars. In addition, I wish to thank Dr. Ge Wang, Dr. Eugene Chen, Dr. David Sanz, Adrian Fontanilla, James Oliver and Anna Szczekutowicz for helpful discussion and group study.

At last, I am deeply grateful to my parents for always being understanding and helping me through the hardship of life. I wish to thank all my friends. They made my PhD career not only fruitful but also colorful, and I wish them all the best in their future.

Alfvén modes and wave-particle interaction in a tokamak

Publication No. _____

Meng Li, Ph.D.
The University of Texas at Austin, 2017

Supervisor: Boris N. Breizman

This work is motivated by the nonlinear wave-particle interaction problems. To build a self-consistent theory, we consider eigenmodes of the bulk plasma as well as the dynamics of the energetic particles. The modes of our particular interest are the Alfvén Cascades and the Toroidicity Alfvén Eigenmodes (TAE), which we describe using Magnetohydrodynamic(MHD) analysis and the AEGIS codes. We investigate the stabilizing effect for the Alfvénic waves from continuum damping, especially near the TAE gap. For the kinetic description of the energetic particles, we propose new canonical straight field line coordinates to model the guiding center motion. We then formulate wave-particle interaction problem using the action-angle variables.

In Chapter 2, we interpret Alfvén Cascades observed in Madison Symmetric Torus (MST). We do linear MHD calculations and find the mode frequency, structure, and stability boundary. We then perform MHD simulation

using the AEGIS code, with the equilibrium reconstructed from experiment. The result is discussed and compared with the experimentally observed features.

In Chapter 3, we analyze continuum damping for Alfvénic waves, especially in the extreme situation near the TAE gap. We find that the continuum tip absorption feature is actually related to the existing of TAEs in the gap. On the technical level, we improve the numerical scheme of AEGIS and resolve two closely-spaced singularities. As a result, the absorption features observed in the simulation show good agreement with our analytical calculation.

In order to simulate the energetic particle guiding center motion in the Hamiltonian form, we propose a new set of straight magnetic field line coordinates. The new coordinates exist for general tokamak devices and facilitate both MHD calculations and energetic particles.

The new coordinate system makes it very convenient to take the advantage of the Hamiltionian structure of the guiding center motion. We use a canonical transformation to action-angle variables to formulate the interaction model for particles. The action-angle variables allow us to resolve wave-particle resonances and describe the conserved quantities for resonance particles. The model can give us a complete picture for nonlinear stage of wave-particle interaction.

Table of Contents

ix

List of Tables

List of Figures

Chapter 1

Introduction

1.1 Fusion reaction and tokamak

Fusion power has long been believed to be the ultimate solution to human energy crisis. The fusion fuel, such as deuterium, is resourceful on the earth. Like the fission reaction, fusion has the advantage of high energy capacity and is helpful to reduce the emission of greenhouse gases compared to fossil fuels. For instance, one kilogram of deuterium (D) and tritium (T) fuels would release 10^8 kWh of energy, which is equivalent to a 1 GW power station for a day. On the other hand, Fusion is much safer than fission. The product of fusion reactions is much less radioactive than that from fission reactions. What's more, potential hazards resulting from an uncontrolled chain reaction can not occur with a fusion reactor.

Actually, the development of mankind has always been relying on the fusion power either directly or indirectly during the human history. Fusion reaction happens in the core of the sun and most stars in the universe. The tremendous power in this process leads to photon production in sun's photosphere, and is absorbed when the photons travel to earth to enable life to develop. Although this energy transmission is not efficient, it bred most lives

on earth. That being said, it will be great breakthrough if we can reveal the secrets of the sun and take control of the fusion reaction on this planet.

However, there are challenges associated with opportunities in developing an actual power plant based on fusion reaction. Controlled fusion requires the confinement of a hot plasma dilute gas rather than compact fission rods. Though in principle feasible, the confinement issue turns out to be so difficult that scientists are still attempting to achieve their goal after half a century's effort. In order to start the fusion reaction, the fuel is heated to a very high temperature to overcome the repulsive force between the positive charged nuclei. Therefore, the most challenging problem of controlled nuclear fusion is to maintain a steady equilibrium state of the fusion system and suppress all the instabilities that degrade the fuel's confinement.

A number of efforts are made to control the high temperature fuel and sustain nuclear fusion. Unlike the confinement of fusion fuel in the sun, it is impossible to pull the fusion fuel together using gravitational attraction with much smaller reactor on earth. Instead, people has proposed to compress and heat the fuel with the help of high-energy laser beams. This approach is called inertial confinement. Other than the inertial confinement, another approach is magnetic confinement fusion, which tries to confine the fuel with magnetic field and has a lot progress in the effective energy production [24, 48].

Different types of magnetic confinement devices have been designed and built, in which the tokamak is the most successful device so far. Tokamaks confine the plasma-state fuel in the torus-shaped chamber. In a tokamak,
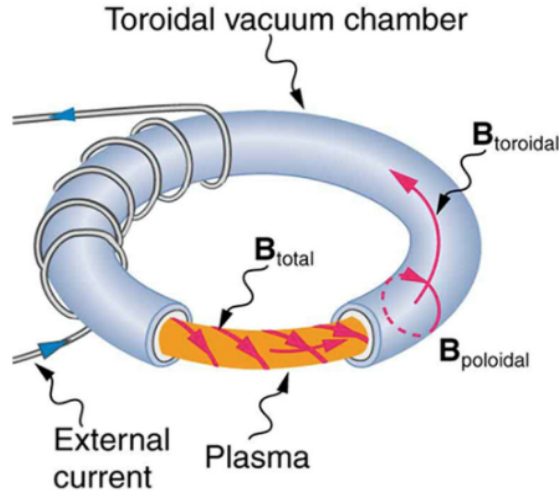
Figure 1.1: An illustration of tokamak and the magnetic field.

the magnetic field spirals around the donut-shape plasma. The magnetic field has poloidal component entirely through plasma current and toroidal field components through the external coils. Safety factor q is often used as the winding number of magnetic fields: one poloidal transit occurs for every q toroidal transits. Other configurations such as the stellarator, reversed field pinch configuration, or spheromak have either externally generated poloidal fields or very different magnetic configuration than a tokamak. All of these devices aim to study how to confine the high temperature plasma and then control the particle flux and heat load deposited on the wall.

Currently, the largest burning plasma experiment- ITER (International Thermonuclear Experimental Reactor)-facility is under construction in Cadarache,

France. The ITER tokamak has the 18 niobiumt-in toroidal field coils and the superconducting central solenoid coil to produce a field of 13.5 tesla. At their maximum field strength, they are expected to have the sufficient confinement to generate a burning plasma. [29, 40]

1.2   Generation of energetic particles

During fusion reaction or heating process, particles that are more energetic than the majority of the plasma can be generated. In the design of practical fusion power plant, energetic particle physics is a key issue which affect the energy balance of the system. For example, the most promising fusion reaction is the D-T reaction, in which the nuclei of deuterium and tritium fuse to produce an alpha particle and a neutron, which carry the most part of fusion energy, i.e.

$$D + T = He(3.5MeV) + n(14.1MeV). \tag{1.1}$$
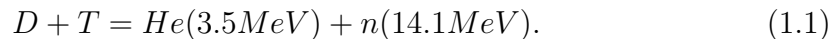
To achieve fusion reaction, the reactant need to reach plasma state with high temperature in order to overcome the Coulomb barrier between deuterium and tritium nuclei. In principle, a practical fusion reactor will need no external heating during the reaction (though auxiliary heating will be used for the ignition and burn control), and the plasma temperature must be maintained for a sufficient confinement time to obtain a net yield of energy. Thus, we have to confine the fusion products as a source to heat the reactants in order to sustain the fusion reaction. In the D-T reaction, neutrons are lost directly

from the system, carrying away a large amount of fusion power, whereas alpha particles are expected to be trapped in plasma and continue to heat the system. Generally, an important measure of the condition for a system to reach fusion ignition is that the heating of the plasma by the fusion product (mainly energetic alpha particles) is sufficient to maintain the temperature of the plasma against all losses without external power input. Only when the breakeven is reached, the burning plasma is self-heated and generate power. Therefore, it is very important to investigate the confinement and transport of the energetic particles for fusion study.

Although the population of energetic alpha particles is relatively small compared to the background density, failure to confine this minority group of particles may result in deleterious consequences. The loss of energetic particles means that the heat source of the plasma is missing, which can quench the fusion. In addition, if the energetic particles are not properly confined at the core, the wall will be degraded since no material can stand the huge energy flux from the direct impact of energetic alpha particle.

Among all the mechanisms of energetic particle transport, collisions may be the most intuitive process. Collision between energetic particle and bulk plasma particles result in energy exchange during the confinement of energetic particles. However, according to the collision theory, the collision time is rather long (0.5s in ITER's targeted burning plasma) as the fast particles tend to be collisionless. Also, most of the alpha particle energy will first heat electrons through the electron drag process during collision. Only about 10%

of the alpha particle energy directly heats ions, which is the reactant species that needs to be hot to have reasonable fusion production. Thus, the time scale for energetic particles to deposit most of their energy into the bulk plasma for self-heating fusion reaction is relatively long.

Instead, these energetic particles can easily lead to instabilities and turbulence through the wave-particle interaction. So far it is known that some waves in tokamak, such as Alfvénic waves, become unstable due to the energetic alpha particles which transfer kinetic energy and momentum of alpha particles to the waves. The momentum transfer can cause alpha particles to cross field lines and possibly be lost to the walls, which brings trouble to our confinement[49]. On the other hand, the wave-particle interaction is a more efficient way to extract energy from alpha particles in a controlled manner than the electron drag. If this can be done without the alpha particles loss, we can expect energy transferred to the background plasma significantly faster and the fusion efficiency greatly improved [19]. Therefore, the understanding of nonlinear coupling processes involved in fast ion interaction with waves is important to global stability, confinement, Alfvén channeling, heating and current drive, thermal instabilities, etc. [14, 26, 27]

1.3 Alfvénic waves in fusion devices

Among the waves that exist in plasmas, the shear Alfvén wave constitutes one of the most fundamental modes of the Magnetohydrodynamic (MHD) spectrum. In a plasma, shear Alfvén waves are transverse electro-

magnetic waves that propagate along the magnetic field. It is analogous to the mechanical waves on magnetic field string with the magnetic pressure as the tension and the mass density provided by the plasma. Shear Alfvén wave dispersion relation is:

$$\omega_A^2 = k_\parallel^2 V_A^2 \tag{1.2}$$

Here wave vector along the equilibrium magnetic field is $k_\parallel = \mathbf{k} \cdot \mathbf{B}_0 / B_0$, the Alfvén velocity is $V_A = B_0 / \sqrt{4\pi\rho}$ and ρ is plasma mass density.

In a tokamak, at the cylindrical limit, the periodicity of the system require that there exists two integers, a toroidal mode number n and a poloidal mode number m, such that

$$k_{\parallel m} = \frac{n - m/q}{R_0}$$

where q is the safety factor, R_0 is the distance from the symmetry axis of the tokamak to the magnetic axis. Because of the radial in-homogeneity in the wave vector and Alfvén speed, the shear Alfvén dispersion relation is a continuous function with radius and is thus called shear Alfvén continuum. In the presence of the shear Alfvén continuum, radially-extended waves will be stabilized because of the interaction with Alfvén continuum, which is also called continuum damping/continuum absorption [23]. Continuum absorption results in mode conversion from the global oscillation to the local shear Alfvén wave limited to the vicinity of a certain resonant surface, which can efficiently damped through phase mixing and transfer wave energy to the plasma kinetic energy.
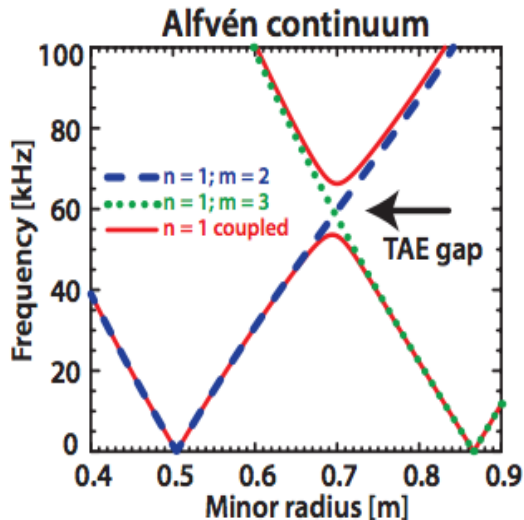
Figure 1.2: An example of the shear Alfvén continuum spectrum. Due to toroidicity, a frequency gap appears in the continuum spectrum. TAE waves cab be excited due to energetic particles in the gap region. [31]

However, the continuum can have gap structure due to toroidicity, similar to the propagation gap occurs at the Bragg frequency in solid state physics. In a torus with a small inverse aspect ratio ($\epsilon = a/R_0 << 1$, where a is distance from the wall to the magnetic axis), the magnetic field can be approximated by $B \approx B_0(1 - \epsilon cos\theta)$ where θ is the poloidal coordinate. The parallel component of the wave vector now also depends on the poloidal coordinate θ which can lead to the coupling of the dispersion relations belonging to neighboring poloidal mode numbers m and $m + 1$. The crossing of m and $m + 1$ components in the continuum spectrum is expected to be at the radius where the

wave number equals:

$$k_{\|m_1}(r_0) = -k_{\|m+1}(r_0).$$

But the toroidicity resolves the degeneracy of intersection and produces gaps in continuum spectrum. Within these gaps global modes can exist without experiencing strong continuum damping.
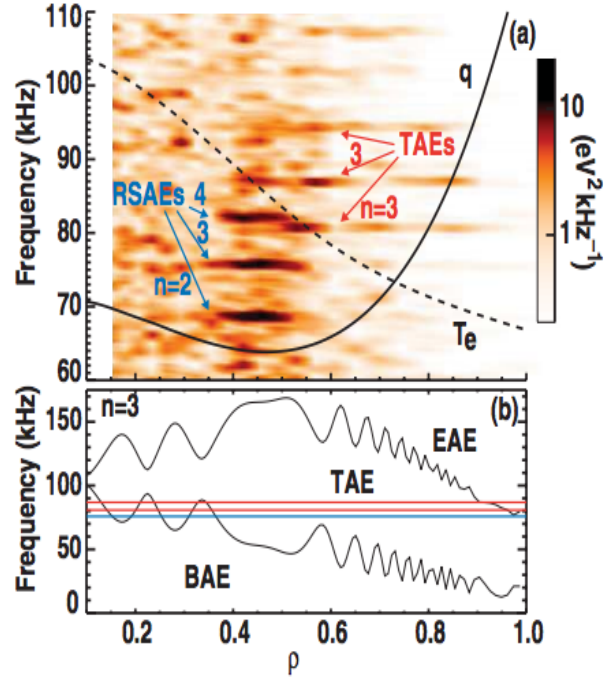
Figure 1.3: (a) RSAEs (blue line) and TAEs (red line) are pointed out along with toroidal mode number (n). The solid overlaid line is the safety factor profile (q) and the dashed line is the electron temperature profile. (b) n= 3 Alfvén continuum including toroidal rotation. The horizontal lines mark n=3 RSAE (blue line) and TAE (red line) frequencies from (a), and the BAEs have lower frequencies. From Ref. [47]

9

The poloidal symmetry-breaking in the toroidal confinement device leads to the couplings between neighboring poloidal harmonics, which not only opens a gap in the continuous shear Alfvén spectrum, but also produces discrete Alfvén eigenmodes. These modes are called toroidicity-induced Alfvén eigenmodes (TAEs) [18, 50]. These TAEs are linearly excited and is undamped to the lowest order in the gap. Dissipation however may still present due to weak viscosity, resistivity and remnant interaction with the continuum in spatial regions where the wave amplitude is weak [43, 44].

Besides TAEs, other discrete Alfvén eigenmodes can exist near continuum accumulation points due to shaping, magnetic shear, energetic particle effects and other effects[38, 2, 21]. The properties of these discrete eigenmodes such as frequency or mode structure are mostly determined by the background plasma. For instance, a similar gap mode is the β-induced Alfvén eigenmode (BAE) [12]. The BAE gap is introduced by the coupling between compressible acoustic waves and the shear Alfvén continuum. Another important kind of the discrete modes-Alvén Cascade (or RSAEs)-will be introduced in Chapter 2.

1.4 Different regimes of wave-particle interaction

As discussed, various discrete eigenmodes exist in the gap. These modes can easily be driven unstable by the free energy in the fast ion distribution function if the energetic particles satisfy the resonance condition[21, 20]. For example, the TAE structure and eigenfrequency ω_0 can be calculated from the

MHD equations. Since the wave is weakly damped due to thermal plasma kinetic effects, it can be excited by a small group of passing particles which satisfy the resonance condition $\omega_0 = k_\parallel v_\parallel$ (where $v_\parallel$ is the parallel velocity to the equilibrium magnetic field). In this scenario, the mode structure and frequency is predetermined by the bulk plasma and damping is minimal, while the energetic particle effects are often perturbative.

For frequencies located inside Alfvén continuum, continuum damping will stabilize the global oscillation. However if the energetic particle pressure is sufficiently high compared to the thermal pressure, the energetic particle drive can overcome the continuum damping and non-MHD modes are excited [17]. These mode structure sensitively depend on the energetic particle distribution. Their frequencies usually correspond to the characteristic frequencies of the energetic particle orbital motion, and sweep as the instabilities develop. These modes constitute a non-linear system where MHD and energetic particle contribution can both be important and are called Energetic-Particle-Modes(EPM).

To study the wave-particle interaction, we can start from the simple 1D bump-on-tail problem, which is a very common instability in plasma physics [3]. When the energetic particles have an inverted distribution, forming a bump on the tail of the thermal particle distribution, there will be an instability with the strong wave excitation. In the linear theory, the bump-on-tail instability can be thought of as the inverse of Landau damping, where the existence of more particles that move faster than the wave phase velocity as

11

compared with those that move slower, leads to an energy transfer from the particles to the wave [1, 25]. The instability saturates when the distribution is flattened at the resonance region.
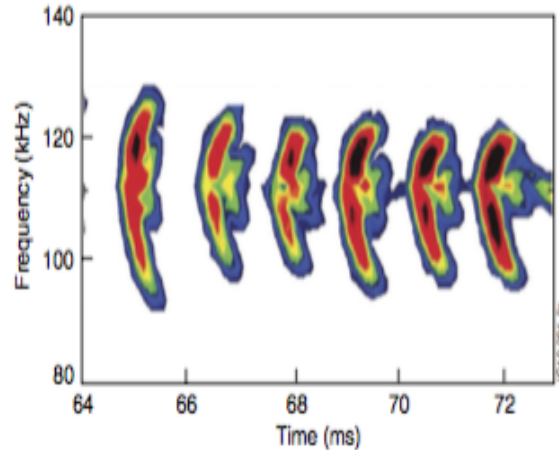
Figure 1.4: Experimental observation is successfully explained by the Berk-Breizman model in the MAST spherical tokamak. Modes that are driven unstable by neutral beam ions begin at the TAE frequency, then chirp upward and downward in frequency. From Ref.[42].

Experimental results, in the case of neutral beam injection, demonstrate that EPMs exhibit a hard nonlinear regime with rapid frequency sweeping. Small deviations from the initial eigenfrequency for the case of a near-threshold instability were first studied by Berk-Breizman (BB) and co-workers[5, 6, 7]. This model show that when the bump-on-tail instability evolves into its non-linear stage, Bernstein-Greene-Kruskal (BGK) modes [28] are formed due to nonlinear properties of the instability resonances, provided that each resonance is sufficiently separated so that mode overlap does not arise. The interplay

12

between the wave field, which tends to flatten the distribution of resonant particles, and the source and sink relaxation processes, which tend to restore the unstable distribution function, leads to various nonlinear effects [14].

The Berk-Breizman model demonstrates three kinds of behavior emerge, namely steady-state, periodic, or explosive response[11]. It was shown that the explosive state evolved into hole and clump phase-space structures in the fast particle distribution function, which support a pair of BGK nonlinear modes, and the motion of these coherent structures causes frequency chirping signals to appear[8, 4]. The rate of frequency shift can be calculated by the balance between the rate of energy being nonlinearly extracted from the resonant particles and the power dissipated into the background plasma through the various damping mechanisms present in the system. The Berk-Breizman scenario has been proved to be successful in explaining the frequency chirping events observed in experiments where the range of frequency chirping is small.

Note that in the spontaneous hole-clump creation model, the initial quantitative description was limited to the case of small frequency deviations from the bulk plasma eigenfrequency. However, there are experimental observations of frequency sweeping events in which the change in frequency is comparable to the frequency itself. As the mode amplitude saturates due to flattening of the distribution function of the energetic particles, the physical picture of each evolving phase-space structure is a BGK mode whose frequency changes in time and its structure is notably affected by the frequency shift. A non-perturbative model based on the adiabatic description of the fast par-

ticles contribution has been developed by Breizman [41, 10] to interpret the long range chirping for an isolated nonlinear resonance. This non-perturbative approach is premised on the assumption that the width of the separatrix supported by the BGK mode is small compared with the characteristic width of the unperturbed distribution function. The underlying idea is that coherent structures with varying frequencies represent nonlinear traveling waves in fast particle phase space. Different from the bulk plasma eigenfrequency, a small coherent group of these particles can still produce an observable signal with a frequency.
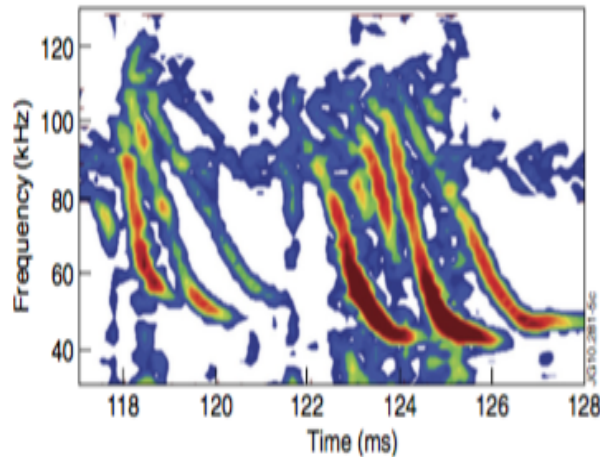
Figure 1.5: NBI-driven chirping modes on MAST, From Ref.[22].

In this thesis, we exhibit our effort to numerically generalize the nonlinear wave-particle interaction model that is valid for both perturbative and nonperturbative case. In chapter 2, We do ideal MHD analysis for the bulk

14

plasma and discuss the stability of the Alfvén Cascade as the discrete eigenmodes, which is observed in Madison Symmetric Torus. In chapter 3, we investigate the continuum damping, especially around the TAE tip, which is important for EPM with significant frequency sweeping. In chapter 4, we turn to the kinetic study of the energetic particles and find that there is a preferable magnetic field for the description of energetic particle guiding center motion. In chapter 5, we describe the action-angle model that combine the previous efforts and simplify the resonant particle dynamics to one dimensional problem.

Chapter 2

Alfvén Cascade in the Madision Symmetric Torus

2.1 Introduction of Alfvén Cascade

In the experiments to obtain Internal Tranport Barriers, the safety factor profiles $q(r)$ often becomes non-monotonic. Such plasmas have a region of magnetic shear reversal, which creates new extremes in the Alfvén spectrum. In addition to the TAEs, these plasmas can also accommodate the so-called Alfvén Cascades, also known as reversed-shear Alfvén eigenmodes (RSAEs). The Alfvén Cascades are associated with the extremum point of the shear Alfvén continuum localized at the magnetic surface with the minimum value of $q(r)$, labelled as q_0. In the simplest case of cold (low pressure) plasma, this gives

$$\omega_{AC}(t) \approx \frac{V_A}{R_0}|n - \frac{m}{q}| + \Delta\omega$$

Note that the first (dominant) term on the right-hand side of the equation is the shear Alfvén continuum frequency at the zero shear point. The correction $\Delta\omega$ describes a deviation of the Alfvén Cascade eigenfrequency from the continuum, and it originates from the effects of large ion orbits, toroidicity and thermal plasma pressure gradient.

In the evolution of the plasma current, the eigenfrequency of the Alfvén Cascades, $\omega_{AC}(t)$, changes in step with $q_0(t)$ in accordance with the local dispersion relation for shear Alfvén waves, while $\Delta\omega$ remain nearly constant on the time scale of $q_0(t)$ evolution. Except in the vicinity of TAE gap, Alfvén Cascade consists of predominantly one poloidal Fourier component and the mode structure agrees quantitatively with MHD calculation.
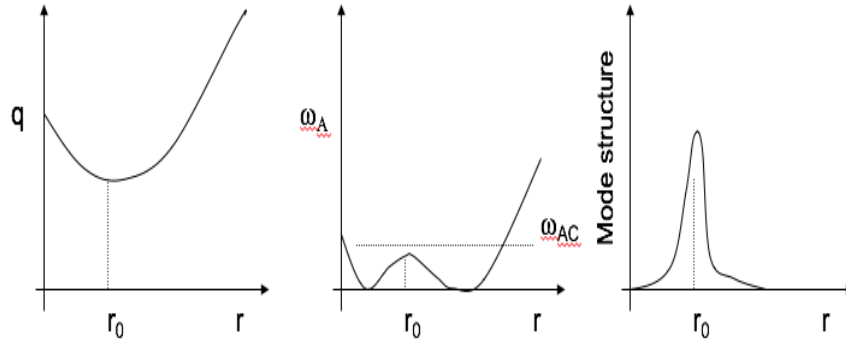
Figure 2.1: A illustration of the magnetic shear reversal, continuum spectrum extreme, and the mode structure for Alfvén Cascades

2.2   AEGIS scheme

The Alfvén Cascade can be numerically calculated by the Adaptive ideal-magnetohydrodynamics Shooting code-AEGIS(short for Adaptive EiGenfunction Independent Solution)[51]. The ideal MHD equations used in AEGIS is derived from single fluid and Maxwells equations:

$$\rho \frac{d\mathbf{v}}{dt} = -\nabla P + \mathbf{J} \times \mathbf{B}$$

$$\mathbf{E} = -\mathbf{v} \times \mathbf{B}$$

$$\frac{\partial P}{\partial t} = -\mathbf{v} \cdot \nabla P - \Gamma P \nabla \cdot \mathbf{v}$$

$$\frac{\partial \rho_m}{\partial t} = -\mathbf{v} \cdot \nabla \rho_m - \rho_m \nabla \cdot \mathbf{v}$$

$$\frac{\partial \mathbf{B}}{\partial t} = \nabla \times \mathbf{E}$$

$$\mu_0 \mathbf{J} = \nabla \times \mathbf{B}$$

where ρ_m is mass density, $\mathbf{v}$ denotes fluid velocity, P is plasma pressure, Γ represents the ratio of specific heats, $\mathbf{E}$ and $\mathbf{B}$ represents respectively electric and magnetic fields, J is current density, and bold faces denote vectors.

After linearization of the perturbed MHD equations, one obtains a single equation for

$$\mu_0 \rho_m \frac{\mathrm{d}^2 \boldsymbol{\xi}}{\mathrm{d}t^2} = [\nabla \times \nabla \times (\boldsymbol{\xi} \times \mathbf{B})] \times \mathbf{B} + (\nabla \times \mathbf{B}) \times [\nabla \times (\boldsymbol{\xi} \times \mathbf{B})]$$
$$+ \nabla (\boldsymbol{\xi} \cdot \nabla P + \Gamma P \nabla \cdot \boldsymbol{\xi}), \tag{2.1}$$

where $\boldsymbol{\xi}$ is the perturbed plasma displacement, and $\mathbf{B}$ is the equilibrium magnetic field.

The plasma parallel compressibility is neglected here, since that corresponds to the acoustic wave propagating along the magnetic field line. Using Fourier decomposition in the poloidal (θ) and toroidal (ζ) directions, the perturbed quantities are transformed as:

$$\xi_\psi \mathrm{e}^{-in\zeta} = \sum_{m=-\infty}^{\infty} \xi_m \frac{1}{\sqrt{2\pi}} \mathrm{e}^{i(m\theta - n\zeta)}. \tag{2.2}$$

18

Then we get the final equation for the $\xi_\psi(\nabla\psi$ component of $\boldsymbol{\xi})$

$$(\mathbf{F}\xi'_{\psi m} + \mathbf{K}\xi_{\psi m})' - (\mathbf{K}^\dagger\xi'_{\psi m} + \mathbf{G}\xi_{\psi m}) = 0, \tag{2.3}$$

To solve this equation, AEGIS employs a multiple-region shooting scheme to avoid the numerical pollution by direct shooting. In this scheme, the entire region from the plasmas magnetic axis to the plasma edge is divided into multiple regions, the complete set of independent solutions in each region is first calculated. The adaptive-mesh shooting method is used to obtain the independent solutions, especially at the magnetic axis and singular mode surface. These independent solutions can then be used to construct the global solution that satisfies the boundary conditions.

2.3 Study of the Alfvén Cascade in the MST: Paper A
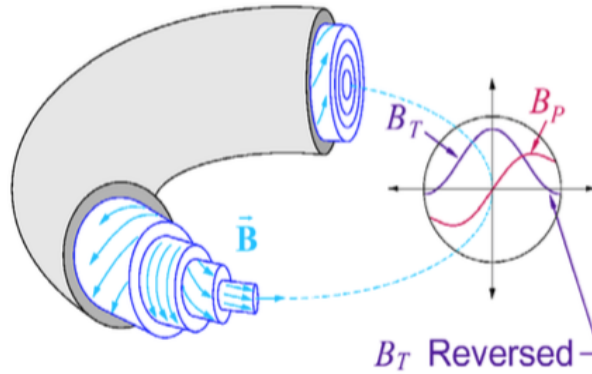
Figure 2.2: MST magnetic field configuration

The Madison Symmetric Torus (MST) is a Reversed Field Pinch(RFP) device locates in Madison, Wisconsin. Unlike tokamak, in RFP devices, the toroidal field is weak and the distinct configuration - low safety factor and high magnetic shear - are likely to bring interesting variations for the study of Alfvén Cascades. During the neutral beam heating experiments of MST, there are observations of busty fast-ion-driven instabilities(mainly $n = 4$ and $n = 5$)[35, 36]. These modes are localized at the core, which is away from the TAE gap. Besides, both modes are dominated by the $m = 1$ component and their frequencies are lower than the TAE frequency. The fact that con-
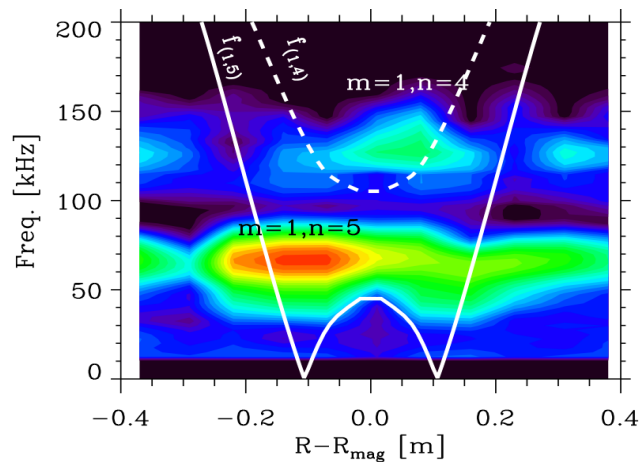
Figure 2.3: Spatial and frequency (in the plasma frame) distribution of line-integrated electron density fluctuation power for the n=4 and n=5 Energetic Particle modes. The Alfvén continua at the mid-plane are over plotted: solid line for m=1, n=5 and dashed line for m=1, n=4. [35]

tinuum spectrum is relatively flat at the core and close to the mode frequency easily evoke our speculation that these modes are Alfvén Cascades. Since

the mode is localized at the core and there are no coupling between different poloidal components, we focus on the simplified cylindrical model analytically and found the coexistence of $n = 4$ and $n = 5$ modes require a small parameter window for the pressure gradient. We also reconstruct equilibrium from MST experiment and use AEGIS code to numerically study the stability. Note that MST equilibrium contains magnetic island close to the core, we seek for modes localized within the core and vanish before the first magnetic island. Paper A presents details of such study for the modes observed in MST [34].

Chapter 3

Continuum absorption near the TAE gap

3.1 Analogues of continuum absorption - Landau damping problem

The methodology developed for the analysis of continuum absorption is very similar to that of the classical Landau damping problem. Landau damping can be defined as damping of a collective mode of oscillations in a plasma, where collisions between the charged particles are negligibly rare [30]. This phenomenon was predicted in 1946 for Langmuir oscillations.

In the 1D Landau damping problem, we consider the initial value problem for a localized Langmuir perturbation. We assume that the ions form an immobile, neutralizing background and we shall look for electrostatic plasma waves. Considering only small perturbations of the distribution function δf and linearizing the Vlasov equation, one finds:

$$
\frac{\partial \delta f}{\partial t} + v\frac{\partial \delta f}{\partial r} + \frac{e}{m}\frac{d\phi}{dr}\frac{\partial f_0}{\partial v} = 0
$$
$$
\frac{d^2\phi}{dr^2} = \frac{e}{\epsilon_0}\int \delta f dv
$$

where ϕ is the electric potential, f_0 is the equilibrium distribution function. We can assume the perturbed quantities vary with r and t as

$exp(i(kr - \omega t))$. Combine the two equations, we get

$$1 + \frac{e^2}{\epsilon_0 m k^2} \int \frac{k(\partial f_0/\partial v)}{\omega - kv} dv = 0$$

We can interpret this equation as the dispersion relation for electrostatic plasma waves, which relates the wave-vector, k, to the frequency, ω. However, this dispersion relation has a serious problem, since the integral has a singularity in velocity space, where $\omega = kv$, and is not properly defined.

The way to get around this problem is to introduce the Laplace transform of δf with respect to t:

$$\delta f(\omega) = \int_0^\infty \delta f(t) e^{-i\omega t} dt. \tag{3.1}$$

If ω possesses a positive real part, then above integral is well defined. Note that in $\omega = \omega_0 + i\nu$, ν actually can be interpreted as the collision frequency. Suppose that, to a first approximation, ω is real. Letting ω tend to the real axis from the domain $\text{Im}(\omega) > 0$, we obtain:

$$1 + \frac{e^2}{\epsilon_0 m k^2} P.v. \int \frac{k(\partial f_0/\partial v)}{\omega - kv} dv + \frac{i\pi e^2}{\epsilon_0 m k^3} \left(\frac{\partial f_0}{\partial v} \right)_{u=\omega/k} = 0 \tag{3.2}$$

The last term in the left hand side will result in a damping effect to the wave. This damping effect is called Landau damping, which does not depend on the artificial collision frequency ν.

Similarly, in the continuum absorption problem, the simplified equation for a single harmonic in the cylindrical limit is:

$$\frac{d}{dr}(\omega^2 - \omega_A^2(r)) \frac{d\Phi_m}{dr} - k^2(\omega^2 - \omega_A^2(r))\Phi_m = 0, \tag{3.3}$$

23

where $\omega_A(r)$ is the local Alfvén frequency, Φ_m is a single harmonic of the perturbed electric field. The singularity in this equation occurs at r_0 where $\omega = \omega_A(r_0)$, and has the same origin as the one that in the Landau damping problem. Continuum absorption then results from the singularity where the energy get absorption. A reliable way of assessing continuum absorption is to consider an initial value problem, and then use a Laplace transform technique. A close similarity with Landau damping then becomes obvious, and it is easy to get that the continuum absorption is inversely proportional to the slope of the continuum $d\omega_A(r_0)/dr$.

3.2 Continuum absorption near the TAE gap : paper B

However, as shown in the introduction, TAE gap forms due to toroidicity induced coupling in the Alfvén continuum of a tokamak. In this case, the continuum is nearly flat at the edges of the TAE gap and forms two tips, which is different from the cylindrical case. The need to evaluate continuum absorption at the tips arises when energetic particle driven modes chirp away from the TAE frequency and hit one of the tips[16]. Recalling the cylindrical picture, one might then expect the continuum absorption is huge at the tip. Yet, a more careful investigation would need to take into account the coupling between neighboring poloidal harmonic due to toroidicity.

It is noteworthy that the meaning of continuum absorption is different between the discrete eigenmode case and the energetic particle mode case. Continuum absorption can occur when the tails of the discrete eigenmodes

24
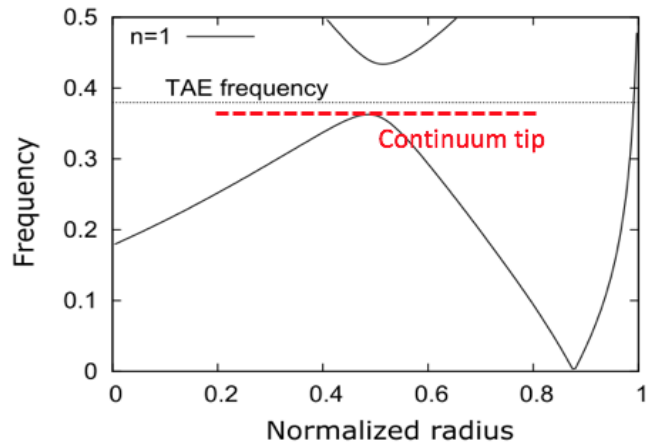
Figure 3.1: Continuum absorption needs to be evaluated for the case that the energetic particle mode frequency near the tip

cross the continuum. In this case, the mode structure is robust and the eigenfrequency is predetermined, while the continuum crossing only introduces a small modification. Thus for a given eigenmode, we can define the wave energy which will fix the continuum absorption, since the result of continuum absorption is mostly determined by the local mode and continuum structure. Then the continuum spectrum effectively introduces a damping rate for the discrete eigenmode case.

On the other hand, the mode structure and frequency are not fixed but depend on the drive in the energetic particle mode case. Even with the same frequency, energetic particle mode structure varies for different types of energetic particle distribution, which means the continuum absorption is not predetermined. So unlike the eigenmode case, continuum absorption rate is

not defined, and the exact value of continuum absorption only make sense if we specify the type of drive for energetic particle modes.

Thus, for the general calculation of energetic particle modes near the TAE gap, we need to introduce an external source to probe the continuum absorption, which mimics the energetic particle current in the chirping event. Also, like in the Landau damping problem, we use Laplace transform to resolve the MHD singularities [52], which is equivalent to introducing a friction force acting on the plasma flow. We have modified the ideal MHD eigenvalue code AEGIS to implement this approach numerically. In order to resolve the two nearby singularities near the tip frequency, we set the adaptive grid in AEGIS at the continuum crossings after iteratively search.
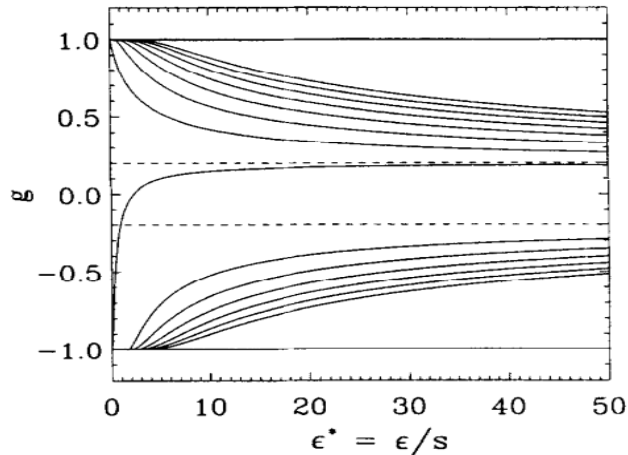
Figure 3.2: Occurrence of multiple TAEs in the gap due to increasing $\epsilon^* = \epsilon/s$
. From Ref.[15].

To analytically look at the problem, we use the singular perturba-

tion method near the gap, which procedure is similar to the classical TAE theory[13]. As a result, we find the tip absorption pattern is highly correlated to TAEs. The MHD equations contain two dimensionless parameters: the inverse aspect ratio ϵ and the magnetic shear s. Depending on their relative values, the gap accommodates one, two, or multiple TAEs. Meanwhile, in our study, we found the different absorption patterns near the lower tip and the upper tip varies, which has deep connection with the nearby TAE frequencies. These features are also observed in our simulation, suggesting the continuum damping problem is well resolved and we can fully calculate the bulk plasma response with AEGIS module. For more details of our work, please see paper B in the appendices [33].

Chapter 4

Canonical straight field line coordinates

4.1 Introduction to magnetic flux coordinates

In the MHD calculation of previous two chapters, magnetic flux coordinates are used. In the presence of strong magnetic field, the hot plasma is usually very anisotropic because particles are relatively free to stream in the direction along the magnetic field. Due to this anisotropy, there is often considerable simplification using the coordinate system aligned with the magnetic field, which is magnetic flux coordinates[46].
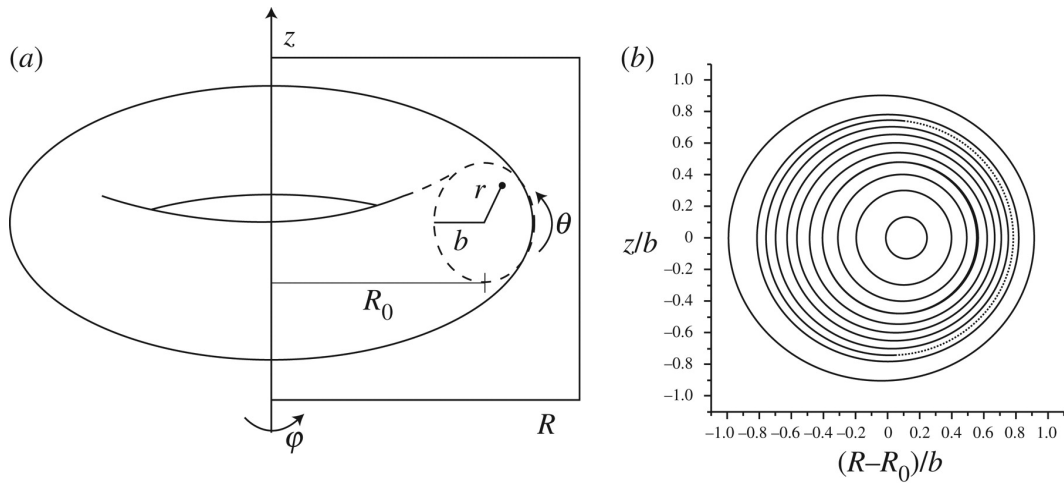
Figure 4.1: (a)Magnetic flux coordinates in a tokamak; (b) nested Magnetic surfaces in the tokamak cross section

A two dimensional surface defined by $\chi(\mathbf{r}) = constant$ is said to be a magnetic surface if at any point the equilibrium magnetic field lies within the surface, i.e. $\mathbf{B} \cdot \nabla \chi = 0$. The existence of nested magnetic surfaces over a large fraction of the plasma volume is an essential for long term confinement. Thus, we can use magnetic flux label χ as one of the new coordinates instead of using all three cylindrical coordinates (R, ϕ, Z) if we find the magnetic surfaces χ. Assuming perfect axisymmetry, the equilibrium magnetic field can be generally expressed as:

$$\mathbf{B} = \nabla \phi \times \nabla \chi(R, Z) + g(R, Z)\nabla \phi, \tag{4.1}$$

where both χ and g are unknown functions, and χ is also the poloidal flux function. In the MHD equilibrium, we have

$$\mathbf{J} \times \mathbf{B} = \nabla P$$

$$\mu_0 \mathbf{J} = \nabla \times \mathbf{B}$$

Take the projection of first equation (the force balance equation) with respect to $\nabla \phi$, $\mathbf{B}$, $\nabla \chi$, we obtain the following restrictions:

$$g = g(\chi)$$

$$p = p(\chi)$$

and also the Grad-Shafranov equation [45]

$$R\frac{\partial}{\partial R}(\frac{1}{R}\frac{\partial \chi}{\partial R}) + \frac{\partial^2 \chi}{\partial Z^2} + \mu_0 R^2 \frac{dp}{d\chi} + g\frac{dg}{d\chi} = 0. \tag{4.2}$$

The Grad-Shafranov equation helps to find the magnetic surfaces with equi-librium measurement of p and g in the experiment. Then magnetic flux coordinates can then be constructed using χ, poloidal angle, and toroidal angle.
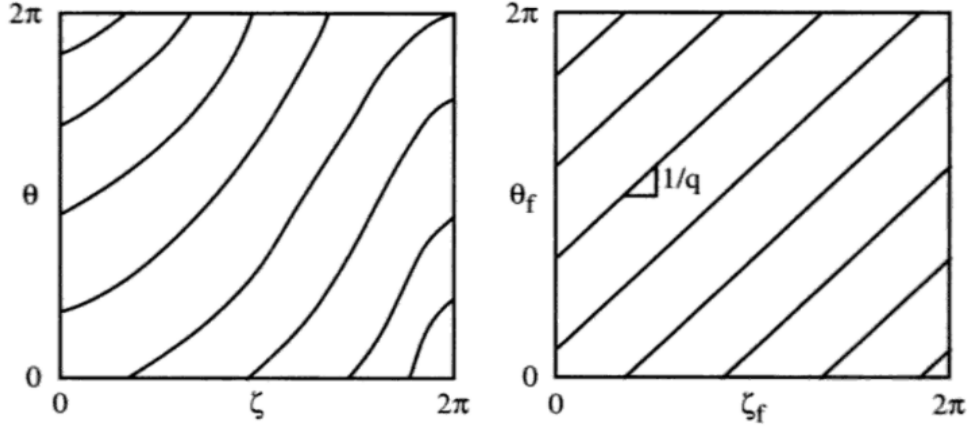
Figure 4.2: Straight field line coordinates [24]

Furthermore, we call a flux coordinate system straight field line if

$$\mathbf{B} = \nabla\phi \times \nabla F(\chi) + \nabla H(\chi) \times \nabla\theta).$$

For instance, if we use general flux label $\psi(\chi)$ instead of χ and we keep the geometric angle ϕ, so that the equilibrium field is

$$\mathbf{B} = \chi' \nabla\phi \times \nabla\psi + g\nabla\phi.$$

If we use (ψ, θ_p, ϕ), the Jacobi for the coordinate transform in Cartesian coordinates is

$$J = \frac{1}{\nabla\psi \times \nabla\theta_p \cdot \nabla\phi}.$$

Then in order for the coordinates to be straight field line, θ_p has to satisfy:

$$\frac{1}{\nabla\psi \times \nabla\theta_p \cdot \phi} = \frac{q\chi' R^2}{g}$$

Here (ψ, θ_p, ϕ) is often called PEST coordinates. Besides PEST coordinates, there are various kinds of straight field line coordinates for different definition of the angles. Straight field line coordinates are especially useful for linear stability calculations where one often use the spectral representation in the toroidal and poloidal directions. From example, it can be easily seen that $q = m/n$ when $k_\parallel$ vanishes, which stands for a single magnetic flux called the rational surface.

4.2 Canonical straight field line coordinate: Paper C

However, when it comes to the description of energetic particle, the straight field line coordinates are not optimal. The motion of charged particles in electromagnetic fields consists of the free-streaming motion along the magnetic field, and the gyromotion perpendicular to the magnetic field. In order to integrate particle motion for the required length of time, such as the wave-particle interaction time scale, an expansion of the motion in the gyro radius needs to be done, with the rapid gyro motion averaged and only guiding center motion left. This work has been done and the guiding center motion Lagrangian is derived by the Littlejohn in Ref.[37]. In the Littlejohn Lagrangian, the guiding center phase space is six-dimensional, but the six dynamical variables in the Lagrangian do not form three canonical pairs. Thus, the most

natural variables in the Littlejohn Lagrangian doesn't preserve a Hamiltonian structure.

In paper C, we look into Littlejohn Lagrangian to obtain a Hamiltonian description of the guiding center motion in the unperturbed fields. We find the crux of finding canonical coordinates lies in proper choice of spatial coordinates that suits the geometry of magnetic field. Thus we introduce new "canonical straight field line coordinates" by eliminating the covariant and contravariant components of the radial magnetic field simultaneously [39]. The fact that the radial component of the magnetic field vanishes allows us to express the guiding center Lagrangian in terms of the angle coordinates and their conjugate momenta in a straightforward way. Meanwhile, the new coordinates are also straight field line coordinates, which is beneficial for MHD simulations [32].

Chapter 5

Wave-particle interaction model in action-angle variables

Based on the works done with the MHD module and the new magnetic flux coordinates, we now turn to the nonlinear wave-particle interaction model in realistic tokamaks. Particles near the resonance produce the most significant nonlinear response, which needs to be included in the MHD equations. As discussed in the introduction chapter, previous 1D analysis reveals different nonlinear scenarios, ranging from benign mode saturation to spontaneous formation of nonlinear coherent structures (phase space holes and clumps) with time-dependent frequencies. The conclusions from the 1D model are difficult to apply to the realistic tokamaks directly, due to sophisticated particle motion in the tokamak magnetic field. The way to overcome this difficulty is to note that particle motion in the unperturbed tokamak magnetic field is fully integrable within the guiding center approximation, which suggests canonical transformation to action-angle variables. Besides, though the wave-particle interaction is nonlinear, the wave amplitude is still small compared to the strong equilibrium magnetic field. We can therefore use the action-angle variables of the unperturbed motion to describe the wave-particle interaction.

In this chapter, we present a procedure of reducing the energetic particle dynamics from 3D realistic tokamak to 1D bump-on-tail model, by using the action-angle variables for the energetic particle guiding center motion. First, the action-angle variables are determined for the particle motion in the unperturbed field. We then consider Hamiltonian description of the interaction in the single resonance case, which effectively becomes one-dimensional using action-angle variables. This implies that the resonances are well separated in phase space so that the energetic particle response can be treated as a sum over several independent resonances. With the reduced Hamiltonian formalism, coherent phase space structures and the corresponding energetic particle transport can be investigated in the vicinity of each isolated nonlinear resonance, similar to the 1D problem.

5.1 Action-angle variables for unperturbed guiding center motion

5.1.1 From guiding center Lagrangian to Hamiltonian formulation

The charged particle motion in the presence of strong magnetic field is an old topic in plasma physics, in which the difficulty is to follow the particle orbit for a long time comparable to the confinement time. A relevant techinique in this case is the guiding-center approximation, because the gyro radius of the charged particle is small compared to the characteristic size of the tokamak magnetic field. After averaging over the fast gyro motion, the guiding center equations can be written in the Lagrangian form. The Lagrangian for the

guiding center motion was derived by Littlejohn as

$$L(\mathbf{X}, \mu, v_{\parallel}, \xi) = \frac{e}{c}\mathbf{A} \cdot \dot{\mathbf{X}} + mv_{\parallel}\frac{(\mathbf{B} \cdot \dot{\mathbf{X}})}{B} + \frac{mc}{e}\mu\dot{\xi} - \mu B - \frac{1}{2}mv_{\parallel}^2. \qquad (5.1)$$

The dynamical variables in this Lagrangian are: $\mathbf{X}$ (the guiding center position), $\mu = mv_{\perp}^2/2B$ (the magnetic moment), ξ (the gyroangle), and $v_{\parallel}$ (the parallel velocity). The magnetic field $\mathbf{B}$, the vector potential $\mathbf{A}$, and the scalar potential Φ are evaluated at the guiding center position.

In the Littlejohn Lagrangian, magnetic moment μ is an invariant. When the fields are time independent, particle energy is also conserved. In addition, toroidal angular momentum is conserved in a tokamak, because the equilibrium magnetic field is designed to be axisymmetric. With the three conservation laws, the guiding center motion is fully integrable within Hamiltonian description.

We use the canonical straight field line coordinates discussed in Chapter 4 to obtain a set of canonical coordinates from Littlejohn Lagrangian. As shown in Chapter 4, the equilibrium magnetic field and the vector potential can be expressed using canonical straight field line coordinates as

$$\begin{aligned} \mathbf{B} &= B_\theta(\psi, \theta)\nabla\theta + B_\zeta(\psi, \theta)\nabla\zeta \\ \mathbf{A} &= A_\theta(\psi)\nabla\theta + A_\zeta(\psi)\nabla\zeta = \int q\chi' d\psi \nabla\theta - \chi\nabla\zeta \end{aligned}$$

where θ and ζ stand for the redefined poloidal and toroidal angles. We can then easily write the Lagrangian in the Hamiltonian form:

$$L_{part} = P_\theta\dot{\theta} + P_\zeta\dot{\zeta} + \frac{mc}{e}\mu\dot{\xi} - H(P_\phi; P_\theta; \theta; \mu) \qquad (5.2)$$

where

$$P_\theta = \frac{eA_\theta}{c} + mv_\parallel \frac{B_\theta}{B_0}$$

$$P_\zeta = \frac{eA_\zeta}{c} + mv_\parallel \frac{B_\zeta}{B_0}$$

are the canonical angular momenta for θ, ζ. Here $(P_\zeta, P_\theta, \zeta, \theta)$ are now new dynamical variables for the Lagrangian, in addition to (μ, ξ). The Hamiltonian

$$H = \mu B_0 + \frac{1}{2} m v_\parallel^2$$

needs to be expressed in terms of the new dynamical variables. Compared to the original variables $(v_\parallel, \psi, \zeta, \theta)$, the quantities $(P_\zeta, P_\theta, \zeta, \theta)$ form canonical pairs for the Hamiltonian. It is apparent that P_ζ is a conserved quantity since the Lagrangian doesn't have dependence on ζ from the equilibrium field.

Note that our canonical straight field line coordinates also provide Hamiltonian formalism for relativistic particles. In the relativistic case

$$\mathrm{L} = (\frac{e}{c}\mathbf{A} + p_\parallel \frac{\mathbf{B}}{B}) \cdot \dot{\mathbf{X}} + \frac{m_0 c}{e} \mu \dot{\xi} - H \tag{5.3}$$

where $\gamma = 1/\sqrt{1 - v^2/c^2}$, m_0 is the rest mass. $H = \gamma m_0 c^2$ and can also be written as

$$H = \sqrt{1 + (2/m_0 c^2)\mu B(\mathbf{X}, t) + \frac{p_\parallel^2}{(m_0 c)^2}} m_0 c^2$$

The definitions of magnetic moment and parallel moment are:

$$\mu = \frac{\gamma m_0 c}{Be} \dot{\xi}$$

36

$$p_\| = \gamma m_0 \frac{\mathbf{B}}{B} \cdot \dot{\mathbf{X}}$$

Then the canonical moments can be easily generalized as

$$P_\theta = \frac{e}{c} A_\theta + p_\| b_\theta;$$
$$P_\zeta = \frac{e}{c} A_\zeta + p_\| b_\zeta;$$

where $p_\|$ is linked to $E(H), P_\zeta, \mu$ through

$$p_\| = \pm\sqrt{\frac{H^2}{c^2} - m_0^2 c^2 - 2m_0 \mu B}$$

5.1.2 The equations of motion and the unperturbed guiding center orbits

To integrate the guiding center motion, we start from the Hamiltonian formulation, rather than directly from the Lagrangian. The equations of motion are:

$$\dot{P}_\theta = -\frac{\partial H}{\partial \theta}; \dot{P}_\zeta = -\frac{\partial H}{\partial \zeta}; \dot{\theta} = \frac{\partial H}{\partial P_\theta}; \dot{\zeta} = \frac{\partial H}{\partial P_\zeta}$$

Since H is an explicit function of $(v_\|, \psi, \zeta, \theta)$, we calculate the partial derivatives of H through the chain rule based on the coordinate transformation from $x_k(P_\theta, P_\zeta, \zeta, \theta)$ to $y_k(v_\|, \psi, \zeta, \theta)$. The transformation between x_k and y_k is

$$\left|\frac{\partial x_k}{\partial y_j}\right| = \begin{bmatrix} \partial_{v_\|} P_\zeta & \partial_\psi P_\zeta & \partial_\zeta P_\zeta & \partial_\theta P_\zeta \\ \partial_{v_\|} P_\theta & \partial_\psi P_\theta & \partial_\zeta P_\theta & \partial_\theta P_\theta \\ 0 & 0 & 1 & 0 \\ 0 & 0 & 0 & 1 \end{bmatrix}$$

The inverse is

$$M = \left|\frac{\partial y_k}{\partial x_j}\right| = \frac{1}{D} \begin{bmatrix} \partial_\psi P_\theta & \partial_\psi P_\zeta & T_{\psi\zeta} & T_{\psi\theta} \\ \partial_{v_\|} P_\theta & \partial_{v_\|} P_\zeta & T_{\zeta v_\|} & T_{\theta v_\|} \\ 0 & 0 & D & 0 \\ 0 & 0 & 0 & D \end{bmatrix}$$

37

with

$$D = \partial_{v_\parallel} P_\zeta \partial_\psi P_\theta - \partial_{v_\parallel} P_\theta \partial_\psi P_\zeta$$

$$T_{\alpha\beta} = \partial_\alpha P_\zeta \partial_\beta P_\theta - \partial_\alpha P_\theta \partial_\beta P_\zeta$$

Then the equation of motion is

$$\frac{dx_k}{dt} = S_{kj} \frac{\partial H}{\partial x_j}$$

where

$$S = \begin{bmatrix} 0 & 0 & -1 & 0 \\ 0 & 0 & 0 & -1 \\ 1 & 0 & 0 & 0 \\ 0 & 1 & 0 & 0 \end{bmatrix}$$

The transform matrix M allows us to change variables from x_k to y_k to obtain:

$$\frac{dy_k}{dt} = (MSM^T)_{kj} \frac{\partial H}{\partial y_j},$$

or equivalently:

$$\begin{bmatrix} \dot{v}_\parallel \\ \dot{\psi} \\ \dot{\zeta} \\ \dot{\theta} \end{bmatrix} = \frac{1}{D} \begin{bmatrix} 0 & 0 & -\partial_\psi P_\theta & \partial_\psi P_\zeta \\ 0 & 0 & \partial_{v_\parallel} P_\theta & -\partial_{v_\parallel} P_\zeta \\ \partial_\psi P_\theta & -\partial_{v_\parallel} P_\theta & 0 & 0 \\ -\partial_\psi P_\zeta & \partial_{v_\parallel} P_\zeta & 0 & 0 \end{bmatrix} \cdot \begin{bmatrix} \partial_{v_\parallel} H \\ \partial_\psi H \\ \partial_\zeta H \\ \partial_\theta H \end{bmatrix}$$

Note that both sides of the equation are now functions of $(v_\parallel, \psi, \zeta, \theta)$ on the orbit. We now denote $B_\theta/B_0 = I, B_\zeta/B_0 = g$, and $A_\zeta = -\chi, A_\theta = \int q\chi' d\psi$, after which then the last two equations of motion become:

$$\dot{\zeta} = \frac{1}{D}(q\chi' + v_\parallel \partial_\psi I)v_\parallel - I\mu \partial_\psi B_0,$$

$$\dot{\theta} = \frac{1}{D}(\chi' - v_\parallel \partial_\psi g)v_\parallel + g\mu \partial_\psi B_0.$$

These expressions can be used to calculate the frequencies of the toroidal and poloidal orbital motion. This set of equations of motion exactly conserves the Hamiltonian. In the Roscoe White's book [48], the equations of motion are similar, but the equilibrium field is expressed in non-canonical Boozer coordinates[9]. As a result, the equations involve an additional time derivative term associated with $\dot{\psi}$. This inconvenient contribution was artificially ignored to use the Hamiltonian formalism, which affects calculations of particle orbits and frequencies.

For guiding center motion in the unperturbed field, energy E, magnetic moment μ, and toroidal angular momentum P_ζ are conserved quantities and determine the guiding center orbit. The only possible ambiguity is whether particle moves along or oppose to the magnetic field. Given (E, P_ϕ, μ), the parallel velocity is

$$v_\parallel = \pm \sqrt{2E - 2\mu B_0(\psi, \theta)}$$

the plus and minus sign depends on the particle direction. If the magnetic moment is small, parallel velocity preserves its sign and the guiding center motion will be mostly along the magnetic field, with small deviation that comes from the drift motion. These particles are called passing particles, and we use "copassing" to refer to particle steaming along the magnetic field, and "conterpassing" referring to the particles move opposite to the magnetic field. In the axisymmetic case, we can project their orbit from 3D torus geometry to the poloidal cross section with fixed toroidal angle(namely "Poincaré map"), the projection will be simply a closed curve or a single point.
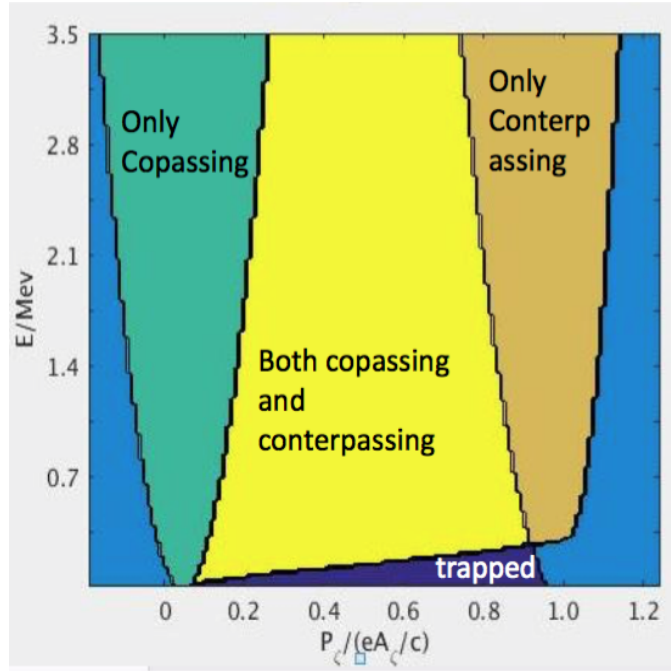
Figure 5.1: Different orbit types in tokamak field. The magnetic field parameters are close to the ITER configuration. We fix the value of μ and simulate particles with different toroidal angular momentum and Energy(up to 3.5 Mev). Banana particles vanish when the total energy E increase (which stands for higher parallel velocity).

The guiding center motion with large magnetic moment is more complicated. As we see from the previous expression, the parallel velocity is a rather complicated function of the magnetic field configuration. In particular, for the nonuniform magnetic field on the tokamak poloidal plane, guiding center motion with large magnetic moment are reflected by field gradients and prevented from penetrating the stronger field side. These particles are called "banana particles". The meaning of their name becomes transparent when we look at

40

the guiding center orbit projection on the poloidal plane. The magnetic field works as a potential well, so the banana orbit is trapped to the outer board region with weaker field and cannot finish a complete circle. As the particle parallel velocity reverses sign at the turning point $\theta = \theta_b$, the bounce motion combined with drift motion across magnetic field forms a crescent shape in the poloidal plane [48, 24].
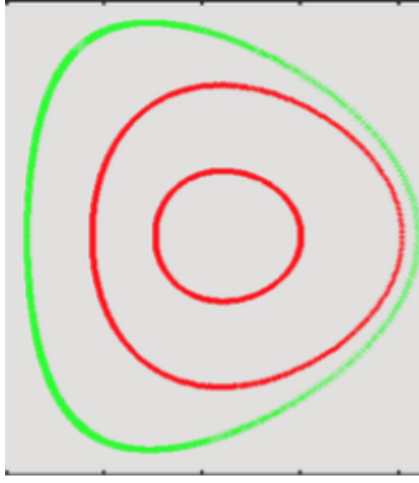
Figure 5.2: Poincaré map of passing particles in the tokamak cross section, with the plasma boundary shown by green lines.

To calculate the guiding center orbit, we can also use the conserved quantities. For P_ϕ to be conserved, we can interpolate to find ψ_i for a given θ_i on the orbit. For banana orbits,

$$
\begin{aligned}
P_\phi &= \frac{A_\phi(\psi_{i+}, \theta_i)}{c} + \sqrt{\frac{2E - 2\mu B_0(\psi_{i+}, \theta_i)}{m}} \frac{B_\phi(\psi_{i+}, \theta_i)}{B_0(\psi_{i+}, \theta_i)} \\
&= \frac{A_\phi(\psi_{i-}, \theta_i)}{c} - m\sqrt{\frac{2E - 2\mu B_0(\psi_{i-}, \theta_i)}{m}} \frac{B_\phi(\psi_{i-}, \theta_i)}{B_0(\psi_{i-}, \theta_i)}
\end{aligned}
$$

41
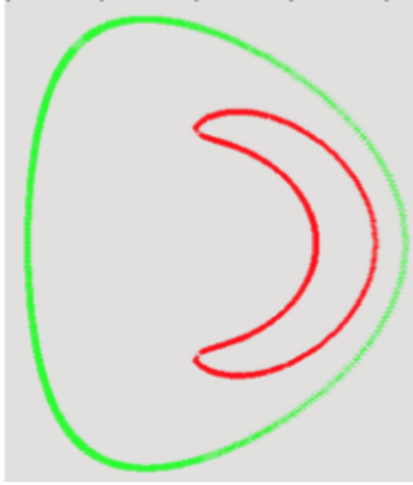
Figure 5.3: Poincaré map of banana particles in the tokamak cross section

Here B_0 is the equilibrium magnetic field. ψ_{i+} stands for the outer branch for the banana particles and ψ_{i-} stands for the inner branch. Similarly we can interpolate to find the trajectory of passing particles. Once the orbit is calculated, we can find $v_\parallel$ and P_θ on every point of the orbit. By integrating along the orbit(for example using $\int dt = \int 1/\dot\theta(\theta)d\theta$), we can easily find $\theta(t)$ and $\zeta(t)$. Note that in the integration, $\dot\theta(\theta)$ vanishes at the turning point of banana particle. This singularity is integrable as the kernel is of type $\int 1/\sqrt{1-x}dx$ at the turning point.

5.1.3 Construction of action-angle variables for the unperturbed motion

Without perturbed field, the guiding center motion is fully integrable. In this section we find the transformation from the explicit variables $(v_\parallel, \psi, \theta, \zeta)$

to the action-angle variables for unperturbed guiding center motion. Among the momenta, μ and P_ζ are already conserved action variables. We then only need to find the action variable for θ:

$$\tilde{P}_\theta = \int_c P_\theta d\theta,$$

where the integral is along the particle orbit. Specifically, for passing particles, the integration is from 0 to 2π; for trapped particles, the motion in poloidal plane is limited from θ_l to θ_u. Supposing the new angles are $\tilde{\theta}, \tilde{\zeta}, \tilde{\xi}$, the generating function is

$$G = \zeta \tilde{P}_\zeta + \zeta \frac{mc}{e} \tilde{\mu} + \int_0^\theta P_\theta [\tilde{H}; \tilde{P}_\zeta; \tilde{\mu}; \theta] d\theta \tag{5.4}$$

Then we can relate the transformed quantities through the generating function [7]. We keep the other two action-μ and P_ζ-since they are already constants of motion:

$$P_\zeta = \frac{\partial G}{\partial \zeta} = \tilde{P}_\zeta$$

$$\mu = \frac{e}{mc} \frac{\partial G}{\partial \zeta} = \tilde{\mu}$$

The angles after transformation then become:

$$\tilde{\theta} = \frac{\partial G}{\partial \tilde{P}_\theta} = \frac{\partial}{\partial \tilde{P}_\theta} \int_0^\theta P_\theta [\tilde{H}; \tilde{P}_\zeta; \tilde{\mu}; \theta] d\theta = \int_0^\theta \frac{\partial P_\theta}{\partial H} \frac{\partial H}{\partial \tilde{P}_\theta} d\theta = \int_0^\theta \frac{\dot{\tilde{\theta}}}{\dot{\theta}} d\theta$$

$$\tilde{\zeta} = \frac{\partial G}{\partial P_\zeta} = \zeta + \frac{\partial}{\partial P_\zeta} \int_0^\theta P_\theta [\tilde{H}; \tilde{P}_\zeta; \tilde{\mu}; \theta] d\theta = \zeta + \int_0^\theta [\frac{\dot{\tilde{\zeta}}}{\dot{\theta}} + \frac{\partial P_\theta}{\partial P_\zeta}|_H] d\theta$$

$$\tilde{\xi} = \frac{\partial G}{\partial \mu} = \xi + \frac{\partial}{\partial \mu} \int_0^\theta P_\theta [\tilde{H}; \tilde{P}_\zeta; \tilde{\mu}; \theta] d\theta = \xi + \int_0^\theta [\frac{\dot{\tilde{\xi}}}{\dot{\theta}} + \frac{\partial P_\theta}{\partial \mu}|_H] d\theta$$

43

If we plot the original toroidal and poloidal angles on particle orbits as functions of time, there will be a linear part and an oscillating part. After the canonical transformation, the angles are linear functions of time from 0 to 2π.

An easier approach can be used to construct the coordinate transformation. Following the previous equations of motion, given E, P_ζ, μ, there is a unique guiding center orbit and we can find $(\psi(t), \theta(t), \zeta(t), v_\parallel(t))$ as well as the frequencies $(\omega_\theta, \omega_\zeta)$. Note in the action-angle variables, $\tilde{\theta} = \omega_\theta t, \tilde{\zeta} = \omega_\zeta t$, which we can use to replace the dependence on time in the original angles. Therefore, we use the one-to-one correspondence between angles and time to get:

$$\psi = \psi(\tilde{P}_\theta, \tilde{P}_\zeta, t(\tilde{\theta}))$$

$$\theta = \theta(\tilde{P}_\theta, \tilde{P}_\zeta, t(\tilde{\theta}))$$

$$v_\parallel = v_\parallel(\tilde{P}_\theta, \tilde{P}_\zeta, t(\tilde{\theta}))$$

$$\zeta = \zeta(\tilde{P}_\theta, \tilde{P}_\zeta, t(\tilde{\zeta}))$$

which forms the transformation from $(v_\parallel, \psi, \theta, \zeta)$ to $(\tilde{P}_\zeta, \tilde{P}_\theta, \tilde{\theta}, \tilde{\zeta})$.

5.2 Scheme to calculate kinetic response of resonance particles to perturbed field

5.2.1 Particle Hamiltonian with perturbed field

In the previous section, we constructed the action-angle variables for the unperturbed motion. In order to use the equilibrium action angle variables for the wave-particle interaction model, we need to express the perturbed

Hamiltonian in terms of the unperturbed canonical variables.

The guiding center Lagrangian in perturbed field is

$$\mathrm{L} = \left(\frac{e}{c}\mathbf{A} + mv_\parallel \frac{\mathbf{B}}{B}\right) \cdot \dot{\mathbf{X}} + \frac{mc}{e}\mu\dot{\xi} - \mu B - \frac{1}{2}mv_\parallel^2 - e\Phi$$

We assume the general form of $\mathbf{A} = \mathbf{A}_0 + \delta\mathbf{A}$, $\mathbf{B} = \mathbf{B}_0 + \delta\mathbf{B}$, in this case the non-canonical piece $\dot{\psi}$ will appear, which makes it difficult to achieve the Hamiltonian formalism. However, note that wave amplitude is still small compared to the strong equilibrium field. This enables us to use the expansion with respect to the perturbed field and the canonical perturbation theory to simplify the problem.

To obtain the Hamiltonian with the perturbed field, we search for the appropriate coordinates, like the canonical straight field line coordinates for the unperturbed field. Given the specific form of perturbation, we try to change (ψ, θ, ζ) to $(\psi, \theta_n, \zeta_n)$ to eliminate the ψ components of $\mathbf{A}$ and $\mathbf{B}$ in the Lagrangian. Let

$$\theta = \theta_n + f(\psi, \theta_n, \zeta_n, t)$$

$$\zeta = \zeta_n + g(\psi, \theta_n, \zeta_n, t)$$

and assume that ψ components vanishes in the new coordinates. According to expression for the vector potential and magnetic field before and after the coordinate transformation:

$$\mathbf{A} = \mathbf{A}_0 + \delta\mathbf{A} = A_\theta^n \nabla\theta_n + A_\zeta^n \nabla\zeta_n,$$

$$\mathbf{B} = \mathbf{B}_0 + \delta\mathbf{B} = B_\theta^n \nabla\theta_n + B_\zeta^n \nabla\zeta_n,$$

f and g need to satisfy:

$$f = \int \frac{\delta A_\psi B_{0\zeta} - \delta B_\psi A_{0\zeta}}{A_{0\zeta} B_{0\theta} - A_{0\theta} B_{0\zeta}} d\psi$$

$$g = \int \frac{\delta B_\psi A_{0\theta} - \delta A_\psi B_{0\theta}}{A_{0\zeta} B_{0\theta} - A_{0\theta} B_{0\zeta}} d\psi$$

The modification in the poloidal and toroidal angles are small and proportional to the perturbation. Due to the small change of variables, the equilibrium fields are also slightly different from the original expressions, for example:

$$A_\theta^n(\theta_n, \zeta_n) = A_\theta^n(\theta, \zeta) + \frac{\partial A_\theta^n}{\partial \theta}(\theta_n - \theta) + \frac{\partial A_\theta^n}{\partial \zeta}(\zeta_n - \zeta) = A_\theta^n(\theta, \zeta)$$

$$\mathbf{b}(\theta_n, \zeta_n) = \frac{\mathbf{B}(\theta_n, \zeta_n)}{B(\theta_n, \zeta_n)} = [b_\theta + \delta b_\theta + b_\theta \frac{\partial f}{\partial \theta} + b_\zeta \frac{\partial g}{\partial \theta} + \frac{\partial b_\theta}{\partial \theta} f] \nabla \theta_n$$
$$+ [b_\zeta + \delta b_\zeta + b_\zeta \frac{\partial g}{\partial \zeta} + b_\theta \frac{\partial f}{\partial \zeta} + \frac{\partial b_\zeta}{\partial \theta} f] \nabla \zeta_n$$

With the new coordinates (θ_n, ζ_n), we can express the Lagrangian in the Hamiltonian form (similar to the unperturbed guiding center motion). The Lagrangian in the new coordinates is

$$L = (\frac{e}{c} A_\theta^n + m v_\| b_\theta^n) \nabla \theta_n \cdot \dot{\mathbf{X}} + (\frac{e}{c} A_\zeta^n + m v_\| b_\zeta^n) \nabla \zeta_n \cdot \dot{\mathbf{X}} + \frac{mc}{e} \mu \dot{\xi}$$
$$- \mu B - \frac{1}{2} m v_\|^2 - e\Phi$$

Note that our change of coordinates involves time, so

$$\nabla \theta_n \cdot \dot{\mathbf{X}} = \dot{\theta}_n - \frac{\partial \theta_n}{\partial t} = \dot{\theta}_n + \frac{\partial f}{\partial t}$$

46

which transforms the Lagrangian to

$$
\begin{aligned}
L =& (\frac{e}{c}A_\theta^n + mv_\parallel b_\theta^n)\dot{\theta}_n + (\frac{e}{c}A_\zeta^n + mv_\parallel b_\zeta^n)\dot{\zeta}_n + \frac{mc}{e}\mu\dot{\xi} - \mu B - \frac{1}{2}mv_\parallel^2 - e\Phi \\
&+ (\frac{e}{c}A_\theta^n + mv_\parallel b_\theta^n)\frac{\partial f}{\partial t} + (\frac{e}{c}A_\zeta^n + mv_\parallel b_\theta^n)\frac{\partial g}{\partial t} \\
=& P_{\theta n}\dot{\theta}_n + P_{\zeta n}\dot{\zeta}_n + \frac{mc}{e}\mu\dot{\xi} - H
\end{aligned}
$$

According to this Hamiltonian form, we can get the corresponding canonical momenta. Compared to the unperturbed motion, the modifications in canonical momenta are:

$$
\begin{aligned}
\Delta P_\theta =& mv_\parallel\frac{\partial(b_\theta)}{\partial\theta}f + \frac{e}{c}(A_{0\theta}\frac{\partial f}{\partial\theta} + A_{0\zeta}\frac{\partial g}{\partial\theta} + \delta A_\theta) \\
&+ mv_\parallel(b_{0\theta}\frac{\partial f}{\partial\theta} + b_{0\zeta}\frac{\partial g}{\partial\theta} + \delta b_\theta) \\
\Delta P_\zeta =& mv_\parallel\frac{\partial b_\zeta}{\partial\theta}f + \frac{e}{c}(A_{0\theta}\frac{\partial f}{\partial\zeta} + A_{0\zeta}\frac{\partial g}{\partial\zeta} + \delta A_\zeta) \\
&+ mv_\parallel(b_{0\theta}\frac{\partial f}{\partial\zeta} + b_{0\zeta}\frac{\partial g}{\partial\zeta} + \delta b_\zeta)
\end{aligned}
$$

Here we use the fact that A_θ and A_ζ are independent of θ, and the system is toroidally symmetric.

As a result, the perturbed fields will change the Hamiltonian as well as the canonical variables. The new Hamiltonian is:

$$
\begin{aligned}
H(P_{\theta n}, P_{\zeta n}, \mu, \theta_n, \zeta_n) =& \mu B + \frac{1}{2}mv_\parallel^2 + e\Phi - (\frac{e}{c}A_\theta^n + mv_\parallel b_\theta^n)\frac{\partial f}{\partial t} \\
&- (\frac{e}{c}A_\zeta^n + mv_\parallel b_\zeta^n)\frac{\partial g}{\partial t}
\end{aligned} \tag{5.5}
$$

with the variables

$$\theta_n = \theta - f(\psi, \theta, \zeta, t)$$

$$\zeta_n = \zeta - g(\psi, \theta, \zeta, t)$$

$$P_{\theta n} = P_\theta + \Delta P_\theta(v_\parallel, \psi, \theta, \zeta, t)$$

$$P_{\zeta n} = P_\zeta + \Delta P_\zeta(v_\parallel, \psi, \theta, \zeta, t)$$

where $(\theta, \zeta, P_\theta, P_\zeta)$ are the set of canonical variables for unperturbed motion.

Note that all modifications from the perturbed field are linearly proportional to the perturbation $(\Delta B / B)$. Ideally we need to take into account the modification of canonical variables, which means recalculating the particle orbit in the presence of perturbation. However, for resonant particles, we are able to use the unperturbed guiding center orbit instead. The reason is that perturbation in Hamiltonian is proportional to $\Delta B / B$, which can result in the change in momentum of order $\sqrt{\Delta B / B}$. Thus, we can only focus on the modification in the Hamiltonian, and characterize the resonant particles by their unperturbed orbits.

To write the new Hamiltonian in terms of the unperturbed orbit quantities, the first contribution comes directly from the perturbed field:

$$\Delta H_1 = \mu(B - B_0) + e\Phi - (\frac{e}{c} A_{0\theta} + mv_\parallel b_\theta)\frac{\partial f}{\partial t} - (\frac{e}{c} A_{0\zeta} + mv_\parallel b_\zeta)\frac{\partial g}{\partial t}.$$

We also need to take into account modification of the coordinates from $(P_\theta, P_\zeta, \theta, \zeta)$ to $(P_{\theta n}, P_{\zeta n}, \mu, \theta_n, \zeta_n)$. We keep the first order term and get:

$$H_0(P_{\theta n}, P_{\zeta n}, \mu, \theta_n, \zeta_n) = H_0(P_\theta, P_\zeta, \mu, \theta) + \frac{\partial H_0}{\partial P_\theta}\Delta P_\theta + \frac{\partial H_0}{\partial P_\zeta}\Delta P_\zeta - \frac{\partial H_0}{\partial \theta} f.$$

here $H_0(P_\theta, P_\zeta, \mu, \theta)$ means the exact unperturbed Hamiltonian in the equilibrium field. Thus the total perturbed Hamiltonian in terms of the unperturbed coordinates is

$$
\begin{aligned}
H_1(P_\theta, P_\zeta, \mu, \theta, \zeta) =& \mu(B - B_0) + e\Phi - P_\theta(\frac{\partial f}{\partial t} + \frac{\partial H_0}{\partial P_\theta}\frac{\partial f}{\partial \theta} + \frac{\partial H_0}{\partial P_\zeta}\frac{\partial f}{\partial \zeta}) \\
& - P_\zeta(\frac{\partial g}{\partial t} + \frac{\partial H_0}{\partial P_\theta}\frac{\partial g}{\partial \theta} + \frac{\partial H_0}{\partial P_\zeta}\frac{\partial g}{\partial \zeta}) \\
& + \frac{\partial H_0}{\partial \theta}f - \frac{\partial H_0}{\partial P_\theta}[mv_\parallel\frac{\partial b_\theta}{\partial \theta}f + \frac{e}{c}\delta A_\theta + mv_\parallel\delta b_\theta] \\
& - \frac{\partial H_0}{\partial P_\zeta}[mv_\parallel\frac{\partial b_\zeta}{\partial \theta}f + \frac{e}{c}\delta A_\zeta + mv_\parallel\delta b_\zeta]
\end{aligned}
\tag{5.6}
$$

In this way, we can separate the Hamiltonian into two parts: the unperturbed part which is completely integrable, and the small perturbation part that comes from the perturbed field. This description is valid for resonant particles when perturbation is small and greatly simplifies our discussion. We ignore the inaccuracy in the coordinate transformation for the resonance dynamics, and use equilibrium orbits to describe energetic particle transport.

5.2.2 Reduction to one dimensional motion for resonance particles

The constructed Hamiltonian and the action-angle variable transformation makes it immediately clear that the resonant particle dynamics can be reduced to one dimensional.

Suppose we have the MHD response in the form

$$
\delta A_\psi = \Sigma \delta A_{\psi m}\frac{1}{\sqrt{2\pi}}\exp\{im\theta - in\zeta\}
$$

49

We can then find f and g and thus the perturbed Hamiltonian. The particle Hamiltonian can be split into the unperturbed part (H_0) and perturbed part (H_1), both in terms of the unperturbed canonical variables,

$$H = H_0(P_\theta, P_\zeta, \theta, \mu) + H_1(P_\theta, P_\zeta, \theta, \zeta, \mu).$$

Since we are considering the equilibrium orbit, we can use the action-angle variables for unperturbed guiding center motion. In these variables, it is easy to identify the resonant particles through the resonance condition. In the general case where the mode frequency chirps, we sum over all the resonances and write the total Hamiltonian in the form:

$$H = H_0(\tilde{P}_\theta, P_\zeta, \mu) + \Sigma H_1(\tilde{P}_\theta, P_\zeta, \mu, l_1, l_2) exp(il_1\tilde{\theta} + il_2\tilde{\zeta} - i\int \omega(t)\mathrm{d}t) + c.c.$$

where l_1 and l_2 distinguish different resonances. We assume the case where only one resonance is essential:

$$H = H_0(\tilde{P}_\theta, P_\zeta, \mu) + H_1(\tilde{P}_\theta, P_\zeta, \mu, l_1, l_2) exp(il_1\tilde{\theta} + il_2\tilde{\zeta} - i\omega(t)t) + c.c.$$

here

$$H_1(\tilde{P}_\theta, P_\zeta, \mu, l_1, l_2) = \frac{1}{(2\pi)^2} \int \int \mathrm{e}^{-il_1\tilde{\theta} - il_2\tilde{\zeta}} H'(P_\theta, P_\zeta, \mu, \theta, \zeta) d\tilde{\theta} d\tilde{\zeta}$$

which can be calculated through the integral along the unperturbed orbit. The function H_1 represents a projection of the perturbed electromagnetic field onto the wave-particle resonance, which is the dominant part of the total perturbed Hamiltonian. Furthermore, if the perturbed field has a specific toroidal mode number, for example:

$$\xi(\psi, \theta, \zeta) = \Sigma \xi_m \frac{1}{\sqrt{2\pi}} \exp\{im\theta - in\zeta\},$$

Then l_2 has to be equal to $-n$ for resonance condition, in which case:

$$H_1(P_\theta, P_\zeta, \mu, l_1, -n) = \frac{1}{2\pi} \int e^{-il_1\tilde{\theta}} e^{in(\tilde{\zeta}-\zeta)} \Sigma \frac{1}{\sqrt{2\pi}} e^{im\theta} H'_m(P_\theta, P_\zeta, \mu) d\tilde{\theta} \quad (5.7)$$

Note the angles only appear as a combination in the perturbed Hamiltonian, we consider the canonical transformation with new angle

$$q = l_1\tilde{\theta} + l_2\tilde{\zeta},$$

and corresponding new momentum is

$$p = \alpha\tilde{P}_\theta + \beta P_\zeta.$$

In order for the transformation to be canonical, the other pair of variables are:

$$J = l_1 P_\zeta - l_2\tilde{P}_\theta, Q = -\frac{\zeta}{l_1}.$$

Then the Hamiltionian becomes

$$H = H_0(J, p, \mu) + H_1(J, p, \mu, l_1, -n) exp(-iq - i \int \omega(t) dt),$$

which is a periodic function of the phase q only. We can see that the quantities J as well as μ are constants of motion in this Hamiltonian, allowing a simplified 1D dynamics for resonant particles. In this description, the distribution of the ambient passing particles remains unperturbed, thus the corresponding kinetic equation is unnecessary to solve numerically. Near the resonance frequency, there is a trapped area of width proportional to the square root of the perturbation amplitude, in which the trapped resonant particles form a locally

51

flat distribution. During the frequency sweeping event, the trapped resonant particles preserve the value of their distribution function when the resonance carries them along the constant J lines in phase space, where $J = l_1 P_\zeta - l_2 \tilde{P_\theta}$.
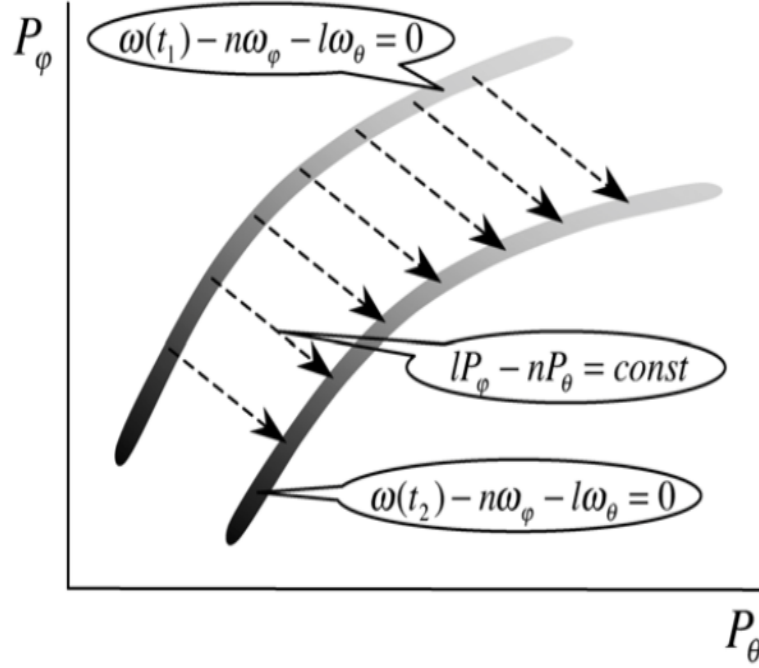
Figure 5.4: Schematic plot of resonant particle transport during frequency sweeping. The shaded areas are resonant region in the momentum space. The trapped resonant particles form a locally flat distribution across the resonance and preserve the value of their distribution function along the dashed lines when frequency chirps. From Ref. [10].

With the new Hamiltonian expressed in (J, p, q, Q), the kinetic equation can be simplified. We first ignore collisions, then the governing equation for

resonance particle distribution function $f(J, p, q, Q)$ is

$$\frac{\partial f}{\partial t} + \frac{\partial H_0}{\partial \tilde{P}_i} \frac{\partial f}{\partial \tilde{Q}_i} - \frac{\partial H_0}{\partial \tilde{Q}_i} \frac{\partial f}{\partial \tilde{P}_i} + \frac{\partial H_1}{\partial \tilde{P}_i} \frac{\partial f}{\partial \tilde{Q}_i} - \frac{\partial H_1}{\partial \tilde{Q}_i} \frac{\partial f}{\partial \tilde{P}_i} = 0$$

Here, the advantage of using Hamiltonian in convection terms is to conserve the particle flow in phase space. We separate the equilibrium distribution and perturbed distribution: $f = F_0 + \delta f$. For energetic particles, the equilibrium distribution F_0 needs to be a function of the constants of motion (J, p, μ). Thus the equation for δf is

$$\frac{\partial \delta f}{\partial t} + \frac{\partial H_0}{\partial J} \frac{\partial \delta f}{\partial Q} + \frac{\partial H_0}{\partial p} \frac{\partial \delta f}{\partial q} + \frac{\partial H_1}{\partial J} \frac{\partial \delta f}{\partial Q} + \frac{\partial H_1}{\partial p} \frac{\partial \delta f}{\partial q} - \frac{\partial H_1}{\partial q} \frac{\partial \delta f}{\partial p} = \frac{\partial H_1}{\partial q} \frac{\partial F_0}{\partial p}$$

Note that H_0 and H_1 doesn't depend on Q, then we can average to eliminate Q dependence and get $< \delta f > (J, p, q)$:

$$\frac{\partial < \delta f >}{\partial t} + \frac{\partial H_0}{\partial p} \frac{\partial < \delta f >}{\partial q} + \frac{\partial H_1}{\partial p} \frac{\partial < \delta f >}{\partial q} - \frac{\partial H_1}{\partial q} \frac{\partial < \delta f >}{\partial p} = \frac{\partial H_1}{\partial q} \frac{\partial F_0}{\partial p}$$

After further simplification since J is constant:

$$\frac{\partial < \delta f >}{\partial t} + (l_2 \omega_\zeta + \frac{\partial H_1}{\partial p}) \frac{\partial < \delta f >}{\partial q} - \frac{\partial H_1}{\partial q} \frac{\partial < \delta f >}{\partial p} = \frac{\partial H_1}{\partial q} \frac{\partial F_0}{\partial p}. \quad (5.8)$$

This equation is greatly simplified for the resonant particles. Once we get the distribution in terms of (J, p, q), it is easy to recover $\delta f(J, p, q, Q)$ as a uniform function on Q. This resonant particle response will then enter the MHD equations in the form of external current or pressure, in order to get the frequency sweeping rate through power balance equation.

5.2.3 Progress in the numerical procedure

The objective of the numeric module is to evaluate the resonance parti-
cle interaction with waves, for which the kinetic equation of resonant particles
is solved as well as the MHD module. The canonical straight field line coordi-
nates are used both for the MHD part and the resonant particle calculation.

In the kinetic module, we focus on the 1D dynamics of trapped resonant
particle as discussed before, in terms of the variables (J, p, q, Q) that derive
from the action angle variables. Note that the resonance Hamiltonian actually
projects the perturbed electromagnetic field from real space coordinates to
the action-angle coordinates, and the perturbed distribution function needs to
be described back in the real space coordinates for the MHD module. It is
therefore necessary to implement coordinate transformation from action-angle
variables to the real space numerically.

Table 5.1: Normalization of physical quantities

Physical quantity	Normalization constant
time	$eB_R/(mc)$
length	R_0
velocity	$mc/(eB_RR_0)$
magnetic field	B_R
vector potential	B_RR_0
energy	$e^2B_R^2/(m^3c^2R^2)$

For simplicity, we normalize the physical quantities according to table

5.1. Then the particle Lagrangian becomes:

$$P_\theta' = A_\theta' + v_\parallel' \frac{B_\theta}{B_0}$$

$$P_\zeta' = A_\zeta' + v_\parallel' \frac{B_\zeta}{B_0}$$

and the new Lagrangian is

$$L' = [\mathbf{A}' + v_\parallel' \mathbf{b}] \cdot \dot{\mathbf{X}}' - H'$$

$$H' = \frac{v_\parallel^2}{2} + \mu' B'; \mu' = \frac{v_\perp^2}{2B'}$$

We build the numerical module that takes (E, P_ζ, μ) (and the type of particle) to generate the guiding center orbits information. The corresponding $(v_\parallel, \psi, \theta, \zeta)$ along the orbits are written as a function of $(\tilde{P}_\theta, P_\zeta, \tilde{\theta}, \tilde{\zeta})$. Thus, this procedure implies the coordinate mapping from $(v_\parallel, \psi, \theta, \zeta)$ to $(\tilde{P}_\theta, P_\zeta, \tilde{\theta}, \tilde{\zeta})$. For our calculations of variables (J, p, μ) (where $J = l_1 P_\zeta - l_2 \tilde{P}_\theta, p = P_\zeta/l_2$), we generate the uniform grid in J since it is constant of motion. The transformation from $(v_\parallel, \psi, \theta, \zeta)$ to $(\tilde{P}_\theta, P_\zeta, \tilde{\theta}, \tilde{\zeta})$ is performed on each grid point.

The coordinate transformation is calculated once, and stored for subsequent use. For example, the coordinate transformation is generated on the grid shown in Fig. 5.5. In the single resonance case, assuming a pair of integers (l_1, l_2), we also plot the resonance line for different frequencies.

The coordinate transformation is used in the process of getting perturbed Hamiltonian on the grid mesh, since the perturbed fields are only functions of real space and need to project to action-angle variables for different resonant particles. Also, after calculation of the kinetic equation in action-angle
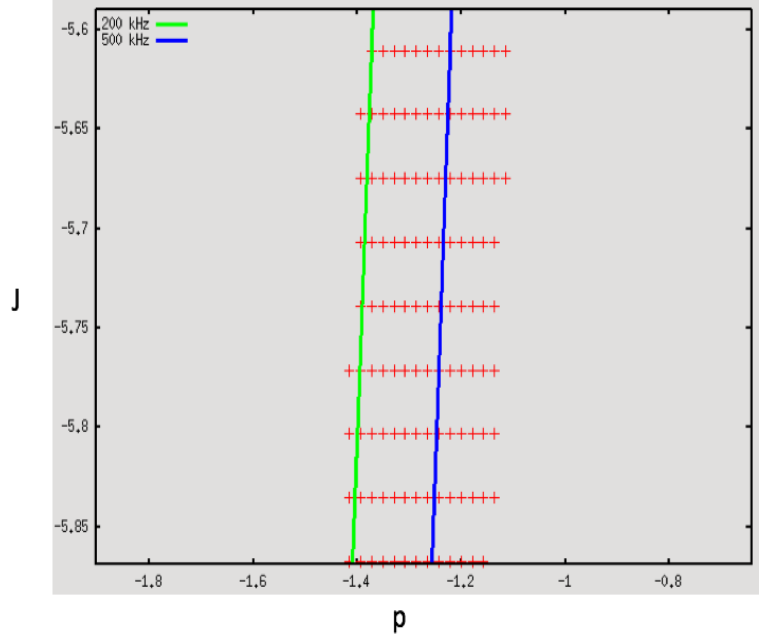
Figure 5.5: The computational grid for calculating the 1D dynamics of the resonant particles with the resonance number $l_1 = 1$ and $l_2 = 1$. The grid is uniform on J and p, since the particles are only allowed to move along the horizontal line (constant J). Resonance center can be found given the wave frequency. For instance, we plot the resonance line for 200 kHz and 500 kHz wave frequency.

variables, as the distribution function needs to be transformed to real space coordinates and integrated to find corresponding pressure or current effect in the MHD equations. Since (J, p, q, Q) are linked to $(P_\theta, P_\zeta, \theta, \zeta)$ by canonical transformation, and we know the transformation matrix from $(P_\theta, P_\zeta, \theta, \zeta)$ to $(v_\parallel, \psi, \zeta, \theta)$. which has the determinant as

$$D = \partial_{v_\parallel} P_\zeta \partial_\psi P_\theta - \partial_{v_\parallel} P_\theta \partial_\psi P_\zeta$$

56

so we can change the distribution function to the real space to calculate energetic particle current.

$$\delta f(v_{\parallel}, \psi, \zeta, \theta) = (\delta f(J, p, q, Q)) * 1/D$$

Up to now, the coordinate transformation module and the kinetic module is finished. AEGIS code is needed for calculation of MHD response, and is modified for the current source and continuum damping. The ongoing effort is to change the ideal MHD code from eigenvalue to initial value code, to calculate the nonlinear wave and particle interaction.

Chapter 6

Summary

Wave and energetic particles interaction often give rise to frequency chirping events and energetic particle transport associated with the formation of coherent structures in phase space. This phenomenon, which has often been described with the electrostatic bump-on- tail model, extends to more general nonlinear evolution regime. In this thesis, we do a series of theoretical and numerical studies along the line to explore the characteristics of energetic particle driven modes. We modify the AEGIS code for the purpose of studying the MHD response in the wave particle interaction model. In particular, the continuum absorption near the TAE gap, which is related to the classical TAE theory, are studied and the results are compared with the simulation. Moreover, canonical straight field line coordinate is proposed for tokamak simulation. We then use the action-angle variables to pinpoint the resonant particle and and show how to generalize the nonlinear bump-on-tail interaction model to a more realistic model in tokamaks.

After an introduction and review of the previous studies on different types of energetic particle and wave interaction, the primary numerical tool, the AEGIS code are introduced and used to analyze the Aflvén cascade in

MST in chapter 2. In the first part of chapter 2, we review the previous studies about the Alfvén cascade instability. The discussion of Aflvén cascade in MST is attached in paper A, in which excellent agreements are obtained between the analytical result from screw pinch model and simulation result with actually experimental equilibrium setup. Besides, further analysis establishes constraints on the safety factor and plasma pressure, under which two modes can exist simultaneously.

In chapter 3, driven by the need to describe continuum absorption in the frequency sweeping events, we examine the dissipation response of the Alfvén continuum to external source with frequency slightly outside the edges of toroidicity-induced spectral gap. The main challenge of this problem is the toroidicity induced coupling between neighboring poloidal components. Inspired by the classical TAE theory, we use the singular perturbation technique near the gap in our theoretical calculation. The AEGIS scheme is changed accordingly to resolve continuum absorption. The result of our study is present in paper B, where different continuum absorption features are found near the upper and lower tip, associated with the characteristics of nearby TAEs.

The discovery of the new global straight field line coordinates for a toroidal plasma configuration is described in chapter 4. The new coordinate system provides a canonical description of particle guiding center motion while maintaining the straight field line feature. These coordinates are convenient for combining MHD calculations with kinetic modeling of energetic particles. We demonstrate how the new coordinate system can be constructed by trans-

forming the poloidal and toroidal angles, along with verification of the new coordinate in paper C.

In chapter 5, we build the wave particle interaction model in action-angle variables in realistic tokamaks. The objective is to focus on the Hamiltonian for a small group of resonant particles adiabatically in 1 dimensional phase space, as the region distant from the resonant structures has little effect on the most critical nonlinear behavior. We start by calculating unperturbed guiding center orbit with the Littlejohn Lagrangian, and get the coordinate transformation to action angle variables on the canonical straight field line coordinates. In the action angle variables, we derive the Hamiltonian formalism in the presence of perturbation, which is effectively 1 dimensional dynamics. The Hamiltonian formalism is helpful to calculate kinetic equation and get the Liouville flow in particle phase space, so that the resonant particle response can be included in the MHD equations.

The remaining interesting task is to change the ideal MHD eigenvalue code to initial value code, to calculate the nonlinear wave and particle interaction. The scheme to follow the resonant particle dynamics is an initial-value problem, which requires the evolution of the energetic particle distribution function and the wave simultaneously. When the MHD module becomes initial value, the numerical procedure we developed are easy to include the resonant particle effect in the MHD part for analysis of nonlinear wave frequency sweeping events.

Appendices

paper A Alfvén modes in the Madison Symmetric Torus

CrossMark

Alfvén modes in the Madison Symmetric Torus

M. Li,[1] B. N. Breizman,[1] L. J. Zheng,[1] L. Lin,[2] W. X. Ding,[2] and D. L. Brower[2]
[1]*Institute for Fusion Studies, The University of Texas, Austin, Texas 78712, USA*
[2]*Department of Physics and Astronomy, University of California Los Angeles, Los Angeles, California 90095, USA*

This work presents a theoretical and computational analysis of core-localized energetic particle driven modes observed near the magnetic axis in the Madison Symmetric Torus [L. Lin, W. X. Ding, D. L. Brower *et al*., Phys. Plasmas **20**, 030701 (2013)]. Using measured safety factor and plasma pressure profiles as input, the linear ideal MHD code Adaptive EiGenfunction Independent Solution (AEGIS) [L. J. Zheng and M. Kotschenreuther, J. Comput. Phys. **211**, 748 (2006)] reveals Alfvénic modes close to the measured frequencies. The AEGIS results together with a reduced analytical model demonstrate that the modes are essentially "cylindrical" and dominated by a single poloidal component ($m = 1$). The modes are localized at the plasma core where the magnetic shear is weak and continuum damping is minimal. Detailed analysis establishes constraints on the safety factor and plasma pressure, under which two modes can exist simultaneously. © *2014 AIP Publishing LLC*. [http://dx.doi.org/10.1063/1.4891659]

I. INTRODUCTION

Alfvén eigenmodes are ubiquitous in magnetically confined plasmas and can lead to deleterious effects, such as enhanced energy losses.[1,2] They tend to be unstable in the presence of fast ions produced by neutral beams injection, rf heating, or fusion reactions.

Observation and theoretical studies of Alfvén eigenmodes have been extensive for tokamaks[3–7] and stellarators.[8,9] In Reversed Field Pinch (RFP) devices, the weak toroidal field and the distinct configuration—low safety factor and high magnetic shear—are likely to bring interesting variations of Alfvén eigenmodes. However, theoretical studies are less mature for the RFP than they are for tokamaks and stellarators. In particular, recent experimental observations of fast-ion-driven instabilities associated with neutral beam heating on Madison Symmetric Torus (MST), a typical axisymmetric RFP device, call for theoretical analysis.

MST plasmas exhibit bursts of the $n = 4$ and $n = 5$ modes in the Alfvénic frequency range during 1 MW neutral beam injection.[10–12] As seen in Fig. 1 of Ref. 10, both the $n = 4$ and $n = 5$ mode frequencies lie outside the toroidicity induced Alfvén gap, but rather close to the Alfvén continuum ($\omega_A = k_\parallel v_A$) near the magnetic axis. There is a maximum for the $n = 5$, $m = 1$ Alfvén continuum spectrum at $r = 0$ and a minimum for the $n = 4$, $m = 1$ at $r = 0$ (also see Fig. 1). Since the spatial profile of the local Alfvén frequency near magnetic axis is nearly flat and fast ions are located at the plasma core, the axis is a preferred location for hosting localized Alfvén modes. This feature is reminiscent of Global Alfvén Modes[13] or Alfvén Cascades.[14] Toroidicity-induced coupling is less important here than it is for the Toroidal Alfvén Eigenmode (TAE). In this case, it is natural to consider an Alfvénic mode with a single poloidal component ($m = 1$) as a candidate explanation of the experimental observations, and this paper presents such analysis for the modes observed in MST.

Whereas an earlier work[15] stressed the role of pressure gradient, we show that a finite pressure gradient is not a necessary ingredient for the $n = 4$ mode. We also discuss conditions that are required for simultaneous existence of the $n = 4$ and $n = 5$ modes.

We first choose a screw pinch geometry in the MHD model to analyze the mode structure and properties of the $m = 1$ mode. We then use a toroidal equilibrium constructed with Variational Moments Equilibrium Code (VMEC)[16] to simulate the modes using Adaptive EiGenfunction Independent Solution (AEGIS). The paper is organized as follows: In Sec. II A, an equilibrium configuration is introduced for the screw pinch model. In Sec. II B, the mode equation is presented, followed by numerical solution of this equation in Sec. II C. The numerical results from AEGIS are described in Sec. III. The concluding section (Sec. IV) is a brief summary.

II. SCREW PINCH MODEL

A. Screw pinch equilibrium

For simplicity, we first consider cylindrical approximation for the RFP field, because the mode frequency is away from the TAE gap and toroidicity-induced coupling is relatively small for the mode localized at the core.

The ideal MHD equilibrium condition is

$$\mathbf{J} \times \mathbf{B} = \nabla P, \tag{1}$$

where $\mathbf{B}$ is the equilibrium magnetic field, $\mathbf{J}$ is the current density, and P is the plasma pressure.

In the cylindrical case, where $\mathbf{B} = (0, B_\theta, B_z)$ and all equilibrium quantities depend only on radius r, Eq. (1) reduces to

$$-B' - \frac{B_\theta^2}{rB} = \frac{\mu_0 P'}{B}, \tag{2}$$

where μ_0 is the vacuum permeability. Note that the characteristic length L in the z direction in the cylindrical model is
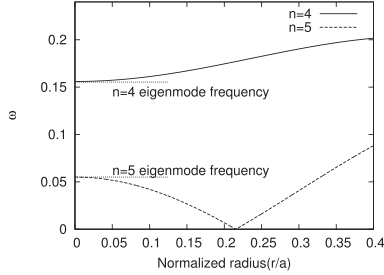
21, 082505-1

63

FIG. 1. The $n=5$, $m=1$, and $n=4$, $m=1$ local Alfvén frequencies versus normalized radius for $q_0 = 0.211$, $\kappa_q = 1.16$, $\beta_0 = 0$, and $\kappa_\beta = 0$. The frequency is normalized by the on-axis Alfvén frequency $v_A/Rq_0 \approx 7.2 \times 10^5$ Hz. The $n=4$ and $n=5$ eigenmode frequencies are marked by dotted lines.

related to the RFP major radius by $L = 2\pi R$. We use $q = rB_z/RB_\theta$ to denote the safety factor, and $\beta = 2\mu_0 P/B^2$ to represent the equilibrium plasma beta, which transforms Eq. (2) to

$$(B^2)' = -\frac{2B_z^2 r}{q^2 R^2} - (\beta B^2)',$$

$$(B^2)' + \frac{2B^2 r}{\left(1 + \dfrac{r^2}{R^2 q^2}\right) q^2 R^2} = -\beta' B^2 - \beta (B^2)'.$$

Consequently, the magnetic field can be written as

$$B^2 = B_0^2 \exp\left\{ -\int_0^r \frac{1}{1+\beta}\left(\beta' + \frac{2r^*}{R^2 q^2 + r^{*2}}\right) dr^* \right\}, \quad (3)$$

where B_0 is the on-axis field and the profiles of q and β are assumed to be given. In the MST experiment, the major radius is $R = 1.5$ m and the minor radius is $a = 0.5$ m. Near the core, we can approximate the MST equilibrium by parabolic profiles of the safety factor, $q = q_0(1 - \kappa_q r^2/a^2)$, and plasma beta, $\beta = \beta_0(1 + \kappa_\beta r^2/a^2)$. The parameter q_0 is the safety factor at the magnetic axis (its experimental value is 0.22, with a 10% error[10]). In what follows, we choose the value of κ_q in such a way that the continuum and the location of the $q = 0.2$ rational surface are close to the experimental data (since the $n = 5$ magnetic island appears in the experiment). Considering the experimental error bars, the value of κ_q can vary from 0.7 to 1.5. We only take into account the bulk plasma beta, which has the value of 0.02 at the magnetic axis ($\beta_0 \approx 0.02$) with a positive gradient near the plasma core in MST case, reflecting radial decrease in the toroidal magnetic field. We ignore the fast ion pressure in this idealized MHD analysis, because significant anisotropy of that pressure requires kinetic treatment for its accurate description. Considering the error bars, we can vary the β gradient parameter κ_β from 0 to 2.5. The near-axis approximations for q and β give the following approximate expressions for the equilibrium magnetic field in the screw pinch model:

$$B = B_0\left(1 - \frac{r^2}{2(\beta_0+1)q_0^2 R^2} - \frac{\beta_0 \kappa_\beta}{2a^2(\beta_0+1)}r^2\right),$$

$$B_z = B_0\left(1 - \frac{(\beta_0+2)r^2}{2(\beta_0+1)q_0^2 R^2} - \frac{\beta_0 \kappa_\beta}{2a^2(\beta_0+1)}r^2\right),$$

$$B_\theta = B_0\left(\frac{r}{Rq_0} - \frac{(\beta_0+2)r^3}{2(\beta_0+1)q_0^3 R^3} + \frac{\kappa_q r^3}{q_0 Ra^2} - \frac{\beta_0 \kappa_\beta r^3}{2a^2(\beta_0+1)q_0 R}\right).$$
$$(4)$$

B. Eigenmode equation

Let $\boldsymbol{\xi} = (\xi_r, \xi_\theta, \xi_z)$ be a small displacement of a plasma element from its equilibrium position. We use a Fourier representation for $\boldsymbol{\xi}$ in the screw-pinch

$$\boldsymbol{\xi}(r, \theta, z, t) = \boldsymbol{\xi}(r)\exp\left[i\left(\omega t + m\theta - \frac{nz}{R}\right)\right],$$

where ω is the mode frequency, m is the poloidal mode number, and n/R is the wave number in the z direction. Starting from the mode equation derived in Ref. 17, we ignore the viscosity terms and obtain the following simplified equation for the perturbed electric potential $\Phi = r\xi_r$:

$$\frac{d}{dr}\left(A(\omega)\frac{d\Phi}{dr}\right) - C(\omega)\Phi = 0, \quad (5)$$

with

$$A(\omega) = \frac{\rho}{r}\frac{(\omega^2 - \omega_a^2)(v_s^2 + v_A^2)(\omega^2 - \omega_h^2)}{D},$$

$$C(\omega) = -\frac{\rho}{r}(\omega^2 - \omega_a^2) + \frac{4n^2 B_\theta^2}{\mu_0 r^3 R^2}\frac{\omega^2 - \omega_g^2}{D}$$
$$+ \frac{d}{dr}\left[\frac{B_\theta^2}{\mu_0 r^2} + \frac{2nGB_\theta}{\mu_0 r^2 DR}(v_s^2 + v_A^2)(\omega^2 - \omega_h^2)\right],$$

$$D = \omega^4 - k_0^2(v_s^2 + v_A^2)\omega^2 + v_s^2 \omega_a^2 k_0^2,$$

$$\omega_a^2 = \frac{F^2}{\mu_0 \rho}, \quad \omega_h^2 = \frac{v_s^2}{v_s^2 + v_A^2}\omega_a^2, \quad \omega_g^2 = \frac{v_s^2}{v_A^2}\omega_a^2,$$

$$v_A^2 = \frac{B^2}{\mu_0 \rho}, \quad v_s^2 = \frac{\gamma P}{\rho},$$

$$F = \frac{mB_\theta}{r} - \frac{nB_z}{R}, \quad G = \frac{mB_z}{r} + \frac{nB_\theta}{R}, \quad k_0^2 = \frac{m^2}{r^2} + \frac{n^2}{R^2},$$

where $v_A = \frac{B}{\sqrt{\mu_0 \rho}}$ is the Alfvén velocity, v_s stands for sound speed, ρ is the equilibrium plasma mass density, and γ refers to the ratio of specific heats. In the zero-beta limit, Eq. (5) reduces to the eigenmode equation derived earlier in Ref. 18. The Alfvén continuum spectrum is given by $\omega = \omega_A = k_\parallel v_A$, where $k_\parallel = \left(\frac{m}{q} - n\right)\frac{B_z}{RB}$.

We restrict our consideration to shear Alfvén modes whose frequencies are much lower than the compressional mode frequency. In addition, we use the near-axis approximation as in Eq. (4) for all equilibrium quantities and ignore the radial dependence of plasma density ρ. The

corresponding simplified expressions for $A(\omega)$ and $C(\omega)$ in Eq. (5) after dividing by B_0^2 are given by

$$A(\omega) = -\frac{r}{m^2}\left(\omega^2 - \omega_a^2\right),$$
$$C(\omega) = -\frac{1}{r}\left(\omega^2 - \omega_a^2\right) + Hr,$$

(6)

where H is a constant that is totally determined by $(q_0, \beta_0, \kappa_q, \kappa_\beta)$

$$H = \frac{2\beta_0\kappa_\beta}{(\beta_0 + 1)a^2q_0^2R^2}\left(\frac{2nq_0}{m} - 1\right) + \frac{4\kappa_q}{a^2R^2q_0^2}\left(1 - \frac{nq_0}{m}\right)$$
$$- \frac{4n^2}{R^4q_0^2m^2}\left(1 - \frac{nq_0}{m}\right) + \mathcal{O}\left(\left(1 - \frac{nq_0}{m}\right)^2\right).$$

Here, we use the fact that $k_\parallel \ll k_0$ and $\beta_0 \ll 1$. In what follows, we set $m = 1$ because the observed mode frequency is close to the $m = 1$ branch of Alfvén continuum in the MST experiment. The coefficient $A(\omega)$ in front of the second-derivative term in Eq. (5) is proportional to r, whereas the non-derivative coefficient $C(\omega)$ contains both $1/r$ and r terms. In the region close to the magnetic axis, the dominant term in $C(\omega)$ is the $1/r$ term and has the same sign as $A(\omega)$. As a result, the perturbed potential Φ of the $m = 1$ mode is proportional to r near the axis. At larger radii, the Hr term becomes more important than the $1/r$ term in $C(\omega)$. If the Hr term changes the sign of $C(\omega)$ relative to $A(\omega)$, we may expect a rollover in Φ and a localized mode near the core.

In the $n = 5$ and $m = 1$ case, the mode in the experiment is above $\omega_A(0)$, so that the coefficient $A(\omega)$ is negative. A positive value of $C(\omega)$ near the core will therefore be favorable for a localized mode to appear above the continuum tip. Since the factor of κ_q in H is negative (mainly determined by $1 - nq_0/m = 1 - 5 \times 0.22 = -0.1$), $C(\omega)$ tends to be positive if q is sufficiently flat and κ_q is small. For the term containing κ_β, the factor in front (i.e., $2nq_0/m - 1$) is positive, so that parameter κ_β should also be large in order to make $C(\omega)$ positive and establish the mode. We thus conclude the nearly flat q profile and positive κ_β help establish the $n = 5$, $m = 1$ mode above the continuum.

On the other hand, when $n = 4$ and $m = 1$, a good candidate mode lies below the minimum of continuum and $A(\omega)$ is positive as a result. Accordingly, $C(\omega)$ should be negative in order for the mode to have the roll over. Since the factor of κ_q (i.e., $1 - nq_0/m$) is now positive, we still expect κ_q to be small to get negative $C(\omega)$ as in the $n = 5$ case. In contrast, the coefficient $(2nq_0/m - 1)$ in front of the pressure gradient term is positive, which suggests that negative values of κ_β should help establish a localized mode.

To summarize, a flattish q profile near the core facilitates mode existence in both $n = 5$ and $n = 4$ cases. But the effects of β gradient are opposite on the two modes: Positive β gradient helps the $n = 5$ but inhibits the $n = 4$ mode and vice versa. The simultaneous existence of the two modes can therefore be viewed as an informative constraint on the q and β profiles within MHD model.

C. Localized modes in the screw pinch core

In this section, we present numerical solutions of the mode equation, Eq. (5), together with sensitivity studies for the $n = 5$, $m = 1$ and $n = 4$, $m = 1$ localized modes.

The core magnetic field in MST is $B = 0.29$ T and the core value of the bulk plasma beta (β_0) is ≈ 0.02. The core electron density, $n_e = 1.0 \times 10^{19} \text{m}^{-3}$, is assumed to be constant in our calculations, and we set $\gamma = 0$ for simplicity. Given the equilibrium profile calculated from Eq. (3), Eq. (5) becomes a second order differential equation that can be solved with a shooting code, starting from the magnetic axis where Φ is proportional to r. A frequency scan is used to find a localized solution for which Φ vanishes at the outer boundary.

We use an artificial outer boundary condition with $\Phi = 0$ before the $q = 0.2$ rational surface. The underlying reason is that the mode frequencies in the MST experiment cross the Alfvén continuum away from the core, as shown in Refs. 10 and 11. This crossing means that any global Alfvén mode ranging from the core to the edge could have significant damping. Additional boundary condition tests show the modes are not sensitive to the position of the boundary. We therefore seek modes that are localized within the core and vanish before the first magnetic island to ensure small continuum absorption.

Using the shooting code for Eq. (5), when β is set to zero, we are able to find both the $n = 4$ and $n = 5$ modes when q is sufficiently flat. Figure 1 shows the continuum spectrum and the mode frequencies for $n = 4$ and $n = 5$ when $q_0 = 0.211$, $\kappa_q = 1.16$ and $\beta = 0$, $\kappa_\beta = 0$. The $n = 5$ mode appears slightly above the continuum tip and the $n = 4$ mode lies below its continuum minimum. The computed $n = 4$ and $n = 5$ mode frequencies are approximately 110 kHz and 42 kHz, respectively, being quite close to the MST experimental observations. The corresponding $n = 5$, $m = 1$ and $n = 4$, $m = 1$ mode structures are plotted in Figs. 2 and 3, respectively. Both modes are localized between the magnetic axis and the $q = 0.2$ rational surface ($r \approx 0.1$ m).

We find that the modes change significantly and can disappear when we vary the q profile and β profile within the
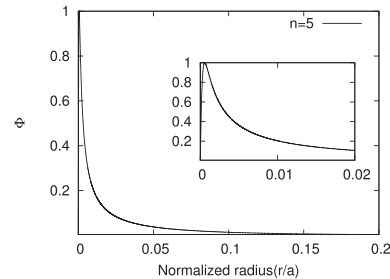

FIG. 2. The $n = 5$, $m = 1$ perturbed electric potential Φ for $q_0 = 0.211$, $\kappa_q = 1.16$, $\beta_0 = 0$, and $\kappa_\beta = 0$. The mode has a rollover very near the core and the mode frequency is 42 kHz.
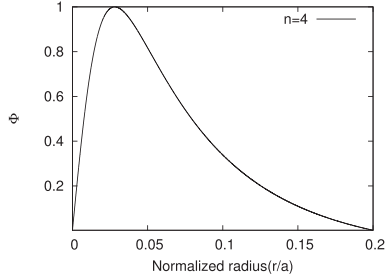
65

FIG. 3. The $n = 4$, $m = 1$ perturbed electric potential Φ for $q_0 = 0.211$, $\kappa_q = 1.16$, $\beta_0 = 0$, and $\kappa_\beta = 0$. The mode frequency is 111 kHz.

experimental error bars. Figure 4(a) shows that the $n = 5$ mode structure becomes more localized when q is steeper (for a given β profile), and that the mode frequency moves closer to the continuum frequency. The $n = 5$ mode eventually disappears when the q profile becomes too steep. In the case of fixed q profile, the $n = 5$ mode disappears when the β gradient parameter κ_β is below some critical positive values, whereas positive κ_β is favorable to the mode (as shown in Fig. 4(b)). Such dependence on q and β gradients agrees

with the conjecture made in Sec. II B and confirms sensitivity of the mode structure and existence to the magnetic shear and plasma beta.

For the $n = 4$, $m = 1$ case, we also change the q and β profiles and find that q profile has the same effect on the structure and existence as in the $n = 5$ case (Fig. 5(a)). However, the effect of β gradient is different: negative gradient helps establish the $n = 4$ mode (Fig. 5(b)) whereas the $n = 4$ mode disappears when the β gradient becomes too positive.

The screw pinch model shows that both the $n = 5$ and $n = 4$ modes appear close to the position where the modes were observed in experiment and have small continuum damping due to their localization in the core. Based on the $n = 4$ and $n = 5$ mode sensitivity study, we confirm the conclusion that a flattish q profile near the core is essential for mode existence within the MHD model but β gradient has opposite effects on these modes. Furthermore, after parameter scan, Fig. 6 gives the range of q and β gradient where both $n = 4$ and $n = 5$ modes can exist when $q_0 = 0.21$ and $\beta_0 = 0.02$.

III. MODES IN TOROIDAL GEOMETRY

The AEGIS code[19] is utilized to extend our analysis to toroidal geometry for more realistic modeling of the observed modes. AEGIS is a linear MHD code with an

FIG. 4. The $n = 5$, $m = 1$ mode structure for various gradients of q and β with $q_0 = 0.207$ and $\beta_0 = 0.02$. In (a), the β gradient is set to be zero and q gradient parameter κ_q changes. (b) Shows the mode structure for different β gradient profiles, while q gradient parameter κ_q remains 0.78.
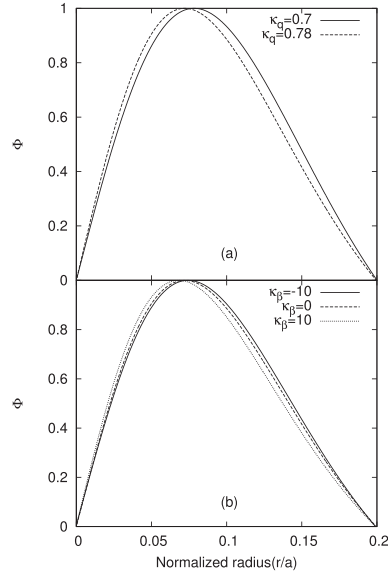

FIG. 5. The $n = 4$, $m = 1$ mode structure for various gradients of q and β, with $q_0 = 0.207$ and $\beta_0 = 0.02$. In (a), the β gradient is fixed ($\kappa_\beta = 0$) and κ_q varies. (b) is for different β gradient profiles and κ_q remains 0.78.
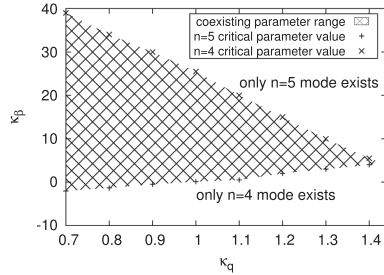
FIG. 6. The parameter window for $n=4$ and $n=5$ modes when $q_0=0.21$, $\beta_0=0.02$. The shaded area marks the coexistence range for the $n=4$ and $n=5$ modes.

adaptive grid mesh in radial direction, and Fourier decomposition in the poloidal and toroidal directions. To solve the radial eigenvalue problem, it constructs an appropriate linear combination of the independent solutions of the Euler-Lagrange equations.

Plasma equilibria are based on the MST experimental data for the safety factor, plasma density and plasma pressure (only bulk plasma beta is taken into account). Equilibrium profiles for all quantities are calculated by
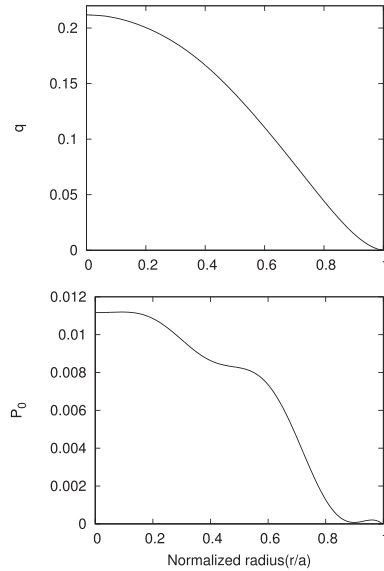
FIG. 7. The safety factor and bulk plasma pressure profiles used as input in AEGIS. The horizontal axis denotes the normalized distance between the magnetic axis and magnetic surface at $\theta=0$.
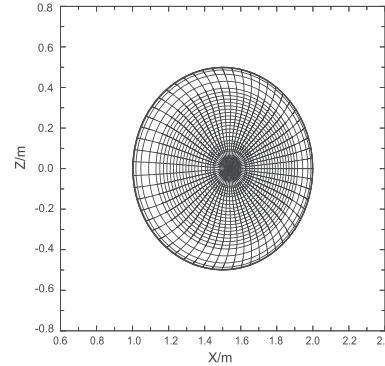
FIG. 8. The coordinate system used in AEGIS, with minor radius 0.5 m. The equilibrium quantities on the grids result from interpolation of the input equilibrium.

VMEC[16] and then adapted to AEGIS input. Figure 7 shows the pressure profile and safety factor profile for one equilibrium. A distinctive feature of MST is that the safety factor is significantly smaller than unity everywhere and that it is nearly flat in the plasma core. The horizontal axis in Fig. 7 labels the normalized distance between the magnetic axis and magnetic surfaces on the outboard side of the midplane. The magnetic surfaces are shown in Fig. 8, and they are nearly circular close to the magnetic axis.

In our simulation, the computational domain extends from the magnetic axis to the nearest magnetic island (i.e., $q=0.2$ rational surface at $r\approx0.1$ m) and has around 300 radial grid points (see Fig. 8). To find the eigenmodes, we use the cylindrical boundary condition $\xi_m\propto r^{m-1}$ for radial displacement at the magnetic axis and set $\xi_m=0$ near the first magnetic island. The mode is assumed to be incompressible in these calculations.
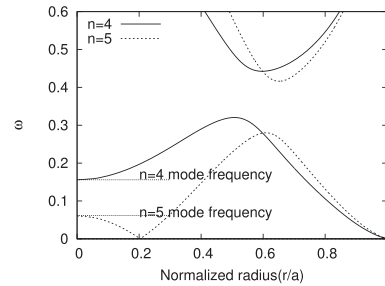
FIG. 9. The $n=5$ and $n=4$ continuum spectra calculated for the equilibrium in Fig. 8, where the frequency is normalized by the on-axis Alfvén frequency $v_A/Rq_0\approx7.2\times10^5$ Hz and the x axis denotes the distance between the magnetic axis and magnetic surface at $\theta=0$. The $n=4$ and $n=5$ eigenmode frequencies are also marked in this figure.

FIG. 10. The $n = 5$ perturbed electric potential Φ_m for the equilibrium in Fig. 8, with the "zoom-in" view of sideband components. The mode frequency is 42 kHz.

FIG. 12. Comparison of the experimental frequency with simulation results for different values of q_0 around 0.21. The shaded area marks the experimental error bars.

After frequency scanning, we find both $n = 5$ and $n = 4$ eigenmodes for the equilibrium in Fig. 7. Figure 9 shows the $n = 4$ and $n = 5$ continuum spectrum and mode frequency, in which the frequency is normalized by the Alfvén frequency $(v_A/Rq_0 \approx 7.2 \times 10^6 \, \text{Hz})$. The continuum and the mode frequencies obtained from AEGIS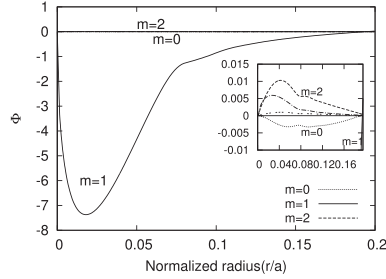 are close to that in the screw pinch model shown in Fig. 1. By checking the $n = 5$ eigenmode (Fig. 10) and $n = 4$ eigenmode (Fig. 11), we observe that the modes are single component dominant and are similar in their radial structure to the localized modes in the screw pinch case, which justifies simplifying assumptions used in Sec. II. We also note that the parameters of the equilibrium in Fig. 7 are in the $n = 5$ and $n = 4$ coexistence range in Fig. 6.

In Ref. 12, the $n = 4$ mode is reported around 120 kHz and the $n = 5$ mode frequency is around 65 kHz in the plasma frame when $q_0 \approx 0.21$. In our simulations, since the modes exist near the continuum, the frequency is sensitive to the safety factor q_0 at the magnetic axis. In the case of $q_0 = 0.211$, the $n = 4$ mode has frequency near 110 kHz and the $n = 5$ mode frequency is 42 kHz. In another equilibrium with $q_0 = 0.218$, the $n = 4$ frequency is 95 kHz and the $n = 5$ frequency is 58 kHz (see Fig. 12). One can therefore approach the observed $n = 4$ and $n = 5$ mode frequencies by choosing an appropriate q_0 value within the experimental error bars.

In addition, the MST experiment shows an $n = 6$, $m = 1$ mode emerges instead of the $n = 5$, $m = 1$ mode when the field reversal parameter decreases and q_0 becomes smaller than 0.2.[12] In our simulation, we use the $q_0 = 0.18$ equilibrium generated with experimental data, and also find the $n = 6$ mode near the measured frequency. The corresponding continuum and the mode structures are plotted in Figs. 13 and 14. The $n = 6$ mode shares many characteristics of the $n = 5$ localized mode. The calculated frequency, 76 kHz, is also sensitive to q_0. The mode frequency will be within the error bars of the experimental value 100 kHz after changing q_0 value.

IV. SUMMARY AND DISCUSSION

In this paper, both cylindrical and toroidal MHD analyses are used to investigate the Alfvén modes in MST. In the cylindrical model, we first consider an analytic equilibrium with parabolic safety factor and plasma pressure (β) profiles, and discuss the effects of those profiles on the modes. We then use a shooting code to solve the eigenmode equation near the plasma core. In the toroidal case, we reconstruct the equilibrium numerically based on MST experimental data. We then use the AEGIS code to study localized modes.
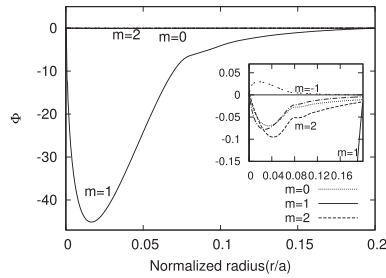

FIG. 11. The $n = 4$ perturbed electric potential Φ_m is plotted for the equilibrium in Fig. 8. The mode frequency is 112 kHz.

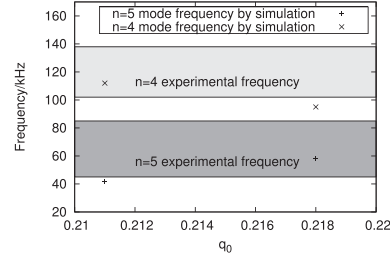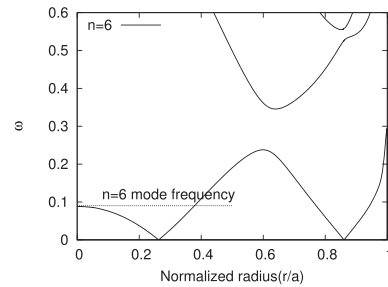FIG. 13. The $n = 6$ continuum spectrum calculated for $q_0 = 0.18$, where the frequency is normalized by the on-axis Alfvén frequency v_A/Rq_0. The $n = 6$ eigenmode frequency is marked by the dotted line in this figure.
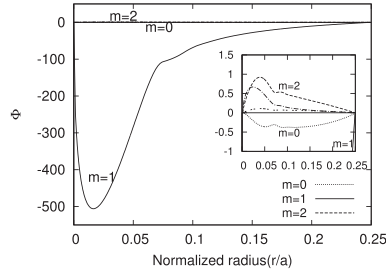
FIG. 14. The n = 6 perturbed electric potential Φ_m. The mode frequency is 76 kHz.

We find coexisting $n = 4$ and $n = 5$ modes in both cylindrical and toroidal calculations. These modes are localized at the core and can therefore have low continuum damping. The mode structure can be affected by safety factor and β gradients and become similar to the experimental modes excited by a population of fast ions.

We also find that coexistence of the $n = 4$ and $n = 5$ modes in the MHD model is possible only within a certain range of plasma pressure gradients. A flattish q profile always helps to establish the $n = 4$ and $n = 5$ modes, but pressure gradient has opposite effects on the modes. The window for pressure gradient where both modes can exist is calculated in the cylindrical model, and our toroidal simulations find the two modes within that window.

As opposed to Ref. 15, we demonstrate that the $n = 4$ mode does not generally require a pressure gradient for its existence. By varying the q profile within the experimental error bars, we find the $n = 4$ mode when there is small or no pressure gradient. Moreover, the pressure gradient cannot be too large, because the existence of the $n = 5$ mode limits the pressure gradient from above.

The $n = 4$ and $n = 5$ mode frequencies are near the experimental frequencies. The $n = 4$ mode resides slightly below the continuum spectrum minimum at the plasma core and the $n = 5$ mode is close to the continuum spectrum maximum at the plasma core. Their frequencies are sensitive to the safety factor value at the plasma core. Considering the

10% uncertainty in q_0, both modes can have frequencies within 15% of the experimental frequencies.

We also find the $n = 6$ localized mode with AEGIS near the experimental frequency. The simulation agrees with the observation that the $n = 6$ mode emerges instead of the $n = 5$ mode when the field reversal parameter decreases in the MST experiment. The $n = 6$ mode shares many characteristics of the $n = 5$ localized mode.

It should be pointed out that our MHD analysis does not capture the kinetic response of the fast ions. We performed an additional AEGIS simulation with an isotropic pressure model for fast ion effect on the equilibrium, and the result shows that both modes still exist and additional $n = 5$ localized modes appear above the continuum. Yet, anisotropy of the fast ion pressure still needs to be incorporated in future work.

Although the MHD model provides a good starting point and we find modes near the observed frequencies in MST, there are still several inconsistencies with current experimental observations. First, the experimentally observed $n = 5$ mode does not have a clear Alfvén scaling (see Fig. 4 from Ref. 10). Another difficulty is presented in Fig. 15 which shows the measured mode frequencies (in the plasma frame of reference) in recent MST experiment (with experimental error bars), as well as the estimated core Alfvén frequencies at the $r = 0$, vs. core safety factor q_0. Although the calculated frequencies at $q_0 \approx 0.21$ are within the experimental error bars, the plot shows that the measured mode frequencies have weaker dependence on the central q value than expected. Additionally, experimentally observed inboard-outboard spatial asymmetry of various modes[12] is an issue not addressed by the present theory.

The existing discrepancies with experiment indicate the need to go beyond the MHD model in future investigations. Also, the role of plasma compressibility and toroidicity-induced coupling between the shear Alfvénic and acoustic modes needs to be assessed for the $q_0 \approx 0.2$ scenario. The key open question is whether fast ions change the mode structure significantly to create the observed inboard-outboard spatial asymmetry.[12] It is also important to investigate the $n = 5$ mode coupling to magnetic island in the $q_0 \approx 0.2$ case. On the other hand, a more accurate q profile measurement is required to resolve the differences between the experimental observations and theoretical results since toroidal field is not measured directly in current experiments.
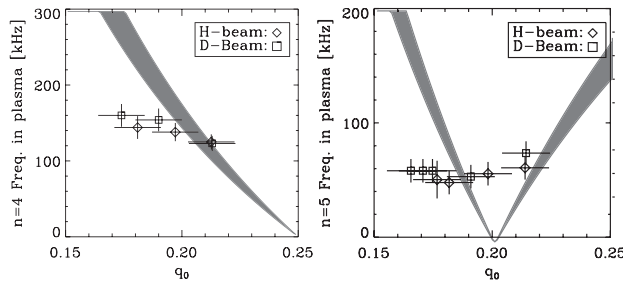
FIG. 15. The $n = 5$ and $n = 4$ measured frequencies versus central q value. The estimated core Alfvén frequencies are in the shaded areas.

ACKNOWLEDGMENTS

[1]K. L. Wong, Plasma Phys. Controlled Fusion **41**, R1 (1999).

[2]ITER Physics Basis, Nucl. Fusion **39**, 2137 (1999).

[3]E. D. Fredrickson, C. Z. Cheng, D. Darrow, G. Fu, N. N. Gorelenkov, G. Kramer, S. S. Medley, J. Menard, L. Roquemore, D. Stutman, and R. B. White, Phys. Plasmas **10**, 2852 (2003).

[4]A. Fasoli, D. Testa, S. Sharapov, H. L. Berk, B. Breizman, A. Gondhalekar, R. F. Heeter, M. Mantsinen, and contributors to the EFDAJET Workprogramme, Plasma Phys. Controlled Fusion **44**, B159 (2002).

[5]B. N. Breizman and S. E. Sharapov, Plasma Phys. Controlled Fusion **53**, 054001 (2011).

[6]W. W. Heidbrink, E. J. Strait, E. Doyle, G. Sager, and R. T. Snider, Nucl. Fusion **31**, 1635 (1991).

[7]F. Zonca, S. Briguglio, L. Chen, S. Dettrick, G. Fogaccia, D. Testa, and G. Vlad, Phys. Plasmas **9**, 4939 (2002).

[8]A. Weller, M. Anton, J. Geiger, M. Hirsch, R. Jaenicke, A. Werner, W7-AS Team, C. Núhrenberg, E. Sallander, and D. A. Spong, Phys. Plasmas **8**, 931 (2001).

[9]Y. I. Kolesnichenko, A. Konies, V. V. Lutsenko, and Y. V. Yakovenko, Plasma Phys. Controlled Fusion **53**, 024007 (2011).

[10]J. J. Koliner, C. B. Forest, J. S. Sarff, J. K. Anderson, D. Y. Liu, M. D. Nornberg, J. Waksman, L. Lin, D. L. Brower, W. X. Ding, and D. A. Spong, Phys. Rev. Lett. **109**, 115003 (2012).

[11]L. Lin, W. X. Ding, D. L. Brower, J. J. Koliner, S. Eilerman, J. A. Reusch, J. K. Anderson, M. D. Nornberg, J. S. Sarff, J. Waksman, and D. Liu, Phys. Plasmas **20**, 030701 (2013).

[12]L. Lin, J. K. Anderson, D. L. Brower, W. Capecchi, W. X. Ding, S. Eilerman, C. B. Forest, J. J. Koliner, D. Liu, M. D. Nornberg, J. Reusch, and J. S. Sarff, Phys. Plasmas **21**, 056104 (2014).

[13]S. M. Mahajan, Phys. Fluids **27**, 2238 (1984).

[14]H. L. Berk, D. N. Borba, B. N. Breizman, S. D. Pinches, and S. E. Sharapov, Phys. Rev. Lett. **87**, 185002 (2001).

[15]H. S. Cai, G. Y. Fu, L. Lin, D. Y. Liu, W. X. Ding, D. L. Brower, and Y. J. Hu, Phys. Plasmas **21**, 022513 (2014).

[16]S. P. Hirshman and J. C. Whitson, Phys. Fluids **26**, 3553 (1983).

[17]S. C. Guo, J. P. Freidberg, and R. Nachtrieb, Phys. Plasmas **6**, 3868 (1999).

[18]K. Appert, R. Gruber, F. Troyuon, and J. Vaclavik, Phys. Plasmas **24**, 1147 (1982).

[19]L. J. Zheng and M. Kotschenreuther, J. Comput. Phys. **211**, 748 (2006).

Paper B Continuum Absorption in the vicinity of the toroidicty-induced Alfvén gap

New Journal of Physics

The open access journal at the forefront of physics

PAPER

Continuum absorption in the vicinity of the toroidicity-induced Alfvén gap

M Li[1,3], **B N Breizman**[1], **L J Zheng**[1] and **Eugene Y Chen**[2]

[1]   Institute for Fusion Studies, The University of Texas, Austin, TX 78712, USA
[2]   DecisionNext Inc., San Francisco, CA 94104, USA
[3]   Author to whom any correspondence should be addressed.

E-mail: mengli@utexas.edu

Abstract

Excitation of Alfvén modes is commonly viewed as a concern for energetic particle confinement in burning plasmas. The 3.5 MeV alpha particles produced by fusion may be affected as well as other fast ions in both present and future devices. Continuum damping of such modes is one of the key factors that determine their excitation thresholds and saturation levels. This work examines the resonant dissipative response of the Alfvén continuum to an oscillating driving current when the driving frequency is slightly outside the edges of the toroidicity-induced spectral gap. The problem is largely motivated by the need to describe the continuum absorption in the frequency sweeping events. A key element of this problem is the negative interference of the two closely spaced continuum crossing points. We explain why the lower and upper edges of the gap can have very different continuum absorption features. The difference is associated with an eigenmode whose frequency can be arbitrarily close to the upper edge of the gap whereas the lower edge of the gap is always a finite distance away from the closest eigenmode.

1. Introduction

The physics of continuum absorption derives from the classical resonant absorption problem, in which a driven mechanical oscillator absorbs energy efficiently when the frequency of the driving force matches the oscillator's natural frequency. Continuum absorption is very common for electromagnetic waves in nonuniform media, where the wave frequency can locally match another natural frequency of the medium. A typical example is the magnetic beach [1]. When a low frequency magnetohydrodynamic (MHD) wave propagates along the weakening magnetic field, the local ion cyclotron frequency eventually becomes equal to the wave frequency, resulting in complete absorption of the wave due to ion cyclotron resonance. Another well-known example is the resonant absorption of laser light in a nonuniform plasma target [2].

In fusion devices, continuum absorption is one of the key damping mechanisms that determine excitation thresholds and saturation levels for Alfvén modes driven by energetic ions such as fusion-product alpha particles or fast ions generated via neutral beam injection and rf heating. The potentially unstable Alfvén waves cause undesirable losses of the fast ion population. A careful evaluation of continuum absorption is an essential element of the fast ion stability assessment. It is also essential for understanding nonlinear consequences of the fast ion driven instabilities. The absorption takes place near a magnetic surface where the driving frequency matches the local shear Alfvén frequency $\omega_A = k_\| v_A$, where v_A is the local Alfvén velocity. Figure 1 shows a typical radial profile of the shear Alfvén frequency in a tokamak; this profile represents the so-called Alfvén continuum.

The studies of Alfvénic instabilities are largely focused on discrete spectral lines within the frequency gap in the continuum [3–5]. Continuum absorption can then occur when the 'tails' of such Toroidicity-induced Alfvén Eigenmodes (TAEs) cross the continuum. In this case, the continuum spectrum near the crossing point can be approximated by a linear function, and the resulting absorption introduces a small damping rate for the mode.
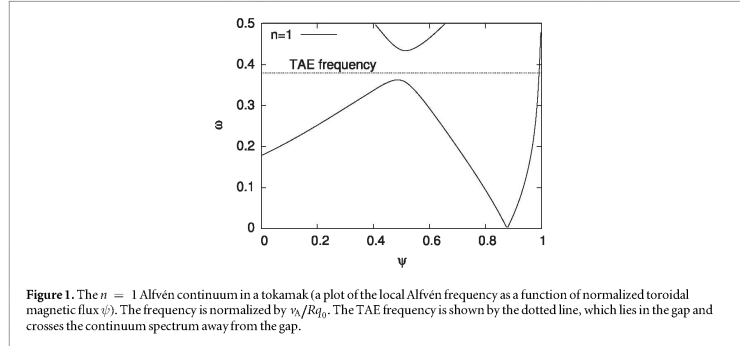
Figure 1. The $n = 1$ Alfvén continuum in a tokamak (a plot of the local Alfvén frequency as a function of normalized toroidal magnetic flux ψ). The frequency is normalized by v_A/Rq_0. The TAE frequency is shown by the dotted line, which lies in the gap and crosses the continuum spectrum away from the gap.

This damping rate can be calculated similarly to Landau damping of plasma oscillations [6], and it is known to be inversely proportional to the slope of the continuum at the crossing point.

However, the constant slope approximation breaks down at the edges of the toroidicity induced gap. The gap forms at $r = r_m$, where the local dispersion relation is satisfied for the m and $m + 1$ poloidal components simultaneously, so that $\omega = -k_{\|m+1}v_A = k_{\|m}v_A$. At the edges of the gap, the continuum is nearly flat and form two *tips*. This aspect needs special attention, because the situation is now different from the constant slope case. The need to evaluate continuum absorption at the tips becomes apparent when energetic-particle-driven modes chirp away from the TAE frequency and hit one of the tips. Recalling the constant slope picture, one might then expect a very strong continuum absorption at the tip. Yet, a more careful investigation presented herein shows that this is actually not the case.

In order to solve the tip absorption problem, we use a formalism that probes the MHD response of the plasma to an external current. The external current enters the linearized MHD equations as an oscillating source term, and we examine the response as a function of the source frequency. This source mimics the energetic particle current in the chirping event. In addition, we introduce a small dissipative term that prevents singularity in the MHD response. The dissipative term can be viewed as a friction force acting on the plasma flow. The resulting dissipative power is quite informative: it has a narrow peak inside the gap at the eigenmode frequency, and it represents continuum absorption at other frequencies provided that the friction force is sufficiently small. We have modified the ideal MHD eigenvalue code adaptive eigenfunction independent solution (AEGIS) [7] to implement this approach numerically. The adaptive grid used in AEGIS and the iterative scheme to search for the continuum crossings assures proper resolution near the tip frequency. Analytically, we choose a low shear setup and calculate the dissipative power by solving the MHD equations for shear Alfvén perturbations via asymptotic matching. Our result shows that continuum absorption vanishes at the lower tip and scales as a square root of the frequency deviation from the tip when the frequency is slightly below the tip. By comparison, the absorption near the upper tip can vary considerably due to an eigenmode that can form arbitrarily close to the upper tip depending on system parameters. These findings agree with our numerical results, and they resolve the outstanding mystery that the two tips have very different absorption features [8].

The paper is organized as follows. Section 2 introduces our basic equations and a reduced version of these equations in the limit of large aspect ratio and low magnetic shear. Section 3 presents an analytical consideration of continuum absorption within the reduced model. The numerical scheme and benchmark of the modified AEGIS code is described in section 4, followed by numerical solution of the unabridged equations. Section 5 summarizes our results.

2. Basic equations and ϵ versus s ordering

Assuming zero compressibility, we use a linearized ideal MHD equation for a cold plasma:

$$\mu_0 \rho \frac{d^2 \boldsymbol{\xi}}{dt^2} = [\boldsymbol{\nabla} \times \boldsymbol{\nabla} \times (\boldsymbol{\xi} \times \mathbf{B})] \times \mathbf{B} + (\boldsymbol{\nabla} \times \mathbf{B}) \times [\boldsymbol{\nabla} \times (\boldsymbol{\xi} \times \mathbf{B})], \tag{1}$$

where $\boldsymbol{\xi}$ is the perturbed plasma displacement, and $\mathbf{B}$ is the equilibrium magnetic field. To mimic the energetic particle drive, we introduce an external current $\delta \mathbf{J}_A$ with a tunable frequency ω. In what follows, we assume this

current to be localized on a single magnetic surface away from the toroidicity-induced gap. We also add a dissipative term $\mu_0 \rho \gamma \, d\boldsymbol{\xi}/dt$ to resolve the singularity at the continuum crossing, so that equation (1) now describes a forced oscillating system with frictional damping:

$$\mu_0 \rho \frac{d^2 \boldsymbol{\xi}}{dt^2} + \mu_0 \rho \gamma \frac{d\boldsymbol{\xi}}{dt} = [\boldsymbol{\nabla} \times \boldsymbol{\nabla} \times (\boldsymbol{\xi} \times \mathbf{B})] \times \mathbf{B} + (\boldsymbol{\nabla} \times \mathbf{B}) \times [\boldsymbol{\nabla} \times (\boldsymbol{\xi} \times \mathbf{B})]$$
$$- \left(\delta \mathbf{J}_A e^{-i\omega t} + \text{c. c} \right) \times \mathbf{B}. \tag{2}$$

We use a Fourier representation of the plasma displacement, $\boldsymbol{\xi}_\omega$, so that

$$\boldsymbol{\xi} = \frac{1}{2} \left(\boldsymbol{\xi}_\omega e^{-i\omega t} + \boldsymbol{\xi}_\omega^* e^{i\omega t} \right).$$

This gives the following expression for the time-averaged power Q dissipated in the plasma volume due to the friction force:

$$Q = \int \rho \gamma \mathbf{v} \cdot \mathbf{v} dV = \int \frac{1}{2} \rho \gamma \omega^2 \boldsymbol{\xi}_\omega^* \cdot \boldsymbol{\xi}_\omega dV. \tag{3}$$

Although the power is formally propotional to γ, it actually remains finite in the limit as $\gamma \to 0$ because $\boldsymbol{\xi}_\omega$ is large at the continuum crossing points. This allows us to choose a sufficiently small γ and scan the frequency to study the continuum absoprtion near the tip as the frequency changes.

In order to examine the absorption analytically, we consider equation (2) in the large-aspect-ratio ($\epsilon = r/R \ll 1$) and low-magnetic-shear ($s = d(\ln q)/d(\ln r) \ll 1$) limit, which is a common approximation for tokamaks. The asymptotic matching technique of TAE theory [9] will then allow us to evaluate the continuum damping rate for TAEs as well as absorption away from the eigenmode frequency.

To start with, we use the following plasma displacement representation:

$$\boldsymbol{\xi} = \xi_\parallel \mathbf{b} + \frac{1}{B^2} [\mathbf{B} \times \boldsymbol{\nabla}\Phi] + \frac{1}{B} \boldsymbol{\nabla}\Psi - \frac{1}{B} \mathbf{b}(\mathbf{b} \cdot \boldsymbol{\nabla}\Psi),$$

in which Φ represents the shear Alfvén perturbation and dominates in the shear Alfvén frequency range. The potential, Φ, can be expressed as $\Phi = \exp(-i\omega t + in\varphi)\Sigma \phi_m e^{-im\theta}$, where m and n are the poloidal and toroidal mode numbers. In the limit of large aspect ratio, low shear and high toroidal mode number, equation (2) reduces to a set of coupled equations for ϕ_m and ϕ_{m+1}, the two dominant poloidal components of Φ, near the gap location r_m [10]:

$$\frac{d}{dy}\left[\Omega\left(\Omega + i\tilde{\gamma}\right) - (y + 1/2)^2 \right]\frac{d\phi_m}{dy} - \frac{1}{s^2}\left[\Omega\left(\Omega + i\tilde{\gamma}\right) - (y + 1/2)^2 \right]\phi_m = -\eta \frac{d^2\phi_{m+1}}{dy^2}$$
$$- \frac{\epsilon - \Delta'}{s}\frac{d\phi_{m+1}}{dy} - \frac{\Delta'}{2s^2}\phi_{m+1} + \delta j_m\left(y_0 + 1/2\right)\delta\left(y - y_0\right),$$

$$\frac{d}{dy}\left[\Omega\left(\Omega + i\tilde{\gamma}\right) - (y - 1/2)^2 \right]\frac{d\phi_{m+1}}{dy} - \frac{1}{s^2}\left[\Omega\left(\Omega + i\tilde{\gamma}\right) - (y - 1/2)^2 \right]\phi_{m+1} = -\eta \frac{d^2\phi_m}{dy^2}$$
$$+ \frac{\epsilon - \Delta'}{s}\frac{d\phi_m}{dy} - \frac{\Delta'}{2s^2}\phi_m + \delta j_{m+1}\left(y_0 - 1/2\right)\delta\left(y - y_0\right). \tag{4}$$

Here $y = n[q(r) - q(r_m)]$ is the radial variable, $\Omega = \omega/\omega_0$ is the normalized frequency and $\tilde{\gamma} = \gamma/\omega_0$ is the normalized friction rate, with $\omega_0 = v_A(r_m)/q(r_m)R_0$. The quantities ϵ, Δ', and η are evaluated at r_m, and all three of them have the same order of magnitude: $\epsilon = r/R$ is the inverse aspect ratio; Δ' is the radial derivative of the Shafranov shift, and $\eta = (\epsilon + \Delta')/2$. Without loss of generality, the external current is assumed to be localized at $y = y_0$ with $y_0 > 0$, and we also assume that the external current flows along the equilibrium magnetic field, with δj_m representing the mth poloidal component of the current.

It is easy to see that $\Omega = \pm\eta + 1/2$ are the lower and upper edges of the frequency gap in the Alfvén continuum (i.e. the tip frequencies), and that both tips are located at $y = 0$. In the absence of the source terms, these wave equations describe bound states (TAEs) within the gap. We now recall [10–12] and remind some features of the TAEs that are essential for our subsequent steps. The wave equations contain two-dimensional parameters: the inverse aspect ratio ϵ and the magnetic shear s. Depending on their relative values, the gap accommodates one, two, or multiple eigenmodes. There is only one TAE mode in the gap when $\epsilon \ll s^2$. This mode is symmetric ($\phi_m \approx \phi_{m+1}$) and its frequency is slightly above the lower tip of the gap [11]. The second mode appears when ϵ becomes comparable to s^2. The frequency of this mode lies slightly below the upper tip of the gap, and the mode is antisymmetric ($\phi_m \approx -\phi_{m+1}$) [12]. For even larger values of ϵ, the gap contains multiple (more than two) modes. This happens when ϵ is comparable to or greater than s [10].

To simplify the subsequent analysis, we restrict ourselves to the case when $\epsilon \ll s$. We thereby exclude multiple modes from our consideration. However, we still intend to consider the $\epsilon \sim s^2$ range, which means

that we need to take two modes into account: the ever-present symmetric mode near the lower tip and the antisymmetric mode that may emerge near the upper tip. We note that the condition $\epsilon \ll s$ makes it allowable to neglect the first derivative terms on the righthandside (RHS) of equation (4). Following [11], we introduce the symmetric and antisymmetric combinations: $S \equiv \phi_m + \phi_{m+1}$ and $A \equiv \phi_m - \phi_{m+1}$. We also take into account that $y \ll 1$, which simplifies equation (4) to

$$\frac{\mathrm{d}}{\mathrm{d}y}[\eta(g+1) + \mathrm{i}\nu]\frac{\mathrm{d}S}{\mathrm{d}y} - \frac{1}{s^2}\Big[\eta g + \mathrm{i}\nu + \Delta'\Big]S - y\frac{\mathrm{d}S}{\mathrm{d}y}$$
$$= \frac{\mathrm{d}}{\mathrm{d}y}y\frac{\mathrm{d}A}{\mathrm{d}y} - \frac{1}{s^2}yA + \delta j_+ \delta\Big(y - y_0\Big), \tag{5a}$$

$$\frac{\mathrm{d}}{\mathrm{d}y}[\eta(g-1) + \mathrm{i}\nu]\frac{\mathrm{d}A}{\mathrm{d}y} - \frac{1}{s^2}\Big[\eta g + \mathrm{i}\nu - \Delta'\Big]A - y\frac{\mathrm{d}A}{\mathrm{d}y}$$
$$= \frac{\mathrm{d}}{\mathrm{d}y}y\frac{\mathrm{d}S}{\mathrm{d}y} - \frac{1}{s^2}yS + \delta j_- \delta\Big(y - y_0\Big), \tag{5b}$$

where $g = (4\Omega^2 - 1)/4\eta$ is the frequency parameter, $\nu \equiv \Omega\tilde{\gamma}$, $\delta j_+ \equiv y_0(\delta j_m + \delta j_{m+1}) + (\delta j_m - \delta j_{m+1})/2$, and $\delta j_- \equiv y_0(\delta j_m - \delta j_{m+1}) + (\delta j_m - \delta j_{m+1})/2$.

These equations describe two eigenmodes within the gap. The frequency parameter of the lower (nearly symmetric) mode is

$$g_1 = -1 + \frac{\pi^2 s^2}{8}\left(\frac{2\eta - 2\Delta'}{s^2} + 1\right)^2. \tag{6}$$

This mode is always present since $2\eta - 2\Delta' = \epsilon - \Delta'$ is positive. By comparison, the antisymmetric eigenmode near upper tip can only exist when $\epsilon - \Delta' > s^2$, and its frequency parameter is:

$$g_2 = 1 - \frac{\pi^2 s^2}{8}\left(\frac{2\eta - 2\Delta'}{s^2} - 1\right)^2. \tag{7}$$

These expressions for g_1 and g_2 follow from the disscussion of TAEs in [11, 12].

3. Analytical consideration

The limiting case of $\epsilon \ll s$ involves a separation of scales in the solution of equation (5). The large difference between the outer region ($|y| \sim s$) and the inner region ($|y| \sim \epsilon$) allows us to connect the outer and inner solutions via asympotic matching.

We first consider the vicinity of the lower tip ($|g + 1| \ll 1$), and only keep the dominant terms of equation (5) in the inner region (the first term on the LHS and the first term on the RHS). This simplification enables integration of equation (5) to obtain:

$$\frac{\mathrm{d}S}{\mathrm{d}y} = -\frac{R_1}{2\eta}\frac{y}{\eta(g+1) + \mathrm{i}\nu + y^2/2\eta} + \frac{R_2}{\eta(g+1) + \mathrm{i}\nu + y^2/2\eta},$$
$$\frac{\mathrm{d}A}{\mathrm{d}y} = -\frac{R_1}{2\eta}\frac{\eta(g+1) + \mathrm{i}\nu}{\eta(g+1) + \mathrm{i}\nu + y^2/2\eta} + \frac{R_2}{2\eta}\frac{y}{\eta(g+1) + \mathrm{i}\nu + y^2/2\eta}, \tag{8}$$

where R_1 and R_2 are the integration constants that remain to be expressed in terms of the external current by means of aymptotic matching. The inner solution gives the dominant contribution to total dissipative power so that one can substitute expressions (8) for $\mathrm{d}S/\mathrm{d}y$ and $\mathrm{d}A/\mathrm{d}y$ in equation (3) and then evaluate the integral using the residue theorem. The characteristic value of y in the inner region is $y \sim \eta\sqrt{|g + 1|}$, which shows that the contribution of A to Q can be neglected since $\mathrm{d}S/\mathrm{d}y \gg \mathrm{d}A/\mathrm{d}y$. We thus obtain:

$$Q \approx \int_{-\infty}^{\infty} \gamma \left|\frac{\mathrm{d}S}{\mathrm{d}y}\right|^2 \mathrm{d}y$$
$$= \int_{-\infty}^{\infty} \gamma \frac{4\eta^2 \left|R_2\right|^2 + \left|R_1\right|^2 y^2}{\left[2\eta^2(g+1) + y^2\right]^2 + 4\eta^2\nu^2}\mathrm{d}y$$
$$= \left[\frac{\pi\sqrt{2\eta}}{\sqrt{\eta^2(g+1)^2 + \nu^2}}\left|R_2\right|^2 + \frac{\pi}{\sqrt{2\eta}}\left|R_1\right|^2\right]\sqrt{\sqrt{\eta^2(g+1)^2 + \nu^2} - \eta(g+1)}. \tag{9}$$

It follows from equation (8) that S and A have jumps, ΔS and ΔA, across the inner layer. Integration of $\mathrm{d}S/\mathrm{d}y$ and $\mathrm{d}A/\mathrm{d}y$ over a wide symmetric interval covering the layer gives:

$$\Delta S = \frac{R_2}{y_1},$$

$$\Delta A = \frac{\pi R_1}{\sqrt{2\eta}} y_1,$$

where $y_1 = \sqrt{\eta(g+1) + i\nu}$ and the branch of the square root is specified by the condition that the imaginary part of y_1 is positive.

In the outer region ($|y| \sim s$), the first term on the LHS in equation (5a) scales as $[\eta(g+1)/y^2]S$, and we observe that this term is much smaller than the second term, which scales as $(\eta/s^2)S$ when $|g+1| \ll 1$. Equation (5a) can therefore be simplified to:

$$\frac{\mathrm{d}}{\mathrm{d}y} y \frac{\mathrm{d}A}{\mathrm{d}y} - \frac{1}{s^2} yA = \frac{1}{s^2}\left(\eta - \Delta'\right)S - y\frac{\mathrm{d}S}{\mathrm{d}y} + \delta j_- \delta\left(y - y_0\right). \tag{10}$$

It now follows from equation (10) that S is much greater than A, i.e. $A/S = O(\epsilon/s)$. The LHS of equation (5b) can be estimated as $(\eta/s^2)A$, and we observe that it can be dropped compared to the RHS, which roughly scales as $(y/s^2)S$. The resulting simplified equation (5b) is

$$\frac{\mathrm{d}}{\mathrm{d}y} y \frac{\mathrm{d}S}{\mathrm{d}y} - \frac{1}{s^2} yS = \delta j_+ \delta\left(y - y_0\right). \tag{11}$$

The homogenous solutions for equation (11) are the zeroth-order Macdonald's function K_0 and Bessel function I_0. Considering the inner solution for S, the coefficient in front of K_0 must be R_1 to match $\mathrm{d}S/\mathrm{d}y$ near zero to the inner solution. We also take into account that S should vanish at infinity. The resulting outer solution for S is

$$S = \begin{cases} R_1 K_0(|y|/s), & y < 0; \\ C I_0(|y|/s) + R_1 K_0(|y|/s), & 0 < y < y_0; \\ R_1 K_0(|y|/s) + C\dfrac{I_0\left(y_0/s\right)}{K_0\left(y_0/s\right)} K_0(|y|/s), & y > y_0, \end{cases}$$

where

$$C = \delta j_+ \frac{y_0}{s} K_0\left(y_0/s\right).$$

Note that S is an almost even function, except for the jump near the origin due to the source: $\Delta S = C$.

Given the solution for S, we treat the RHS of equation (10) as a source term, $\hat{L}(S)$, and use the Green's function method to find A in terms of S:

$$A = \begin{cases} I_0(|y|/s) \displaystyle\int_{+\infty}^{y} K_0(|x|/s)\hat{L}(S)\,\mathrm{d}x - K_0(|y|/s)\int_{0^+}^{y} I_0(|x|/s)\hat{L}(S)\,\mathrm{d}x - R_2 K_0(|y|/s), & y > 0; \\ I_0(|y|/s) \displaystyle\int_{-\infty}^{y} K_0(|x|/s)\hat{L}(S)\,\mathrm{d}x - K_0(|y|/s)\int_{0^-}^{y} I_0(|x|/s)\hat{L}(S)\,\mathrm{d}x - R_2 K_0(|y|/s), & y < 0. \end{cases} \tag{12}$$

The $+\infty$ and $-\infty$ integration limits in these expressions ensure that A vanishes at infinity, whereas the coefficient R_2 in front of K_0 is chosen to match $\mathrm{d}A/\mathrm{d}y$ at small values of y to the inner solution. As seen from equation (12), the jump in A across the origin is

$$\Delta A = R_1 \frac{\pi^2 s}{4}\left(\frac{2\eta - 2\Delta'}{s^2} + 1\right) + j_-,$$

where

$$j_- = C\int_0^{y_0} K_0(|x|/s)\left[\frac{1}{s^2}\left(\eta - \Delta'\right) - x\frac{\mathrm{d}}{\mathrm{d}x}\right]\left[I_0(|x|/s) - \frac{I_0\left(y_0/s\right)}{K_0\left(y_0/s\right)} K_0(|x|/s)\right]\mathrm{d}x$$

$$+ C\frac{I_0\left(y_0/s\right)}{K_0\left(y_0/s\right)} \frac{\pi^2 s}{8}\left(\frac{2\eta - 2\Delta'}{s^2} + 1\right) + \delta j_- K_0\left(y_0/s\right)$$

describes the contribution of the source.

By equating the jumps in S in the outer and inner solutions, we find

$$R_2 = y_1 C.$$

5

76

We also match the values of ΔA in the inner and outer solutions, which gives

$$R_1 = \frac{j_-}{\frac{\pi^2 s}{4}\left(\frac{2\eta - 2\Delta'}{s^2} + 1\right) - \frac{\pi}{\sqrt{2\eta}}y_1}.$$

Substitution of these expressions for R_1 and R_2 into equation (9) yields

$$Q = \left[\pi\sqrt{2\eta}\,C^2 + \frac{j_-^2}{\left|\sqrt{\eta\left(g_1 + 1\right)} - y_1\right|^2}\right]\sqrt{\sqrt{\eta^2(g+1)^2 + \nu^2} - \eta(g+1)}, \tag{13}$$

where g_1, defined by equation (6), is the frequency parameter of the lower TAE.

As seen from equation (13), the dissipative power has a sharp peak inside the gap at the TAE frequency $(g = g_1)$ with $Q \sim 1/\nu$. This feature is characteristic for a simple forced oscillator with small friction, since there is no continuum absorption in the gap.

When the frequency of the source current is somewhat below the gap, the corresponding value of g is less than -1, and the quantity y_1 is predominantly imaginary. We can then simplify equation (13) to

$$Q \approx \frac{\sqrt{|\eta(g+1)|}}{\eta\left(g_1 + 1\right) + |\eta(g+1)|}j_-^2 + \sqrt{|\eta(g+1)|}\,C^2. \tag{14}$$

As we scan the source frequency downward from the tip, the quantities j_- and C remain nearly constant (they do not change significantly in the vicinity of the tip). For the first term in equation (14), the denominator contains a constant contribution and the $|\eta(g+1)|$ term. The constant part is finite at the lower tip, which shows that the total dissipative power Q scales as $\sqrt{|\eta(g+1)|}$ downward from the lower tip. We can roughly estimate the range of g values for the $\sqrt{|\eta(g+1)|}$ scaling as:

$$|\eta(g+1)| < \eta\left(g_1 + 1\right),$$

$$g > g_L = -1 - \frac{\pi^2 s^2}{8}\left(\frac{2\eta - 2\Delta'}{s^2} + 1\right)^2,$$

and we observe that this range is of the same order as the distance from the lower TAE to the tip.

The technique of solving equation (5) for the frequencies near the upper tip is very similar to the lower tip case, but the solution near the upper tip is now dominated by the antisymmetric combination A. The resulting dissipative power near the upper tip is given by

$$Q = \left[\pi\sqrt{2\eta}\,C'^2 + \frac{j_+^2}{\left|\frac{\pi\sqrt{2\eta}s}{4}\left(\frac{2\eta - 2\Delta'}{s^2} - 1\right) - y_2\right|^2}\right]\sqrt{\sqrt{\eta^2(g-1)^2 + \nu^2} + \eta(g-1)}, \tag{15}$$

where

$$C' = \delta j_- \frac{y_0}{s}K_0\left(y_0/s\right);$$

$$j_+ = C'\int_0^{y_0} K_0(|x|/s)\left[\frac{1}{s^2}\left(\eta - \Delta'\right) + x\frac{\mathrm{d}}{\mathrm{d}x}\right]\left[I_0(|x|/s) - \frac{I_0\left(y_0/s\right)}{K_0\left(y_0/s\right)}K_0(|x|/s)\right]\mathrm{d}x$$

$$+ C'\frac{I_0\left(y_0/s\right)}{K_0\left(y_0/s\right)}\frac{\pi^2 s}{8}\left[\frac{2\eta - 2\Delta'}{s^2} - 1\right] + \delta j_+ K_0\left(y_0/s\right)$$

and $y_2 = \sqrt{-\eta(g-1) + \mathrm{i}\nu}$ is chosen in such a way that $\mathrm{Im}(y_2) > 0$. This dissipative power exhibits a peak at $g = g_2$, provided that there is an upper TAE mode in the gap. The absorption otherwise vanishes below the upper tip in the limit of $\nu \to 0$.

Above the upper tip $(g > 1)$, equation (15) simplifies to

$$Q \approx \frac{\sqrt{\eta(g-1)}}{\frac{\pi^2\eta s^2}{8}\left(\frac{2\eta - 2\Delta'}{s^2} - 1\right)^2 + \eta(g-1)}j_+^2 + \sqrt{\eta(g-1)}\,C'^2. \tag{16}$$

Figure 2. Function $y = \sqrt{x}/(x + c)$ for different values of c, where x represents $|\eta(g-1)|$ and c stands for $\dfrac{\pi^2\,s^2}{8}\left(\dfrac{2\eta - 2\Delta'}{s^2} - 1\right)^2$ in equation (16).
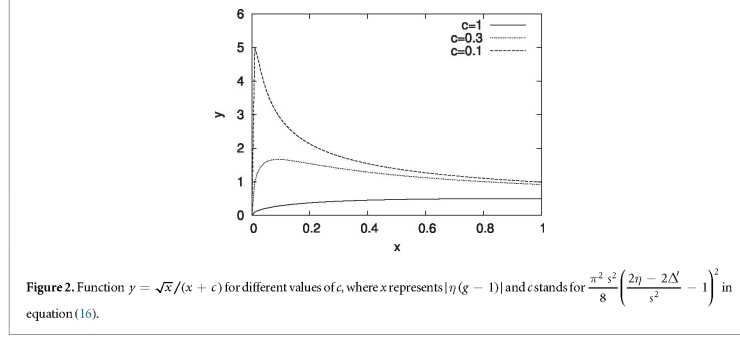
As we scan the source frequency upward from the upper tip, the range for the $\sqrt{|\eta(g-1)|}$ scaling of Q is

$$g < g_{\rm U} = 1 + \frac{\pi^2\,s^2}{8}\left(\frac{2\eta - 2\Delta'}{s^2} - 1\right)^2,$$

which is of the same order as the frequency difference between the upper TAE and the tip. In contrast with the lower tip case, the threshold frequency can be very close to the tip because $(2\eta - 2\Delta')/s^2 - 1$ may change sign and become very small as parameter changes. In the limiting case when $(2\eta - 2\Delta')/s^2 = 1$, the first term in equation (16) scales as $1/\sqrt{|\eta(g-1)|}$, and results in a large divergent part $1/\sqrt{|\eta(g-1)|}$ in the total dissipative power. Figure 2 shows the behavior of the first term in equation (16) versus frequency for various parameters, which demonstrates that the absorption can be large at the tip, and is sensitive to the parameters when $(2\eta - 2\Delta')/s^2 \sim 1$.

We can now summarize the different scenarios for continuum absorption near the two tips in the $\epsilon \ll s$ limit. Near the lower tip, where there is an ever-present neighboring eigenmode that never touches the tip, the absorption always vanishes at the tip. When ϵ increases, the separation between the eigenfrequency and the lower tip will increase as well as the range for the $\sqrt{|\eta(g+1)|}$ scaling of Q below the lower tip. For the upper tip, where there is no neighboring eigenmode until ϵ becomes comparable to s^2, the range of the $\sqrt{|\eta(g-1)|}$ scaling shrinks when ϵ approaches the mode-existence threshold; consequently, the $\sqrt{|\eta(g-1)|}$ scaling breaks down and we may expect a large continuum absorption at the tip when the upper eigenmode is just about to appear. As we further increase ϵ, the range of the $\sqrt{|\eta(g-1)|}$ scaling of Q grows in step with the distance between the eigenmode frequency and the tip. These features are responsible for significant asymmetry in continuum absorption at the tips.

4. Numerical results

4.1. Numerical scheme and benchmark

We use the AEGIS code to study continuum absorption numerically. AEGIS is a linear MHD eigenvalue code with an adaptive mesh in the radial direction (here toroidal magnetic flux ψ is used as the radial coordinate), and Fourier decomposition in the poloidal (θ) and toroidal (ζ) directions. The plasma displacement vector ($\boldsymbol{\xi}$), which is orthogonal to the equilibrium magnetic field under incompressibility condition, is represented by two functions (ξ_s and ξ_ψ) as

$$\boldsymbol{\xi} \times \mathbf{B} = \xi_s \boldsymbol{\nabla}\psi + \xi_\psi \chi'(\boldsymbol{\nabla}\zeta - q\boldsymbol{\nabla}\theta),$$

where $2\pi\chi$ is the poloidal magnetic flux. The perturbed quantities are Fourier transformed as:

$$\xi_\psi e^{-in\zeta} = \sum_{m=-\infty}^{\infty} \xi_{\psi m}\frac{1}{\sqrt{2\pi}}e^{i(m\theta - n\zeta)}.$$

We then use equation (2) to introduce the external current $\delta \mathbf{J}_{\rm A}$ with frequency ω in AEGIS. Assuming the current to flow on a single magnetic surface ψ_0 and being divergence free ($\boldsymbol{\nabla} \cdot \delta\mathbf{J}_{\rm A} = 0$), we express ξ_s in terms of ξ_ψ and obtain the following set of equations for $\xi_{\psi m}$:
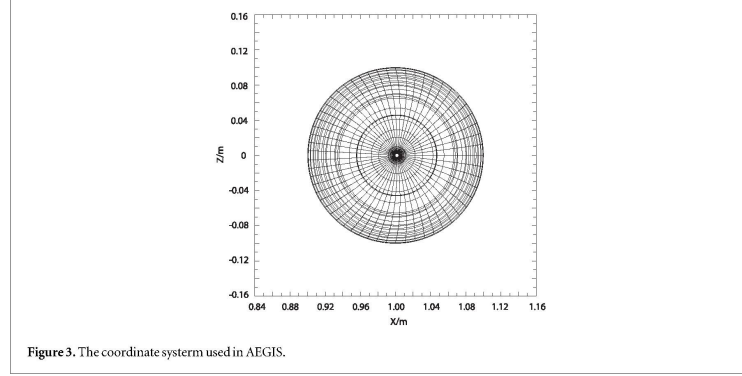
Figure 3. The coordinate systerm used in AEGIS.

$$\left(F\xi'_{\psi m} + K\xi_{\psi m}\right)' - (K^{\dagger}\xi'_{\psi m} + G\xi_{\psi m} + nS_m\delta\left(\psi - \psi_0\right) = 0, \tag{17}$$

where

$$S_m = \chi'(m - nq)\delta j_m$$

represents the external current. The definitions of matrices F, K, and G are given in [7]. We add a small positive imaginary part $(i\gamma/2)$ to the frequency ω in the expressions for F, K, and G, to capture the effect of friction. To solve for $\xi_{\psi m}$ in equation (17), AEGIS divides the radial computational domain into multiple regions, and matches the independent solutions at the interfaces of these regions. Consequently, ψ_0 can be set as one of the interfaces between the adjacent regions in AEGIS so that the source contribution will only affect the matching condition across ψ_0. The adaptive mesh in AEGIS allows us to input the resonance point and pack the nearby grid points exponentially, which ensures proper resolution near the continuum crossing for small values of γ.

With the modified code, we first study the continuum absorption of the $n = 1$ TAE as a test case. Since the continuum crossing is away from the gap in this case, toroidicity-induced coupling can be neglected near the crossing, which means that the matrices F, K, and G are almost diagonal there. Suppose mth equation in (17) has singularity ($F_{mm} \approx 0$) near the crossing. We can then keep the highest derivative term of $\xi_{\psi m}$ and simplify the equation to

$$F_{mn}\xi'_{\psi m} = C_1,$$

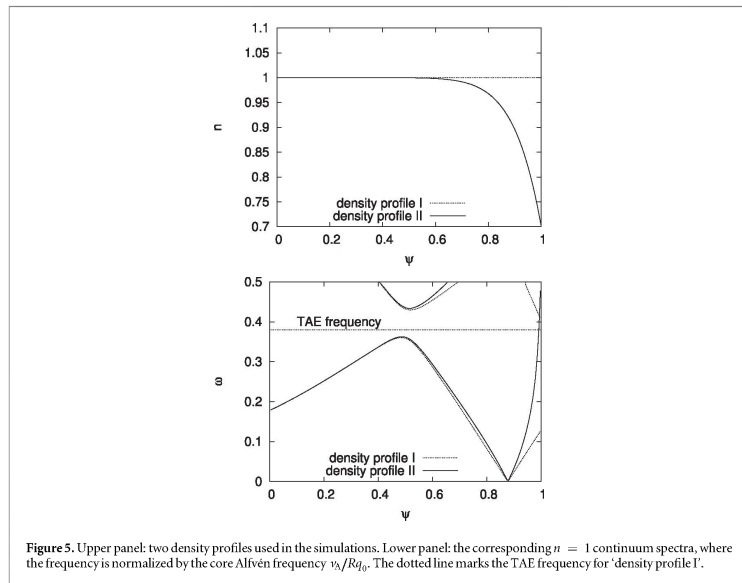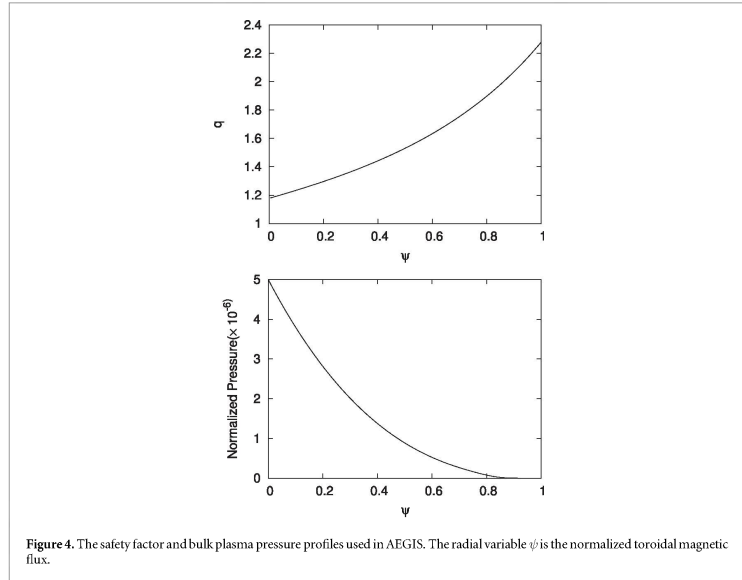where C_1 is an integration constant. By linear expansion of F_{mm} at the crossing ψ_0, we find

$$\xi'_{\psi m} = \frac{C_1}{F'_{mm}\left(\psi - \psi_0\right) + i\gamma^*}. \tag{18}$$

Here γ^* is the imaginary part of F_{mm}, which is propotional to γ. The total dissipative power is

$$Q = \int \frac{1}{2}\rho\gamma\omega^2\xi^* \cdot \xi J d\psi d\zeta d\theta \sim \int \pi\rho\gamma\omega^2 \frac{C_1^2}{F'^2_{mm}\left(\psi - \psi_0\right)^2 + \gamma^{*2}} d\psi \sim C_1^2\left(\frac{dF_{mm}}{d\psi}\right)^{-1},$$

which shows that Q is inversely propotional to the slope of the continuum spectrum near the crossing when γ is sufficiently small.

We choose a low beta tokamak equilibrium that has nearly circular cross section (see figure 3), with the equilibrium pressure and safety factor plotted in figure 4. By slightly varying the density profile near the plasma edge, the gap can be either open or closed without changing the TAE frequency significantly. Figure 5 shows two density profiles we used ('density profile I' and 'density profile II') and the corresponding continuum spectra. For 'density profile I', the gap is open and we find the $n = 1$ TAE (whose frequency is labeled in figure 5). On the other hand, 'density profile II' closes the gap and introduces continuum absorption at the edge for the TAE. We scan the source frequency for 'density profile II' for different values of γ and plot the total dissipative power in figure 6. This figure shows that the dissipative power has a peak near the eigenfrequency, and it converges for small values of γ away from the eigenfrequency, as we expect analytically.

Figure 4. The safety factor and bulk plasma pressure profiles used in AEGIS. The radial variable ψ is the normalized toroidal magnetic flux.

Figure 5. Upper panel: two density profiles used in the simulations. Lower panel: the corresponding $n = 1$ continuum spectra, where the frequency is normalized by the core Alfvén frequency v_A/Rq_0. The dotted line marks the TAE frequency for 'density profile I'.
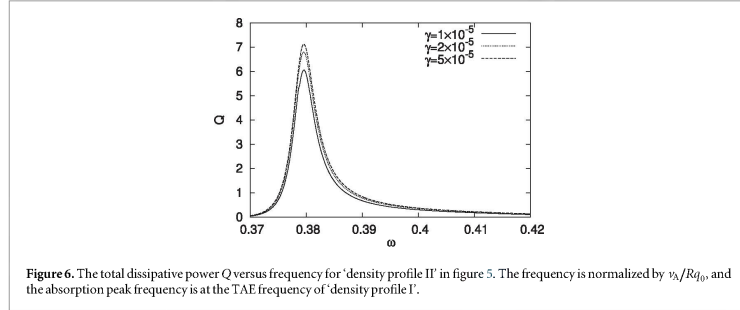
9

Figure 6. The total dissipative power Q versus frequency for 'density profile II' in figure 5. The frequency is normalized by v_A/Rq_0, and the absorption peak frequency is at the TAE frequency of 'density profile I'.
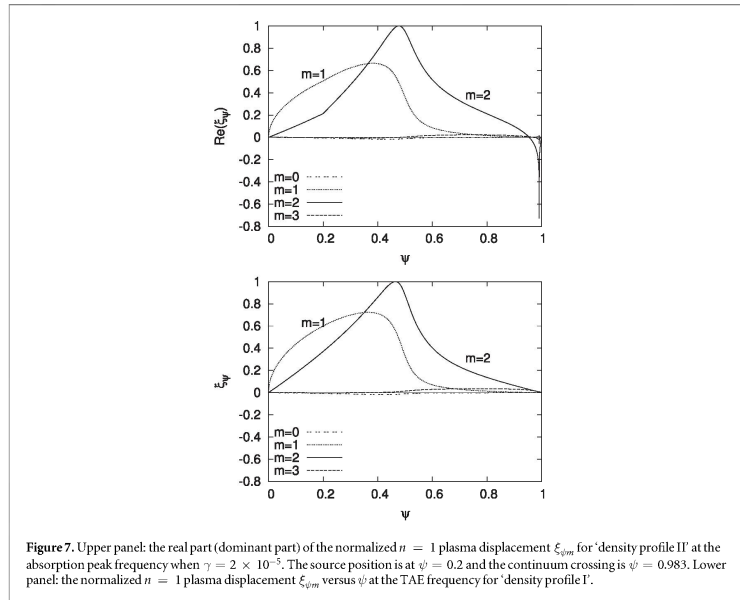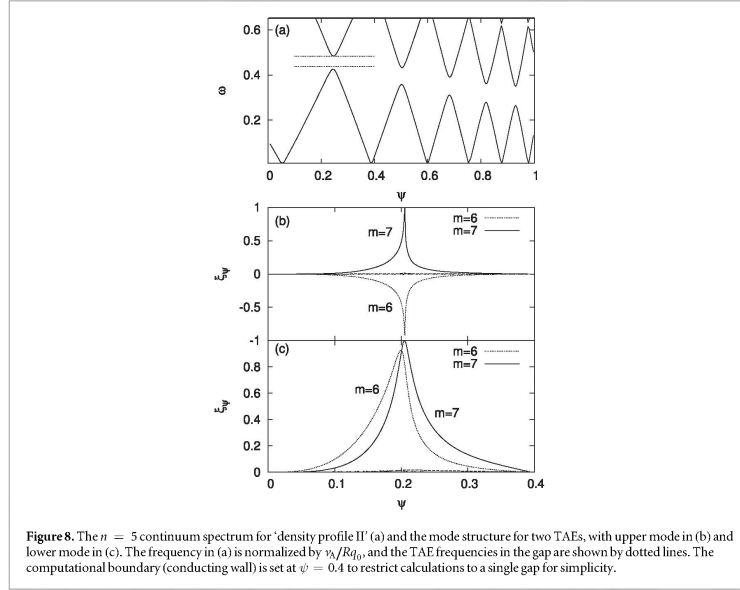

Figure 7. Upper panel: the real part (dominant part) of the normalized $n = 1$ plasma displacement $\xi_{\psi m}$ for 'density profile II' at the absorption peak frequency when $\gamma = 2 \times 10^{-5}$. The source position is at $\psi = 0.2$ and the continuum crossing is $\psi = 0.983$. Lower panel: the normalized $n = 1$ plasma displacement $\xi_{\psi m}$ versus ψ at the TAE frequency for 'density profile I'.

To check how well the mode structure is resolved at the continuum crossing, we plot the plasma response when dissipative power has a peak and compare it to the TAE structure when the gap is open in figure 7. We see that the plasma displacement in the two cases agrees quite well away from the continuum crossing. In addition, we compare the calculated plasma response near the continuum crossing with the analytical solution, which is obtained after integration of equation (18):

$$\frac{\xi_{\psi m}\,|_{\psi_0-\Delta}^{\psi_0+\Delta}}{F_{mm}\xi'_{\psi m}} = 2\left(\frac{\mathrm{d}F_{mm}}{\mathrm{d}\psi}\right)^{-1}\tan^{-1}\left(\frac{\Delta}{\gamma^*}\right).$$

The code output is found to be in close agreement with this expression.

Near the eigenfrequency, the bulk plasma response is large and it can still contribute considerably to the total dissipative power even when γ is relatively small. As a result, the total dissipative power is greater than the continuum absorption at the crossing. To single out the continuum absorption at eigenfrequency, we define the

10

Figure 8. The $n = 5$ continuum spectrum for 'density profile II' (a) and the mode structure for two TAEs, with upper mode in (b) and lower mode in (c). The frequency in (a) is normalized by v_A/Rq_0, and the TAE frequencies in the gap are shown by dotted lines. The computational boundary (conducting wall) is set at $\psi = 0.4$ to restrict calculations to a single gap for simplicity.

continuum damping rate as

$$\gamma_{\mathrm{d}} = \frac{Q}{2E_{\mathrm{tot}}} = \frac{\int_{\psi_0 - \delta}^{\psi_0 + \delta} \rho \gamma \omega^2 \boldsymbol{\xi}^* \cdot \boldsymbol{\xi} \mathrm{d}V}{4 \int \rho \omega^2 \boldsymbol{\xi}^* \cdot \boldsymbol{\xi} \mathrm{d}V - 4 \int_{\psi_0 - \delta}^{\psi_0 + \delta} \rho \omega^2 \boldsymbol{\xi}^* \cdot \boldsymbol{\xi} \mathrm{d}V}.$$
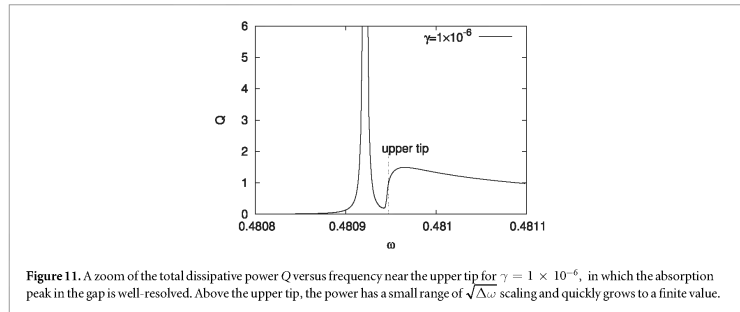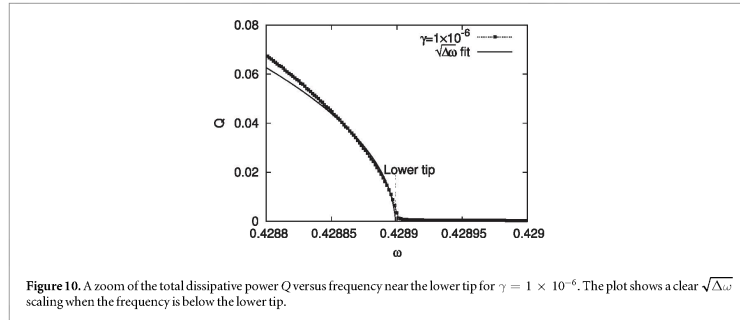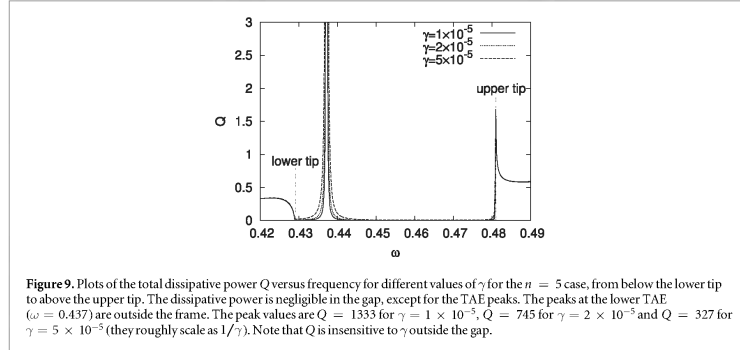
Here we use the fact that the total energy of the mode, E_{tot}, is contributed equally from the bulk plasma kinetic energy and potential energy, and we choose $\delta \gg \gamma^*$ to determine the integration limits. For small values of γ, the bulk plasma energy is well-separated from the continuum crossing and γ_{d}. We calculate the continuum damping rate for different values of γ for the $n = 1$ TAE. The continuum damping rate converges as γ decreases, and its value agrees with the result obtained via analytic continuation in [13].

4.2. Tip absorption results

In the studies of continuum absorption at the tips, there are two closely spaced crossings that are equally important. To resolve the field structure at the two crossings, γ must be very small and the points for grid setting need to be chosen carefully. To meet the numerical requirement, we search for the continuum crossings iteratively. Previous studies of tip absorption in a reversed-shear configuration [8] provide a good guidance for our simulation since the numerical requirements are similar despite the differences in the physics picture.
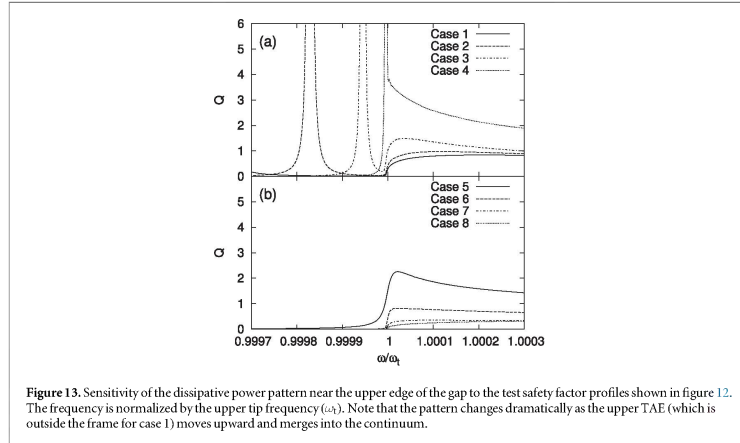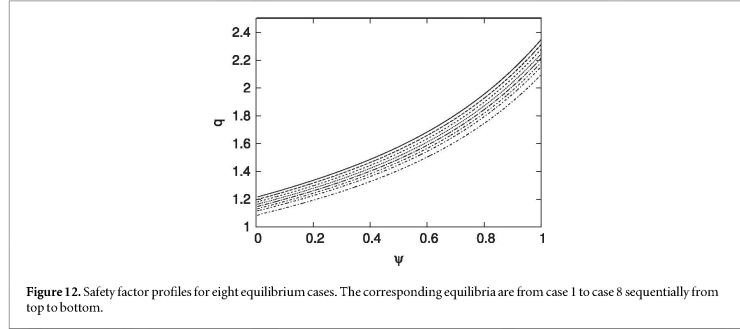
For better comparison with the analytical result, we study the $n = 5$ case using the same tokamak equilibrium (with 'density profile II') as in section 4.2. Figure 8 is the corresponding $n = 5$ continuum spectrum. We set the boundary at $\psi = 0.4$ to focus on the tip absorption in the first gap. In this way the gap is open and TAEs appear both near the upper and the lower tip (labeled in figure 8). The two TAEs are strongly asymmetric (the upper TAE is much closer to the upper tip than the lower TAE to the lower tip).

We scan the source frequency from below the lower tip to the upper tip and plot the total dissipative power in figure 9. Inside the gap, the continuum absorption is almost zero except for the peaks at the TAE eigenfrequencies. Outside the gap, the dissipative power shows good convergence for different values of γ, and we observe a significant difference between the upper and lower tips. Figure 10 is a zoom-in of the dissipative power near the lower tip. It shows that the absorption almost vanishes at the tip and follows the $\sqrt{\Delta\omega}$ scaling below the lower tip, where $\Delta\omega$ measures the frequency difference from the lower tip and is proportional to the

Figure 9. Plots of the total dissipative power Q versus frequency for different values of γ for the n = 5 case, from below the lower tip to above the upper tip. The dissipative power is negligible in the gap, except for the TAE peaks. The peaks at the lower TAE (ω = 0.437) are outside the frame. The peak values are Q = 1333 for γ = 1 × 10⁻⁵, Q = 745 for γ = 2 × 10⁻⁵ and Q = 327 for γ = 5 × 10⁻⁵ (they roughly scale as 1/γ). Note that Q is insensitive to γ outside the gap.

Figure 10. A zoom of the total dissipative power Q versus frequency near the lower tip for γ = 1 × 10⁻⁶. The plot shows a clear $\sqrt{\Delta\omega}$ scaling when the frequency is below the lower tip.

Figure 11. A zoom of the total dissipative power Q versus frequency near the upper tip for γ = 1 × 10⁻⁶, in which the absorption peak in the gap is well-resolved. Above the upper tip, the power has a small range of $\sqrt{\Delta\omega}$ scaling and quickly grows to a finite value.

$|\eta(g+1)|$ in section 3. Similar zoom-in of the upper tip absorption is presented in figure 11, in which there is a well-resolved absorption peak at the upper TAE frequency. The continuum absorption in this figure has only a very narrow range of validity for the $\sqrt{\Delta\omega}$ scaling (in this case $\Delta\omega$ is the frequency difference from the upper tip and is propotional to the $|\eta(g-1)|$), and this range is comparable to the frequency separation of the TAE from the tip.

To study the tip absorption as system parameters change, we investigate a set of eight equilibrium cases, which are generated by varying the strength of the equilibrium current. All these equilibrium cases have

Figure 12. Safety factor profiles for eight equilibrium cases. The corresponding equilibria are from case 1 to case 8 sequentially from top to bottom.

Figure 13. Sensitivity of the dissipative power pattern near the upper edge of the gap to the test safety factor profiles shown in figure 12. The frequency is normalized by the upper tip frequency (ω_t). Note that the pattern changes dramatically as the upper TAE (which is outside the frame for case 1) moves upward and merges into the continuum.

negligible pressure and similar safety factor profile. Yet, the safety factor value decreases monotonically from case 1 to case 8, which can be seen from figure 12. Thus, as one moves from case 1 to case 8, the position of the gap moves outwards and the ratio ϵ/s^2 will also decrease monotonically.

With these equilibria, we observe the expected sensitivity of the upper tip absorption to variation of the aspect ratio and magnetic shear. From case 1 to case 8, the frequency interval between the lower TAE and the lower tip doesn't change significantly. Consequently, the lower tip absorption turns out to be nearly the same. Yet, the upper TAE and the upper tip absorption are much more sensitive. Figure 13 shows the absorption near the upper tip as equilibrium changes. It is apparent that the TAE frequency moves closer to the upper tip and the range of the $\sqrt{\Delta\omega}$ scaling narrows from case 1 to case 4. As the q profile decreases from case 5 to case 8, the TAE disappears and the range of the $\sqrt{\Delta\omega}$ scaling grows. This feature of the upper tip absorption agrees with the analytical expectation presented in figure 2, and it also appears in our simulations for the $n = 1$ case.

5. Summary and discussion

To summarize, we have examined the continuum absorption around the edges of the toroidicity-induced gap in the Alfvén continuum spectrum. To solve the problem, we introduce a driving current and a small dissipative term to the ideal MHD equations.

For an analytical assessment, we reduce the basic MHD equations to a two-poloidal-mode set. Based on earlier work, we show how the inverse aspect ratio ϵ and magnetic shear s cause an asymmetry of the lower and upper TAE frequencies within the gap. Compared to the lower TAE, the existence of the upper TAE is strongly sensitive to ϵ and s. This high sensitivity offers an interesting possibility of measuring the relationship between ϵ and s through the presence of the upper TAE.

Using the simplified equation, we show that the continuum absorption always vanishes at the lower tip, and scales as the square root of the downward frequency shift ($\sqrt{\Delta\omega}$) from the lower tip. On the other hand, the continuum absorption above the upper tip usually has a smaller range of $\sqrt{\Delta\omega}$ scaling, and may not vanish at the tip when the neighbouring TAE frequency in the gap is very close to the tip frequency.

We have modified the AEGIS code to study the continuum absorption numerically. With a nearly circular tokamak equilibrium, we vary ϵ and s by changing the safety factor profile. The resulting lower tip absorption does not change dramatically, whereas the upper tip absorption can vary significantly when the q profile changes, which is consistent with our analytical calculation.

These absorption patterns result from an interference of the two poloidal harmonics of the perturbation, a feature that is absent when the tip of the continuum is due to shear reversal (see [8]). The reversed shear tip is formed where $q' = 0$ with finite q'', and the continuum absorption is very large at the tip, scaling as $1/\sqrt{\Delta\omega}$ as frequency approaches the tip within the continuum.

It should be noted that we draw our conclusion from the simplified shear Alfvén equations, which assume high n, $\epsilon < s$, and low pressure. The pressure gradient tends to shift the TAE frequencies towards the continuum (see [12, 14]), and should affect dissipation at both tips. However, the asymmetry between the lower and upper eigenmodes should still be present in this case, as well as the resulting differences between the upper and lower tip absorption patterns.

Acknowledgments

References

[1] Stix T H 1992 *Waves in Plasmas* (New York: American Institute of Physics)
[2] Ginzburg V L 1964 *The Propagation of Electromagnetic Waves in Plasmas* (Oxford: Pergamon)
[3] Rosenbluth M N, Berk H L, Van Dam J W and Lindberg D M 1992 *Phys. Rev. Lett.* **68** 596
[4] Berk H L, Dam J W V, Guo Z and Lindberg D M 1992 *Phys. Fluids* B **4** 1806
[5] Chu M S, Greene J M, Ling W, Turnbull A D, Berk H L and Rosenbluth M N 1994 *Phys. Plasmas* **1** 1214
[6] Landau L 1946 *JETP* **16** 574
[7] Zheng L J and Kotschenreuther M 2006 *J. Comput. Phys.* **211** 748
[8] Chen E, Berk H, Breizman B and Zheng L J 2011 *Bull. Am. Phys. Soc.* **56** 284
[9] Cheng C Z, Chen L and Chance M S 1985 *Ann. Phys., NY* **161** 21
[10] Candy J, Breizman B N, Van Dam J W and Ozeki T 1995 *Phys. Lett.* A **215** 299
[11] Breizman B N and Sharapov S E 1995 *Plasma Phys. Control. Fusion* **37** 1057
[12] Berk H L, Van Dam J W, Borba D, Candy J, Huysmans G T A and Sharapov S 1995 *Phys. Plasmas* **2** 3401
[13] Zheng L J, Kotschenreuther M T and Valanju P 2013 *Phys. Plasmas* **20** 012501
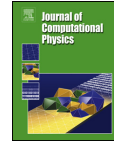[14] Zonca F and Chen L 1993 *Phys. Fluids* B **5** 3668

paper C Canonical Straight field line magnetic flux coordinates for tokamaks

Short note

Canonical straight field line magnetic flux coordinates for tokamaks

CrossMark

Meng Li *, Boris N. Breizman, Linjin Zheng

Institute for Fusion Studies, University of Texas at Austin, Austin, TX 78712, United States

A B S T R A C T

New global straight field line coordinates are introduced for a toroidal plasma configuration. The new coordinate system provides a canonical description of particle guiding center motion while maintaining the straight field line feature. These coordinates are convenient for combining MHD calculations with kinetic modeling of energetic particles. We demonstrate how the new coordinate system can be constructed by transforming the poloidal and toroidal angles. Numerical examples show comparison of the new coordinates with various non-canonical coordinates for the same equilibrium configuration.

© 2016 The Authors. Published by Elsevier Inc. This is an open access article under the CC BY-NC-ND license (http://creativecommons.org/licenses/by-nc-nd/4.0/).

1. Introduction

Tokamaks are designed to have closed, nested magnetic surfaces on which plasma pressure is constant as required by the force balance. The Grad–Shafranov equation determines configuration of these surfaces for the tokamak equilibrium [1]. Due to strong anisotropy associated with the magnetic field, the magnetic surface label ψ is a convenient radial coordinate for computations. The corresponding commonly used magnetic flux coordinates (ψ, θ, ζ) are the magnetic flux, the generalized poloidal and toroidal angles. In most cases, the generalized angles (θ, ζ) do not have to be the geometric poloidal and toroidal angles (θ_g, ϕ). For convenience, the generalized angles are often chosen so that the magnetic field lines are straight when plotted on (θ, ζ) plane, i.e.:

$$\mathbf{B} = \chi'(\nabla \zeta \times \nabla \psi + q(\psi)\nabla \psi \times \nabla \theta),$$

where $q(\psi)$ is the safety factor, $\chi(\psi)$ is the poloidal magnetic flux with prime denoting the derivative with respect to ψ, and $\mathbf{B} \cdot \nabla \psi = 0$. These coordinates are the so-called straight field line coordinates and they are particularly convenient for stability analysis. The coordinate system in which the field lines are straight is not unique. The commonly used versions of the straight field line coordinates are PEST [2], Hamada [3], equal arclength, and Boozer [4] coordinates.

It should, however, be noted that these four versions are not optimal for Hamiltonian description of the particle guiding center motion in tokamaks. A Hamiltonian description of the guiding center equations of motion is essential for investigating particle trajectories on very long times since it satisfies the Liouville theorem. The guiding center motion is known to be governed by the Littlejohn Lagrangian [5]:

$$L(\mathbf{X}, \mu, v_\parallel, \xi) = \frac{e}{c}\mathbf{A} \cdot \dot{\mathbf{X}} + m v_\parallel \frac{(\mathbf{B} \cdot \dot{\mathbf{X}})}{B} + \frac{mc}{e}\mu\dot{\xi} - \mu B - \frac{1}{2}m v_\parallel^2 - e\Phi. \tag{1}$$

---

* Corresponding author.
  E-mail address: mengli@utexas.edu (M. Li).

87

The dynamical variables in this Lagrangian are: **X** (the guiding center position), $\mu = mv_\perp^2/2B$ (the magnetic moment), ξ (the gyroangle), and $v_\parallel$ (the parallel velocity). The magnetic field **B**, the vector potential **A**, and the scalar potential Φ are evaluated at the guiding center position. The guiding center phase space is six-dimensional, but the six dynamical variables in the Lagrangian do not immediately split into three canonical pairs for Hamiltonian formalism. The reason is that the Littlejohn Lagrangian generally contains time derivatives of four variables rather than three. These four are the components of **X** and the gyroangle.

There have been several attempts in the past to eliminate the extra time derivative and find a set of canonical variables (two coordinates and two momenta besides μ and ξ). One of the attempts is based on Boozer coordinates [4], in which the Jacobian is $J = ((\nabla \psi \times \nabla \theta) \cdot \nabla \zeta)^{-1} = 1/B^2$. The contravariant radial component of **B** is zero in these coordinates. However, the covariant component B_ψ associated with the nonorthogonality of the coordinates does not generally vanish. The neglect of nonzero B_ψ modifies the Lagrangian and thus the equations of motion, which is undesirable. Later, in Ref. [6], a simple change of the guiding center velocity is introduced to achieve a canonical form with a claim that the orbit in the poloidal plane and the toroidal precession remains unchanged. Yet that procedure is not equivalent to coordinate transformation and does not preserve the Littlejohn Lagrangian either, which can distort the time-dependence of the original gyrocenter motion in long-term simulations.

Reference [7] offers a rigorous alternative. By redefining the poloidal angle, it introduces a new coordinate system in which both the vector potential **A** and magnetic field **B** only have two nonzero covariant components; this procedure eliminates the $\dot{\psi}$ term from the Lagrangian. Although Ref. [7] gives the poloidal angle transformation analytically for Shafranov equilibrium, it is impractical to find such a coordinate system globally in numerical simulations when the flux surfaces are not circular. The transformation introduced in Ref. [7] gives orthogonal coordinates with one of the coordinate axes being orthogonal to **A** and **B** locally. It is unfortunate that nonuniformity of this coordinate system is significant in many equilibrium configurations of interest, such as elliptically shaped equilibria. Also, the magnetic field lines are not automatically straight in the orthogonal coordinates. For these reasons, numerical implementation of the orthogonal coordinates is challenging for realistic tokamaks.

To eliminate this difficulty, we herein construct a new type of global coordinates by modifying the poloidal and toroidal angles simultaneously, so that

$$\mathbf{A} = A_\theta(\psi)\nabla\theta + A_\zeta(\psi)\nabla\zeta,$$

$$\mathbf{B} = B_\theta\nabla\theta + B_\zeta\nabla\zeta.$$

It then follows from Eq. (1) that the guiding center Lagrangian can be written as a function of the canonical variables $(\theta, \zeta, P_\theta, P_\zeta)$:

$$L = P_\theta\dot{\theta} + P_\zeta\dot{\zeta} + \frac{mc}{e}\mu\dot{\xi} - H, \tag{2}$$

where the Hamiltonian is defined as

$$H = \mu B + \frac{1}{2}mv_\parallel^2 + e\Phi,$$

with

$$P_\theta = \frac{eA_\theta}{c} + mv_\parallel\frac{B_\theta}{B},$$

$$P_\zeta = \frac{eA_\zeta}{c} + mv_\parallel\frac{B_\zeta}{B},$$

and two of the three coordinates (poloidal and toroidal angles) automatically become canonical variables. These coordinates provide a rigorous Hamiltonian form as in Ref. [7], and they are also suitable globally unlike the orthogonal coordinates. Moreover, the new coordinates preserve the straight magnetic field line feature, which makes them perfectly compatible with existing codes. In what follows, we call them "canonical straight field line coordinates". In Sec. 2 of this paper, we discuss how to construct such coordinates. Section 3 shows their numerical implementation for realistic tokamaks. Section 4 is a brief summary.

2. Construction of the canonical straight field line coordinates

In the general straight field line coordinates (ψ, θ, ζ), the magnetic field **B** has the following contravariant representation:

$$\mathbf{B} = \chi'(\nabla\zeta \times \nabla\psi + q\nabla\psi \times \nabla\theta),$$

and the corresponding covariant representation for the vector potential **A** is:

$$\mathbf{A} = \left(\int q\chi'\mathrm{d}\psi\right)\nabla\theta - \chi\nabla\zeta.$$

88

To construct the new coordinates, we use the same magnetic flux variable ψ and modify the poloidal and toroidal angles. In order to preserve periodicity in the poloidal and toroidal directions, we seek the new generalized poloidal and toroidal angles (θ_c, ζ_c) of the form:

$$\theta_c = \theta + \nu(\psi, \theta), \zeta_c = \zeta + \nu_1(\psi, \theta), \tag{3}$$

where ν and ν_1 are periodic functions of θ. We choose

$$\nu_1 = q\nu, \tag{4}$$

to ensure that the new coordinates maintain straight field lines:

$$\mathbf{B} = \chi'(\nabla\zeta_c \times \nabla\psi + q\nabla\psi \times \nabla\theta_c), \tag{5}$$

and the expression for $\mathbf{A}$ remains the same:

$$\mathbf{A} = \left(\int q\chi'\mathrm{d}\psi\right)\nabla\theta_c - \chi\nabla\zeta_c.$$

Then the only constraint on the canonical coordinates is that the covariant radial component of $\mathbf{B}$ is zero, i.e.

$$B_\psi = \mathbf{B} \cdot \vec{e}_\psi = 0, \tag{6}$$

where

$$\vec{e}_\psi = J(\nabla\theta_c \times \nabla\zeta_c).$$

Taken together, Eqs. (3)–(6) give a partial differential equation for ν:

$$\frac{\partial\nu}{\partial\psi} = C_1\frac{\partial\nu}{\partial\theta} + C_2\nu\frac{\partial\nu}{\partial\theta} + C_2\nu + C_1, \tag{7}$$

where

$$C_1 = \frac{G_{12} + qG_{31}}{G_{22} + 2qG_{23} + q^2G_{33}},$$

$$C_2 = -\frac{q'G_{22} + qq'G_{23}}{G_{22} + 2qG_{23} + q^2G_{33}},$$

with

$$G_{22} = J(\nabla\zeta \times \nabla\psi) \cdot (\nabla\zeta \times \nabla\psi),$$

$$G_{33} = J(\nabla\psi \times \nabla\theta) \cdot (\nabla\psi \times \nabla\theta),$$

$$G_{12} = J(\nabla\theta \times \nabla\zeta) \cdot (\nabla\zeta \times \nabla\psi),$$

$$G_{31} = J(\nabla\psi \times \nabla\theta) \cdot (\nabla\theta \times \nabla\zeta),$$

$$G_{23} = J(\nabla\zeta \times \nabla\psi) \cdot (\nabla\psi \times \nabla\theta).$$

The matrix elements G_{ik} as well as the functions C_1 and C_2 are herein evaluated in the original straight field line coordinates. After solving for ν, we obtain a canonical straight field line coordinate system in which:

$$\mathbf{A} = A_{\theta_c}(\psi)\nabla\theta_c + A_{\zeta_c}(\psi)\nabla\zeta_c,$$

$$\mathbf{B} = \chi'(\nabla\zeta_c \times \nabla\psi + q(\psi)\nabla\psi \times \nabla\theta_c) = B_{\theta_c}\nabla\theta_c + B_{\zeta_c}\nabla\zeta_c.$$

Equation (7) can be integrated directly by shooting method as a first-order differential equation. For the global coordinate system to exist, a constraint from the Jacobian is imposed on the solution. The new Jacobian (J_c) is related to the original Jacobian (J) by:

$$J_c = (\nabla\psi \times \nabla\theta_c) \cdot \nabla\zeta_c^{-1} \sim (\nabla\psi \times \nabla\theta) \cdot \nabla\zeta^{-1} = \frac{J}{1 + \frac{\partial\nu}{\partial\theta}},$$

which shows that the coordinate transformation would introduce a singularity if the denominator vanishes in this expression. In order to avoid such singularity, we need to ensure that

$$\frac{\partial\nu}{\partial\theta} + 1 \neq 0.$$

We find that this constraint can indeed be satisfied in general cases of tokamaks, which follows from a convenient ordering of the coefficients in Eq. (7): $C_1 \ll C_2$. For simplicity, we demonstrate this ordering in PEST coordinates. The PEST
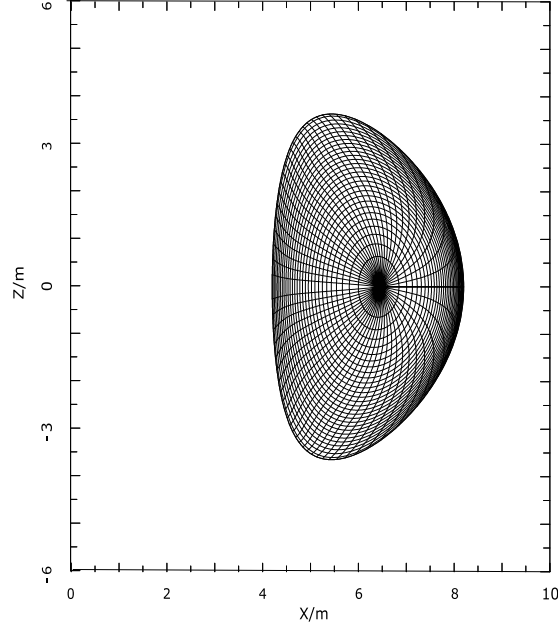
Fig. 1. The canonical coordinates constructed with the boundary condition $\nu_0 = 0$ for the ITER-like equilibrium (generated with the equilibrium code TOQ). The equilibrium parameters are: plasma beta $\beta = 0.08$, aspect ratio $\epsilon \sim 1/3$, elongation $\kappa = 1.86$, and triangularity $\delta = 0.5$. The new grid mesh is very similar to the PEST grid mesh.

coordinate system uses the geometric angle ϕ as the toroidal angle. In this case, the coefficients in Eq. (7) can be estimated as:

$$C_1 \sim -\frac{|\nabla\phi|^2 \nabla\psi \cdot \nabla\theta_p}{|\nabla\psi|^2 |\nabla\theta_p|^2} \sim \left(\frac{a}{R}\right)^2 \nabla\psi \cdot \nabla\theta_p,$$

$$C_2 \sim -\frac{qq'|\nabla\psi|^2 |\nabla\theta_p|^2}{|\nabla\psi|^2 |\nabla\theta_p|^2} \sim 1,$$

where a is the minor radius and R is the major radius of the tokamak. The inverse aspect ratio ($\epsilon = a/R$) and the factor $\nabla\psi \cdot \nabla\theta_p$ are usually less than unity in tokamaks. As a result, this ordering indicates that the nonlinearity is relatively small in Eq. (7) and does not bring in numerical difficulty, so that the final coordinates are not drastically different from the original coordinates ($\nu \sim O(\epsilon^2)$). If ν is sufficiently small, the new Jacobian is close to the PEST Jacobian, and the transformation does not introduce singularities. This feature is essential for global coordinate transformation.

3. Numerical implementation

In this section, we describe a computational module that uses a realistic tokamak equilibrium configuration file (like DCON [8] or EFIT [9]) and provides the canonical straight field line coordinates. We also present a comparative simulation of resistive wall instability in the new and old coordinates as a test case.

The developed module solves Eq. (7) in general straight field line coordinates. Since the poloidal angle dependence in Eq. (7) is a periodic function, we use Fourier representation of ν and factors C in Eq. (7):

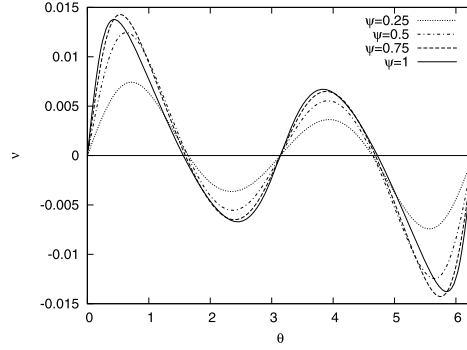$$\nu_m = \frac{1}{\sqrt{2\pi}} \int_{-\pi}^{\pi} \nu e^{-im\theta} \mathrm{d}\theta,$$

Fig. 2. The difference in poloidal angle (ν) between PEST and new coordinates at different radial locations ($\psi = 0.25, 0.5, 0.75, 1$). The horizontal axis stands for the poloidal angle θ in PEST coordinates.
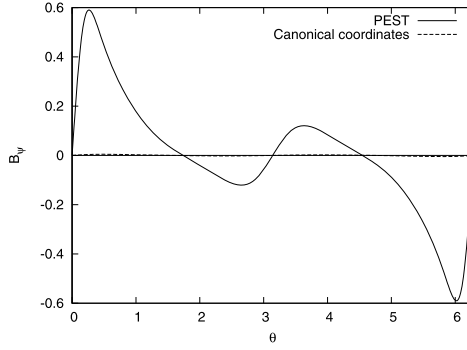

Fig. 3. The covariant component of radial magnetic field B_ψ versus poloidal angle in PEST and canonical straight field line coordinates.

$$C^{mm'} = \frac{1}{2\pi} \int\limits_{-\pi}^{\pi} C(\theta) e^{i(m'-m)\theta} d\theta.$$

We thereby obtain a set of ordinary differential equations for the Fourier components of ν:

$$\frac{\partial \nu_m}{\partial \psi} = \sum_{i,j} iC_1^{mi} \delta_{ij} j\nu_j + \sum_{i,j,k} \frac{i}{\sqrt{8\pi}} C_2^{mi} \delta_{ij} j\nu_{j-k}\nu_k + \sum_i C_2^{mi}\nu_i + C_{1m},$$

and we then truncate this set appropriately to achieve convergence of the solution.

We set $\nu = \nu_0$ at the innermost flux surface and integrate the nonlinear equations radially outwards with this boundary condition. Note that there is a considerable freedom in choosing ν_0 as long as ν_0 is not too large to produce singularity in the solution. We use an integration subroutine (D02BJF) from NAG (Numerical Algorithms Group) library, which is a fixed order Runge–Kutta method, and the computation tolerance is set to 10^{-5}.

We have tested the coordinate transformation module for various realistic equilibria, and the results render global canonical straight field line coordinates. We first take an up-down-symmetric ITER-type equilibrium, and solve for ν in the PEST coordinates with $\nu_0 = 0$ on magnetic axis. The integration error is within the tolerance, and the Fourier series converges quickly. Fig. 1 shows the resulting grid mesh in the new coordinates, which is very similar to the PEST grid mesh. In Fig. 2, we plot ν versus θ at various radial positions. We find that the modification of the poloidal angle is very small and is therefore free from numerical difficulties associated with the orthogonal coordinates. We also compare B_ψ in the new coordinates to that in the PEST coordinates (see Fig. 3) and find that B_ψ vanishes in the new coordinates as expected. For the
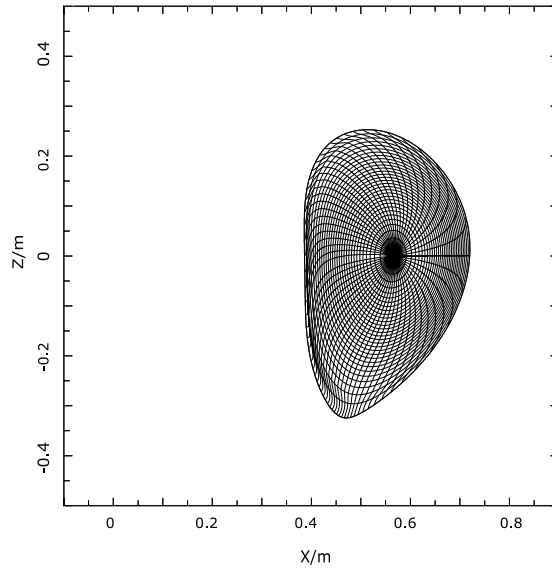
Fig. 4. The canonical coordinates for the asymmetric COMPASS equilibrium with the boundary condition $v_0 = 0$. The new grid mesh is also similar to the PEST grid mesh.
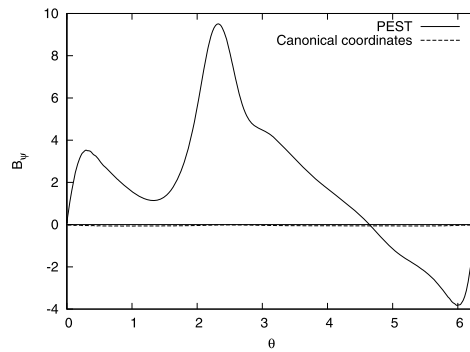

Fig. 5. B_ψ versus poloidal angle in PEST and new coordinates for the COMPASS equilibrium.

asymmetric COMPASS [10] equilibrium, we also find that the grid mesh of the new canonical coordinates with $v_0 = 0$ is similar to the original PEST coordinates (Fig. 4), and B_ψ vanishes in the new coordinates (see Fig. 5).

The new canonical coordinate system is flexible with regard to boundary condition. For example, we can use the boundary condition according to Hamada coordinates (which specifies Jacobian $J = const.$) instead of setting $v_0 = 0$, and we then obtain a different grid mesh. As seen from Fig. 6, the grid mesh of the final canonical coordinates is denser at the outboard midplane than that in Fig. 1. This feature is also present in the numerical tests for other types of equilibria such as COMPASS and Shafranov equilibrium. Thus, by applying different boundary conditions, we are able to optimize the new canonical coordinates for particular calculations.

The new coordinate transformation module has been incorporated into the AEGIS [11] code with Fortran 90/95. For benchmark purpose, we calculate the Resistive Wall Mode (RWM) in the new coordinates against the Hamada coordinates.
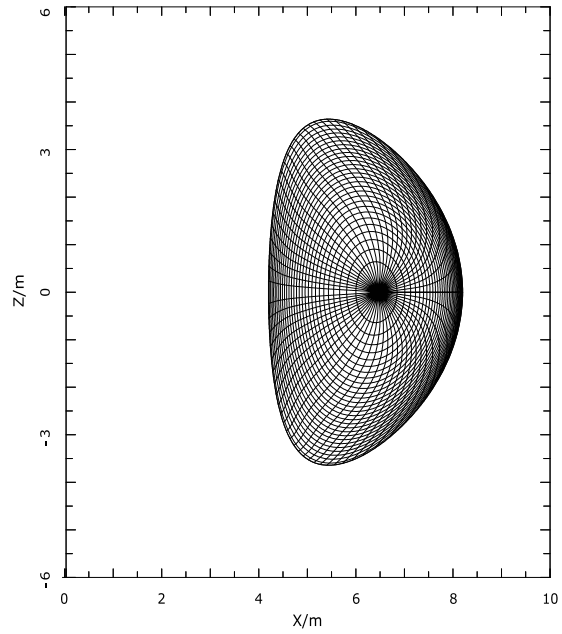
Fig. 6. The grid mesh of canonical coordinates for the ITER-like equilibrium with boundary condition close to Hamada coordinates.
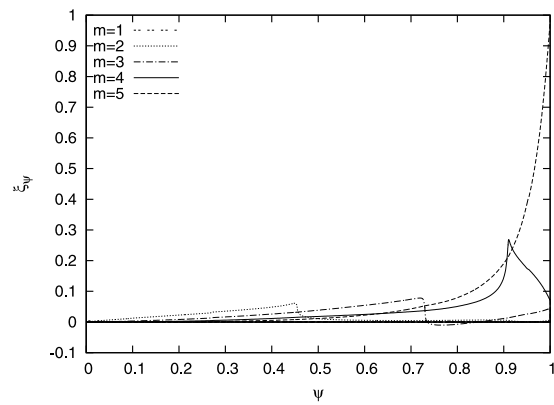

Fig. 7. The $n = 1$ resistive wall modes computed by AEGIS in the coordinate described in Fig. 6. The poloidal magnetic flux ψ is used as the horizontal coordinate and different Fourier components of plasma displacement $\xi_\psi = \boldsymbol{\xi} \cdot \nabla \psi$ are plotted. Total amount of poloidal components is 20. The critical wall position is at $\psi = 1.375$.
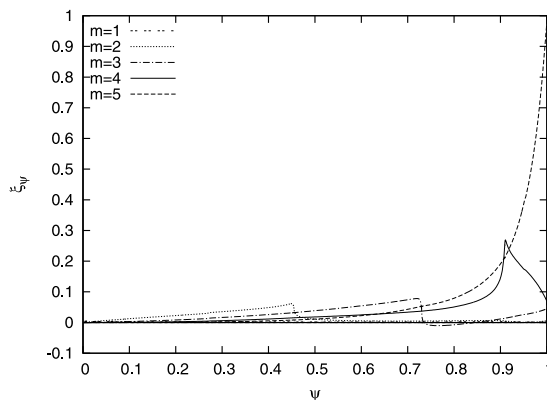
93

Fig. 8. The $n = 1$ mode calculated in Hamada coordinates for the ITER-like equilibrium. The total amount of poloidal components is the same (20) and critical wall position is also $\psi = 1.375$.

Resistive wall modes are the external kink mode with a resistive wall. The external kink modes can be stabilized by having a perfectly conducting wall close to the plasma inside the critical wall position, but the resistive wall modes are still unstable in this case [12]. We find good agreement in all respects, such as the growth rate, mode structure, the critical wall position, etc. Fig. 7 shows the $n = 1$ resistive wall mode for the ITER-type equilibrium using the coordinates in Fig. 6, which is similar to the result computed in Hamada coordinates shown in Fig. 8. The critical wall position is also in good agreement with similar amount of sidebands. The new canonical coordinate system is also ready to be used with other existing MHD codes.

4. Summary

To summarize, we introduce new canonical straight field line coordinates by changing the poloidal and toroidal angles of the general straight field line coordinates. The new coordinates eliminate the covariant and contravariant components of the radial magnetic field, which was previously possible only in orthogonal coordinates and was impractical for the tokamak equilibrium. The fact that the radial component of the magnetic field vanishes allows us to express the guiding center Lagrangian in terms of the angle coordinates and their conjugate momenta in a straightforward way. In addition, the new coordinates are also straight field line coordinates, which is advantageous to MHD simulations.

Our simulation results show that the new coordinates are numerically feasible. In the coordinate transformation, corrections to the poloidal and toroidal angles are small, and global coordinate system exists in general for tokamaks. Besides, multiple canonical coordinates can coexist due to the flexibility of the boundary conditions, which offers a variety of options for different problems.

References

[1] V.D. Shafranov, Plasma Equilibrium in a Magnetic Field, Reviews of Plasma Physics, vol. 2, Consultants Bureau, New York, 1966, pp. 103–151.
[2] R.C. Grimm, J.M. Greene, J.L. Johnson, Methods of Computational Physics, vol. 9, Academic Press, New York, London, 1976, pp. 253–280.
[3] S. Hamada, Hydromagnetic equilibria and their proper coordinates, Nucl. Fusion 2 (1962) 23–37.
[4] A.H. Boozer, Plasma equilibrium with rational magnetic surfaces, Phys. Fluids 24 (1981) 1999–2003.
[5] R.G. Littlejohn, Hamiltonian formulation of guiding center motion, Phys. Fluids 24 (1981) 1730–1749.
[6] R.B. White, The Theory of Toroidally Confined Plasmas, Imperial College Press, London, 2014, pp. 77–79.
[7] J.D. Meiss, R.D. Hazeltine, Canonical coordinates for guiding center particles, Phys. Fluids B 2 (1999) 2563–2567.
[8] A.H. Glasser, The direct criterion of Newcomb for the stability of an axisymmetric toroidal plasma, Los Alamos Report LA-UR-95-528, 1997.
[9] L.L. Lao, H.S. John, R.D. Stambaugh, W. Pfeiffer, Separation of $\hat{\beta}_p$ and l_i in tokamak of non-circular cross-section, Nucl. Fusion 25 (1985) 1421–1436.
[10] A.V. Melnikov, T. Markovic, L.G. Eliseev, et al., Quasicoherent modes on the COMPASS tokamak, Plasma Phys. Control. Fusion 57 (2015) 065006.
[11] L.J. Zheng, M. Kotschenreuther, AEGIS: an adaptive ideal-magnetohydrodynamics shooting code for axisymmetric plasma stability, J. Comp. Physiol. 211 (2006) 748–766.
[12] J.P. Freidberg, Ideal Magnetohydrodynamics, Pleum Press, New York, 1987, pp. 307–314.

Bibliography

[1] Paul Murray Bellan. *Fundamentals Of Plasma Physics.* Cambridge University Press, 2006.

[2] H. L. Berk, D. N. Borba, B. N. Breizman, S. D. Pinches, and S. E. Sharapov. Theoretical Interpretation of Alfvén Cascades in Tokamaks with Nonmonotonic q Profiles. *Physical Review Letters*, 87(18):185002, October 2001.

[3] H. L. Berk and B. N. Breizman. Saturation of a single mode driven by an energetic injected beam. II. Electrostatic "universal" destabilization mechanism. *Physics of Fluids B*, 2:2235–2245, September 1990.

[4] H. L. Berk, B. N. Breizman, J. Candy, M. Pekker, and N. V. Petviashvili. Spontaneous hole-clump pair creation. *Physics of Plasmas*, 6:3102–3113, August 1999.

[5] H. L. Berk, B. N. Breizman, and M. Pekker. Numerical simulation of bump-on-tail instability with source and sink. *Physics of Plasmas*, 2:3007–3016, August 1995.

[6] H. L. Berk, B. N. Breizman, and M. Pekker. Nonlinear Dynamics of a Driven Mode near Marginal Stability. *Physical Review Letters*, 76:1256–1259, February 1996.

[7] H. L. Berk, B. N. Breizman, and M. S. Pekker. Simulation of Alfven-wave-resonant-particle interaction. *Nuclear Fusion*, 35:1713–1720, December 1995.

[8] H. L. Berk, B. N. Breizman, and N. V. Petviashvili. Spontaneous hole-clump pair creation in weakly unstable plasmas. *Physics Letters A*, 234:213–218, February 1997.

[9] A. H. Boozer. Plasma equilibrium with rational magnetic surfaces. *Physics of Fluids*, 24:1999–2003, November 1981.

[10] B. N. Breizman. Nonlinear travelling waves in energetic particle phase space. *Nuclear Fusion*, 50(8):084014, August 2010.

[11] B. N. Breizman, H. L. Berk, M. S. Pekker, F. Porcelli, G. V. Stupakov, and K. L. Wong. Critical nonlinear phenomena for kinetic instabilities near threshold. *Physics of Plasmas*, 4:1559–1568, May 1997.

[12] B. N. Breizman, M. S. Pekker, and S. E. Sharapov. Plasma pressure effect on Alfvén cascade eigenmodes. *Physics of Plasmas*, 12(11):112506, November 2005.

[13] B. N. Breizman and S. E. Sharapov. Energetic particle drive for toroidicity-induced Alfven eigenmodes and kinetic toroidicity-induced Alfven eigenmodes in a low-shear tokamak. *Plasma Physics and Controlled Fusion*, 37:1057–1074, October 1995.

[14] B. N. Breizman and S. E. Sharapov. Major minority: energetic particles in fusion plasmas. *Plasma Physics and Controlled Fusion*, 53(5):054001, May 2011.

[15] J. Candy, B. N. Breizman, J. W. Van Dam, and T. Ozeki. Multiplicity of low-shear toroidal Alfvén eigenmodes. *Physics Letters A*, 215:299–304, February 1996.

[16] E. Chen, H. Berk, B. Breizman, and L. Zheng. Energy absorption due to spatial resonance of Alfven waves at continuum tip. In *APS Meeting Abstracts*, October 2011.

[17] L. Chen, R. B. White, and M. N. Rosenbluth. Excitation of Internal Kink Modes by Trapped Energetic Beam Ions. *Physical Review Letters*, 52:1122–1125, March 1984.

[18] C. Z. Cheng and M. S. Chance. Low-n shear Alfvén spectra in axisymmetric toroidal plasmas. *Physics of Fluids*, 29:3695–3701, November 1986.

[19] N. J. Fisch. Elementary processes underlying alpha channeling in tokamaks. In S. Benkadda, N. Dubuit, and Z. Guimara˜es-Filho, editors, *American Institute of Physics Conference Series*, volume 1478 of *American Institute of Physics Conference Series*, pages 80–90, September 2012.

[20] G. Y. Fu and C. Z. Cheng. Excitation of high-n toroidicity-induced shear Alfvén eigenmodes by energetic particles and fusion alpha particles in

tokamaks. *Physics of Fluids B*, 4:3722–3734, November 1992.

[21] G. Y. Fu and J. W. Van Dam. Excitation of the toroidicity-induced shear Alfvén eigenmode by fusion alpha particles in an ignited tokamak. *Physics of Fluids B*, 1:1949–1952, October 1989.

[22] M. P. Gryaznevich and S. E. Sharapov. Perturbative and non-perturbative modes in START and MAST. *Nuclear Fusion*, 46:S942–S950, October 2006.

[23] A. Hasegawa and L. Chen. Plasma Heating by Alfvén-Wave Phase Mixing. *Physical Review Letters*, 32:454–456, March 1974.

[24] R. D. Hazeltine and J. D. Meiss. *Plasma Confinement*. Dover, 2003.

[25] R. D. Hazeltine and F. L. Waelbroeck. *The Framework Of Plasma Physics*. Westview Press, 2004.

[26] W. W. Heidbrink. Basic physics of Alfvén instabilities driven by energetic particles in toroidally confined plasmasa). *Physics of Plasmas*, 15(5):055501, May 2008.

[27] W. W. Heidbrink and G. J. Sadler. REVIEW PAPER: The behaviour of fast ions in tokamak experiments. *Nuclear Fusion*, 34:535–615, April 1994.

[28] J. M. Greene I. B. Bernstein and M. D. Kruskal. Exact nonlinear plasma oscillations. *Physical Review*, 108:546, 1957.

[29] K. Ikeda. PREFACE: Progress in the ITER Physics Basis. *Nuclear Fusion*, 47, June 2007.

[30] L. Landau. On the vibrations of the electronic plasma. *JETP*, 16:574, 1946.

[31] M. Lesur. The Berk-Breizman Model as a Paradigm for Energetic Particle-driven Alfven Eigenmodes. *ArXiv e-prints*, January 2011.

[32] M. Li, B. N. Breizman, and L. Zheng. Canonical straight field line magnetic flux coordinates for tokamaks. *Journal of Computational Physics*, 326:334–341, December 2016.

[33] M. Li, B. N. Breizman, L. J. Zheng, and E. Y. Chen. Continuum absorption in the vicinity of the toroidicity-induced Alfvén gap. *New Journal of Physics*, 17(12):125001, December 2015.

[34] M. Li, B. N. Breizman, L. J. Zheng, L. Lin, W. X. Ding, and D. L. Brower. Alfvén modes in the Madison Symmetric Torus. *Physics of Plasmas*, 21(8):082505, August 2014.

[35] L. Lin, J. K. Anderson, D. L. Brower, W. Capecchi, W. X. Ding, S. Eilerman, C. B. Forest, J. J. Koliner, D. Liu, M. D. Nornberg, J. Reusch, and J. S. Sarff. Energetic-particle-driven instabilities and induced fast-ion transport in a reversed field pincha). *Physics of Plasmas*, 21(5):056104, May 2014.

[36] L. Lin, W. X. Ding, D. L. Brower, J. J. Koliner, S. Eilerman, J. A. Reusch, J. K. Anderson, M. D. Nornberg, J. S. Sarff, J. Waksman, and D. Liu. Measurement of energetic-particle-driven core magnetic fluctuations and induced fast-ion transport. *Physics of Plasmas*, 20(3):030701, March 2013.

[37] R. G. Littlejohn. Hamiltonian formulation of guiding center motion. *Physics of Fluids*, 24:1730–1749, September 1981.

[38] S. M. Mahajan. Kinetic theory of shear Alfven waves. *Physics of Fluids*, 27:2238–2247, September 1984.

[39] J. D. Meiss and R. D. Hazeltine. Canonical coordinates for guiding center particles. *Physics of Fluids B*, 2:2563–2567, November 1990.

[40] V. Mukhovatov, M. Shimada, A. N. Chudnovskiy, A. E. Costley, Y. Gribov, G. Federici, O. Kardaun, A. S. Kukushkin, A. Polevoi, V. D. Pustovitov, Y. Shimomura, T. Sugie, M. Sugihara, and G. Vayakis. Overview of physics basis for ITER. *Plasma Physics and Controlled Fusion*, 45(27):A235–A252, December 2003.

[41] R. M. Nyqvist, M. K. Lilley, and B. N. Breizman. Adiabatic description of long range frequency sweeping. *Nuclear Fusion*, 52(9):094020, September 2012.

[42] S. D. Pinches, H. L. Berk, M. P. Gryaznevich, S. E. Sharapov, and J.-E. Contributors. Spectroscopic determination of the internal amplitude of

frequency sweeping TAE. *Plasma Physics and Controlled Fusion*, 46:S47–S57, July 2004.

[43] M. N. Rosenbluth, H. L. Berk, J. W. van Dam, and D. M. Lindberg. Continuum damping of high-mode-number toroidal Alfvén waves. *Physical Review Letters*, 68:596–599, February 1992.

[44] M. N. Rosenbluth, H. L. Berk, J. W. Van Dam, and D. M. Lindberg. Mode structure and continuum damping of high-n toroidal Alfvén eigenmodes*. *Physics of Fluids B*, 4:2189–2202, July 1992.

[45] V. D. Shafranov. Plasma Equilibrium in a Magnetic Field. *Reviews of Plasma Physics*, 2:103, 1966.

[46] D. Sünder. W. D. D'haeseleer, W. N. G. Hitchon, J. D. Callen, J. L. Shohet: Flux Coordinates and Magnetic Field Structure-A Guide to a Fundamental Tool of the Plasma Theory. Edited by R. Glowinski, M. Holt, P. Hut, H. B. Keller, J. Killeen, S. A. Orszag and V. V. Rusanov. Springer Series in Computational Physics, Springer Verlag Berlin 1991. *Contributions to Plasma Physics*, 31:692–692, 1991.

[47] M. A. van Zeeland, G. J. Kramer, M. E. Austin, R. L. Boivin, W. W. Heidbrink, M. A. Makowski, G. R. McKee, R. Nazikian, W. M. Solomon, and G. Wang. Radial Structure of Alfvén Eigenmodes in the DIII-D Tokamak through Electron-Cyclotron-Emission Measurements. *Physical Review Letters*, 97(13):135001, September 2006.

[48] R. B. White. *The Theory of Toroidally Confined Plasmas.* Imperial, 2nd edition, 2006.

[49] K.-L. Wong. REVIEW ARTICLE: A review of Alfvén eigenmode observations in toroidal plasmas. *Plasma Physics and Controlled Fusion*, 41:R1–R56, January 1999.

[50] K. L. Wong, R. J. Fonck, S. F. Paul, D. R. Roberts, E. D. Fredrickson, R. Nazikian, H. K. Park, M. Bell, N. L. Bretz, R. Budny, S. Cohen, G. W. Hammett, F. C. Jobes, D. M. Meade, S. S. Medley, D. Mueller, Y. Nagayama, D. K. Owens, and E. J. Synakowski. Excitation of toroidal Alfvén eigenmodes in TFTR. *Physical Review Letters*, 66:1874–1877, April 1991.

[51] L.-J. Zheng and M. Kotschenreuther. AEGIS: An adaptive ideal magnetohydrodynamics shooting code for axisymmetric plasma stability. *Journal of Computational Physics*, 211:748–766, January 2006.

[52] L.-J. Zheng, M. Kotschenreuther, and M. S. Chu. Rotational Stabilization of Resistive Wall Modes by the Shear Alfvén Resonance. *Physical Review Letters*, 95(25):255003, December 2005.

Vita

Meng Li was born in Nanyang, Henan, P.R.China in 1991. He graduated from School for the Gifted Young in the University of Science and Technology of China (USTC) and received the Bachelor of Science degree in applied physics in 2012. He then attended the graduate school at The University of Texas at Austin in 2012. He completed his Ph. D in plasma physics at the University of Texas at Austin in 2017.

Permanent address: 2501 Lake Austin Blvd Apt B104
Austin, Texas 78703

This dissertation was typeset with LaTeX[†] by the author.

[†]LaTeX is a document preparation system developed by Leslie Lamport as a special version of Donald Knuth's TeX Program.